(NASA-CR-141103) ACCELERATION PROCESSES IN THE QUASI-STEADY MAGNETOPLASMADYNAMIC DISCHARGE Ph.D. Thesis (Princeton Univ.) 137 p HC $5.75 CSCL 20I
N75-13629
Unclas
G3/75 03682

Princeton University

[redacted]

DEI SUB NUMINE VIGET

Department of
Aerospace and
Mechanical Sciences

Prepared for
National Aeronautics
and Space Administration
NASA Research Grant NGL 31-001-005

ACCELERATION PROCESSES
IN THE
QUASI-STEADY MAGNETOPLASMADYNAMIC DISCHARGE

M. J. Boyle and R. G. Jahn

Report 1188*

Prepared by Michael J. Boyle
M. J. Boyle

Approved by R. G. Jahn
R. G. Jahn
Dean, School of Engineering

*This report is a reproduction in entirety of the Ph.D. dissertation of Mr. Michael John Boyle. It is submitted to the sponsor and to the distribution list in this form both as a presentation of the technical material, and as an indication of the academic program supported by this Grant.

October 1974

School of Engineering and Applied Science
Department of Aerospace and Mechanical Sciences
Guggenheim Aerospace Propulsion Laboratories
PRINCETON UNIVERSITY
Princeton, New Jersey

ABSTRACT

The flow field characteristics within the discharge chamber and exhaust of a quasi-steady magnetoplasmadynamic (MPD) arcjet are examined to clarify the nature of the plasma acceleration process. In order to observe discharge characteristics unperturbed by insulator ablation and terminal voltage fluctuations, three criteria must first be satisfied: the use of refractory insulator materials, a mass injection geometry tailored to provide propellant to both electrode regions of the discharge, and a cathode of sufficient surface area to permit nominal MPD arcjet operation for given combinations of arc current and total mass flow. The axial velocity profile and electromagnetic discharge structure are measured for an arcjet configuration which functions nominally at 15.3 kA and 6 g/sec argon mass flow ($J^2/\dot{m}$ = 39 kA^2-sec/g). An empirical two-flow plasma acceleration model is advanced which delineates inner and outer flow regions and accounts for the observed velocity profile and calculated thrust of the accelerator. The acceleration process is characterized by nearly 50% of the total arc current flowing downstream of the anode orifice. The plasma leaves the discharge chamber at a speed of less than 9.0 km/sec and accelerates to 12.5 km/sec several anode orifice diameters downstream. A supersonic expansion in the exhaust plume accounts for the observed plasma acceleration to 12.5 km/sec of the inner flow. This terminal velocity significantly exceeds the previously proposed Alfven limiting velocity of 8.7 km/sec for argon. It also corresponds to the mass-averaged velocity associated with the thrust attributable to the inner flow, thereby implying a fraction of the total thrust is recovered during the flow expansion in the downstream exhaust regions of the accelerator. In contrast, the outer flow produces thrust with a lower specific impulse and thus degrades the overall performance of the thruster. It is suggested that improved thruster performance may be realized by reducing the extent of the outer flow.

TABLE OF CONTENTS

Page

TABLE OF CONTENTS (Cont'd)

TABLE OF CONTENTS (Cont'd)

LIST OF ILLUSTRATIONS

LIST OF ILLUSTRATIONS (Cont'd)

Chapter I

Quasi-steady Magnetoplasmadynamic Accelerators

I-1 Electromagnetic Plasma Acceleration

Electromagnetic accelerators are able to combine large values of total and specific impulse, thereby making the electromagnetic plasma thruster a particularly attractive candidate for highly energetic space missions. Characteristically, such missions require the primary thrusting system to provide total impulses greater than 10^6 newton-seconds and specific impulses between 1000 and 10,000 seconds.(1) Present chemical systems are limited to maximum attainable specific impulses of less than 600 seconds; a limit established by the finite enthalpy of the reactants. Electrostatic or ion thrusters can provide high specific impulses ($I_{sp} > 1000$ sec) but suffer from inherent space charge flow limitations which translate into low thrust operation. Hence ion engines must be clustered in large arrays to provide the required total impulse. Low thrust operation further restricts the application of electrostatic thrusters to only those missions during which sudden spacecraft accelerations are not required.

In principle, electromagnetic plasma acceleration circumvents the fundamental limitations of both the chemical and electrostatic thruster systems. The basic principles of electromagnetic plasma acceleration are schematically illustrated in Figure 1-1 for a self-field magnetoplasmadynamic (MPD) arcjet. In this case, a gaseous propellant is introduced upstream of two concentric electrodes. An arc discharge is struck between the anode and cathode, and a diffuse, cylindrically symmetric current pattern is established throughout the discharge chamber.

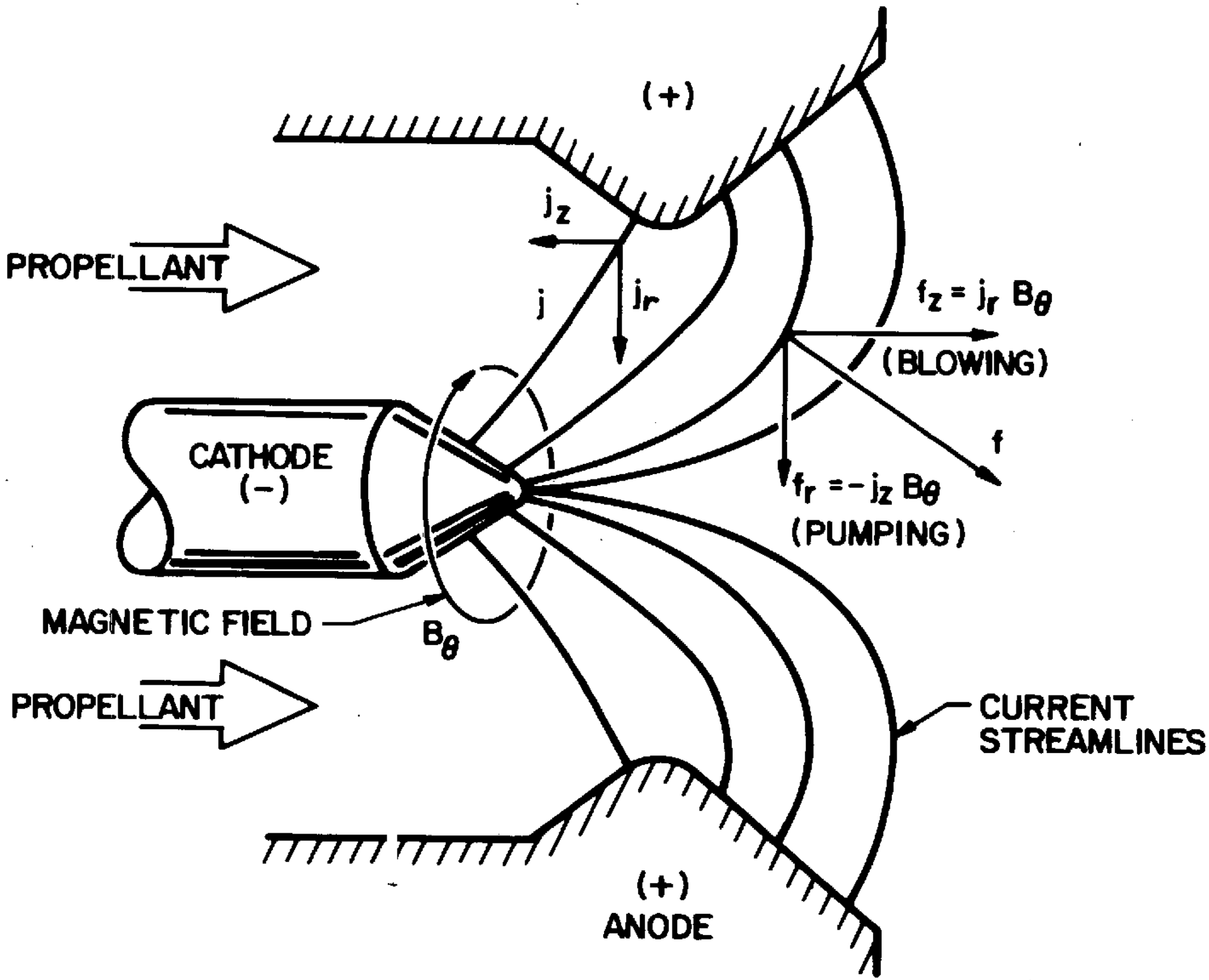

SELF - FIELD MPD ACCELERATOR

FIGURE 1-1

AP25-5033

The axial and radial components of the current density cross with the azimuthal self-magnetic field, producing radial and axial Lorentz body forces which accelerate the ionized propellant downstream. Since the plasma flow is quasi-neutral, no space charge limitations on the accelerated mass flow rate exist, thereby allowing thrust densities orders of magnitude larger than electrostatic thrust levels to be realized. Furthermore, maximum attainable MPD exhaust velocities are independent of, and thus not limited by, the enthalpy of the propellant, since electrical input power externally supplied couples directly into the kinetic motion of the propellant. In this sense MPD acceleration is "power limited" in contrast to the "energy limited" nature of chemical processes.

The net thrust of the MPD accelerator is related to the $\bar{j} \times \bar{B}$ body force distribution throughout the discharge volume. For a self-field device, these Lorentz forces scale quadratically with the total arc current. Clearly then, high specific impulses and thrust densities should be associated with high current modes of MPD arcjet operation. However, previous experience with steady-state accelerators demonstrates that these high power operational modes can not be maintained continuously for arc currents greater than several thousand amperes.(2) Electrode and insulator surfaces destruct when subjected to the thermal stresses concomitant with steady-state, high power arcjet operation. Thus,in order to realize the advantages accrued at higher arc currents without inducing structural failure, the MPD accelerator must operate in a pulsed mode.

I-2 The Quasi-steady MPD Arcjet

Pulsed plasma accelerators which accelerate propellant by the sweeping action of propagating current sheets have been studied extensively in the past.(3,4,5) These devices are characterized by discharge times ranging between 1 and 10 microseconds. On these time scales however, inefficient transient phenomena including initial breakdown, ionization, electrode and mass ejection processes keep the overall thruster efficiency below several percent. Hence, results from both steady-state and pulsed plasma devices separately suggest extended current pulses with transient periods short compared to total discharge times, are desirable.

Between 1966 and 1969, it was demonstrated that current pulses, several hundred microseconds long discharged between concentric electrodes would stabilize in times short compared to the duration of the current pulse.(6,7) That is, after an initial transient period, the arc current discharge pattern assumes a "quasi-steady" distribution which remains constant for the remainder of the pulse. This stabilized discharge pattern accelerates the plasma in a mode resembling that of the steady-state MPD arcjet, rather than by the sweeping action of a propagating current sheet. This mode of plasma acceleration is referred to as "quasi-steady plasma acceleration."

Quasi-steady plasma acceleration results after properly tailored mass flow and current pulses are delivered to the accelerator's discharge chamber. An arc discharge is initiated across the electrodes after the injected propellant has assumed a steady cold flow pattern throughout the discharge chamber. Spatial and temporal stabilization of the electromagnetic fields generated by the arc discharge occurs on a time scale typically between ten and one hundred microseconds after discharge initiation. Shortly thereafter, the propellant mass swept from the accelerator chamber by the initial breakdown processes is replenished by the protracted mass flow pulse, and gasdynamic stabilization of the discharge occurs. Only for times during which both the electromagnetic and flow fields are unchanging may the plasma acceleration process be described as quasi-steady.

I-3 Quasi-steady Plasma Acceleration Models

To date, a complete theoretical understanding of the high power plasma acceleration process does not exist. The nonlinear coupling of the electromagnetic and gasdynamic processes responsible for the plasma acceleration makes the mathematical modelling of the problem extremely complex. The paucity of all but the most simplified analytical models is at least partially a result of the historical development of the devices. The steady-state MPD arc inadvertantly evolved from electrothermal thruster research in 1964.(8) Encouraging preliminary results prompted an indiscriminant rush to achieve bigger and better performance without acquiring a fundamental understanding of the devices. Only recently have series of systematic experiments been undertaken to clarify the nature of the accleration process.

Previously proposed theoretical and semi-empirical arcjet models are discussed briefly below. A more detailed review is given by Jahn,(1) and the specifics of each model may be found in the referenced literature.

I-3-1 Magnetogasdynamic Model

The magnetogasdynamic or continuum approach models the plasma acceleration process in terms of a conducting, continuum fluid. Macroscopic variables, including the mass averaged velocity u, the current density j, and the self-induced magnetic field B, describe the acceleration of particular fluid elements, under the prevailing electromagnetic body forces. Actually, the self-field thrust can be evaluated from a volume integration of the $\bar{j} \times \bar{B}$ distribution throughout the discharge region without explicit reference to the local fluid properties. Such an integration yields a relation of the form:

$$T_{em} = \frac{\mu_o J^2}{4\pi} \left[\ln\left(\frac{r_a}{r_c}\right) + c \right] = bJ^2 \qquad (1\text{-a})$$

or in terms of the mass averaged velocity,

$$u = b \left(\frac{J^2}{\dot{m}} \right) \qquad (1\text{-b})$$

where

$$b = \frac{\mu_o}{4\pi} \left[\ln\left(\frac{r_a}{r_c}\right) + c \right]$$

and J is the total arc current, μ_o the magnetic permeability, $\dot{m}$ the accelerated mass flow rate, r_a and r_c the maximum anode and cathode current attachment radii, and c a numerical constant of order one.

It may be shown that the above result is independent of the local $\bar{j} \times \bar{B}$ distribution throughout the discharge plasma, except for the constant c which depends upon the current attachment pattern off the tip of the cathode.(9) Both the self-field electromagnetic thrust and mass averaged exhaust velocity depend only on the input parameters of the accelerator. As a result, the self-field thrust equation embodies no information concerning local acceleration mechanisms in that the local $\bar{j} \times \bar{B}$ pattern and the magnetogasdynamic fluid properties are not theoretically specified. Such information must be obtained experimentally. Furthermore, electrothermal contributions to the plasma acceleration are not included explicitly.

I-3-2 Collisionless Stratton Model

In contrast, the plasma acceleration mechanisms are called forth explicitly in a collisionless arcjet model proposed by both Stratton(10) and Watson.(11) This model relies on charged particle orbit theory to describe the ion and electron trajectories in the crossed electric and self-induced magnetic fields of the discharge. Ions created in the vicinity of the outer anode electrode are characterized by gyro radii comparable to the discharge chamber dimensions. As a result, the ions are accelerated radially inwards and axially downstream under the combined influence of the electric and magnetic fields of the discharge. Space charge neutralization of the ion flow is provided by an electron beam streaming off the tip of the cathode. Features of this collisionless model include ion radial current conduction which couples the mass flow and arc current, and an exhaust velocity determined by the potential difference between the two electrodes.

$$J = \frac{e\dot{m}}{M_i} \tag{1-c}$$

$$u = \frac{\mu_o eJ}{2\pi M_i} \leq \left(\frac{2eV}{M_i}\right)^{\frac{1}{2}} \tag{1-d}$$

where M_i is the mass of the propellant ion and V is the arc voltage exclusive of the electrode falls.

The assumption of collisionless flow for the moderate density plasmas characteristic of quasi-steady accelerators is an extreme one. The particle orbit theory may be modified, however, to account for the effects of particle collisions. In this case, knowledge of the local Hall parameters is required to identify regions of particle acceleration, current conduction, and thrust generation.

I-3-3 1-D Parallel Plate Model

The quasi-steady discharge patterns and acceleration processes of a parallel plate accelerator are theoretically treated by Martinache and Lam.(12) A one-dimensional model of the discharge region and monofluid description of the plasma are assumed. The gasdynamics and electrodynamics of the problem are considered simultaneously rather than individually. Inlet and outlet boundary conditions and restrictions imposed upon the back emf delineate several classes of theoretical solutions. Electrothermal and electromagnetic modes of accelerator operation result, with the high current, electromagnetic mode the more efficient of the two. For various inlet conditions and arc currents, the solutions display normal shock patterns, choking of the flow within the accelerator and exit velocities equal to or slightly greater than the acoustic speed. Clearly though, the one-dimensional treatment precludes any examination of two-dimensional electromagnetic and/or flow expansion effects upon the specific impulse and thrust of the accelerator.

I-3-4 Minimum Flow Power Model

Experimental results from the AVCO, SSD laboratories first suggested quasi-steady MPD arcjet performance might be fundamentally limited.(13) Malliaris observed, for a given mass flow rate, a certain arc current above which erratic terminal voltage behavior and insulator ablation occurred. Furthermore, the onset of this erratic arcjet behavior scaled such that the parameter $(J^*)^2/\dot{m}$, the onset arc current squared divided by the injected mass flow rate, remained constant for a given propellant. This critical $J^2/\dot{m}$ parameter was interpreted as an upper fundamental limit imposed upon quasi-steady plasma acceleration. This conclusion was analytically supported by a minimum power model of the arcjet flow processes.

In this model, the arc discharge accelerates a mass flow rate (not necessarily identical with the injected mass flow) such that the power invested in the plasma flow, exclusive of the electrode fall regions, is minimized. The flow power is assumed to be expressible as the sum of kinetic and ionization power terms given by Equation 1-e. The minimum power condition is expressed by Equation 1-f.

$$P_{FLOW} = \frac{T^2}{2\dot{m}} + \frac{e\phi_i}{M_i} \quad \dot{m} \qquad (1\text{-}e)$$

$$\frac{\partial P_{FLOW}}{\partial \dot{m}} = 0 \qquad (1\text{-}f)$$

where a constant thrust T given by Equation 1-a, and negligible power in plasma thermal and radiative modes are additionally assumed. ϕ_i and M_i are the first ionization potential and ion mass of the propellant.

Partial differentiation of Equation 1-e, as specified by Equation 1-f, results in an optimum or critical value for the parameter $J^2/\dot{m}$,

$$(J^2/\dot{m})_{CRIT} = \frac{(2e\phi_i/M_i)^{\frac{1}{2}}}{b} \qquad (1\text{-}g)$$

dependent only upon the electromagnetic thrust coefficient b and the properties of the accelerated propellant. Numerically, expression 1-g was found to be in good agreement with empirical obserations for several different propellant species.

Because of this optimum $J^2/\dot{m}$ value, the minimum power arcjet model implies that both the exhaust velocity and specific impulse, I_{sp}, of the quasi-steady accelerator exhibit upper bounds:

$$I_{sp} = \frac{T}{\dot{m}\, g} = \frac{b}{g}\left(\frac{J^2}{\dot{m}}\right) \leq \frac{(2e\phi_i/M_i)^{\frac{1}{2}}}{g} \qquad (1\text{-h})$$

and

$$u_e = I_{sp}\; g \leq (2e\phi_i/M_i)^{\frac{1}{2}} \qquad (1\text{-i})$$

For argon propellant a maximum specific impulse of 890 seconds corresponding to an exhaust velocity of 8.7 km/sec is indicated. The minimum power assumption may be shown equivalent to an energy equipartition between kinetic and ionization modes. As a consequence, the kinetic power efficiency of the accelerator is implied to be at best 50% excluding the inherent losses associated with electrode phenomena.

Despite this arcjet model's dire implications, no measurements other than voltages and exhaust velocities were made to confirm and/or clarify the nature of this apparent limitation.

I-4 Thesis Organization

Clearly the need exists for a further clarification of the plasma acceleration processes in the quasi-steady MPD arcjet. The quasi-steady MPD arcjet's ultimate applicability in a viable space thruster system depends in part upon a thorough understanding of its performance capabilities. The nature of the plasma acceleration process reflects directly upon two such performance parameters, the thrust and the exhaust velocity or specific impulse of the device. Because of the significant mathematical difficulties encountered in analytically evaluating these and similar parameters in any generality, an experimental or semi-empirical approach to the plasma acceleration problem is both necessary and enlightening.

Previous experimental study of the high power quasi-steady MPD arcjet at Princeton has focused primarily upon discharge stabilization phenomena and plasma diagnostic development. Clark and Eckbreth demonstrated discharge stabilization in coaxial and planar accelerator geometries.(6,7) Plasma diagnostics were developed to measure electromagnetic field distributions, velocity, impact pressure, and electron and ion temperature profiles in the quasi-steady MPD discharge. Upon acquiring the proper facilities and diagnostic techniques, attention was directed toward aspects of the quasi-steady plasma acceleration process.

Measured potential profiles throughout the discharge region discredited the simple electrostatic plasma acceleration model discussed in Section I-3-2.(14) Using a parallel plate geometry, Di Capua concluded that electrothermal contributions to the plasma acceleration were significant.(15) Cory was able to distinguish between electromagnetic and electrothermal thrust components of the coaxial accelerator using impact pressure measurements and the self-field thrust Equation 1-a.(16) Bruckner measured argon ion temperature and velocity profiles in this accelerator, later shown to be grossly influenced by the presence of ablated insulator species in the discharge plasma (Section III-3 and III-4). In fact, Bruckner was forced to conclude that the measured argon exhaust velocities were due in part to an unspecified momentum transfer process between the mixed argon and ablation plasma flows.(17)

In light of the significant perturbations induced by the severe insulator ablation, a decision had to be made regarding the direction in which further details of the acceleration process would be pursued. In order to proceed further with the same apparatus, the cause and effects of the ablation process would have had to been included in any plasma acceleration model. This approach had been previously followed by Workman, Keck, and others in their investigations of rail and vacuum arc accelerators.(18,19,20) Alternatively, one could try to eliminate insulator ablation from the problem by appropriate changes in the accelerator configuration.

This program takes the latter alternative in its examination of the quasi-steady plasma acceleration process. Chapter II briefly reviews the experimental facilities and diagnostic techniques used in this study. Chapter III discusses the manner in which insulator ablation perturbs the characteristic voltages and velocities associated with nominal arcjet operation, and the steps taken to eliminate those perturbations. Data suggesting an alternative explanation for the erratic arcjet behavior experienced at the "critical $J^2/\dot{m}$" condition are also presented. Chapter IV details the axial velocity profile associated with an arcjet configuration unperturbed by insulator ablation and erratic terminal voltage while operated at the "critical $J^2/\dot{m}$" condition. From local measurements of magnetic field, current density, electric field, and flow vector, a phenomenological plasma acceleration model is proposed. This model accounts for the measured final exhaust velocity and implied specific impulse, both of which exceed the upper limits previously suggested in Section I-3-4. A summary of experimental conclusions, as well as future recommendations, are presented in Chapter V.

Chapter II

Experimental Facilities and Diagnostic Techniques

II-1 Experimental Facilities

The research apparatus employed during the course of this study may be conveniently subdivided into four systems. The overall system consists of the MPD arc chamber, a propellant mass injection system, a current pulse-forming network, and a Plexiglas vacuum chamber. These pulsed quasi-steady MPD arcjet facilities are illustrated schematically in Figure 2-1.

II-1-1 MPD Accelerator Chamber

The cylindrical arc chamber is 12.7 cm in diameter and 5.0 cm deep. A 1.9 cm diameter tungsten cathode is centrally located within the discharge chamber. During the experimental program various cathode geometries were used. The particular cathode dimensions and geometry are explicitly noted in the subsequent text where appropriate. The annular aluminum anode has an i.d. of 10.2 cm and an outer barrel diameter of 18.8 cm. The anode is electrically insulated from the cathode by a cylindrical pyrex wall insert and a circular rear end plate. The insulator ablation discussed in Chapter III refers to the ablation of this end plate. The end plate is constructed of either Plexiglas or boron nitride.

II-1-2 Mass Injection System

In addition to acting as an insulator, the end plate contains the injection orifices through which argon propellant is supplied to the discharge chamber. Changes in mass injection geometry refer to the use of end plates which distribute the injected propellant to different locations

FIGURE 2-1

AP 25 R 4681 71

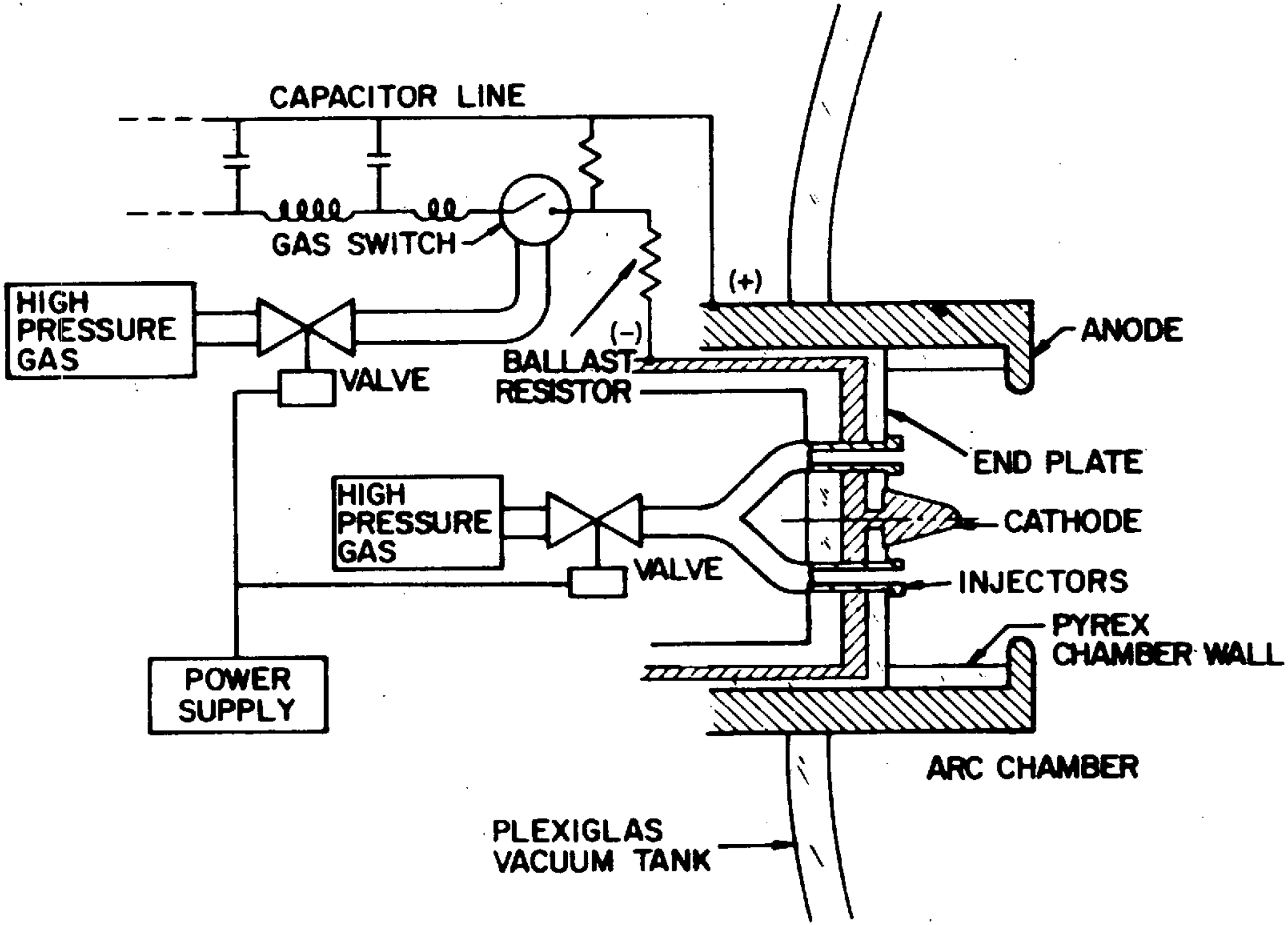

QUASI-STEADY MPD ARCJET FACILITIES

within the discharge chamber. Mass pulses of several milliseconds in duration are provided by a fast-acting solenoid valve fed by a high pressure argon reservoir. By varying the reservoir stagnation pressure, steady mass flow rates between 1 and 36 g/sec may be supplied to the MPD arc chamber.

II-1-3 Power Supply System

Rectangular current pulses are applied to the electrodes through a gas-triggered switch(21) and an impedance-matching ballast resistor from a 120 station L-C ladder pulse-forming network.(15) Each inductor is a three turn portion of a continuous solenoid, 10 cm i.d. x 6.4 cm pitch, wound from a 3.8 cm x 0.32 cm copper strip. The 160 kilojoule power supply has a total capacity of 3300 μfd and is capable of providing one millisecond pulses up to 26 kiloamperes in amplitude when charged to 8 kV. An electronic delay circuit synchronizes the triggering of the gas switch with the stabilization of the injected propellant mass flow rate.

II-1-4 Vacuum System

The accelerator exhausts into a dielectric vacuum tank 183 cm long and 92 cm i.d. constructed of Plexiglas and evacuated by a 15.2 cm oil diffusion pump to some 10^{-5} torr before each discharge.(22) An electrically-controlled probe carriage mounted inside the vacuum tank allows remote probing of the arc chamber and exhaust regions in three dimensions. Seven Plexiglas viewing ports mounted flush against the sides and end of the vacuum tank permit unobstructed views of the entire discharge region for optical diagnostics.

II-2 Diagnostic Techniques

The experimental quasi-steady arcjet facility described above is amenable to diagnostic scrutiny by several techniques not otherwise applicable to high power steady state MPD thrusters. Such techniques depend upon the insertion of probes into the discharge plasma. Probe methods take advantage of the enlarged characteristic accelerator dimensions and the pulsed mode of operation by enhancing the spatial resolution of local measurements and permitting interior probing of the otherwise hostile plasma environment. These advantages are counter-balanced to some degree by theoretical ambiguity associated with the reduction of probe data under certain plasma conditions and probe-plasma perturbations.(23,24) Only for those conditions where these effects are negligible will probe methods be fruitful.

The manner in which those variables associated with the acceleration processes examined in this program are determined is discussed in the following sections. These variables include terminal arc voltage, local velocity, magnetic field, current density, and electric field data.

II-2-1 Terminal Arc Properties

The voltage-current (V-J) characteristic of the arc for a given mass flow rate and injection geometry is obtained on a shot-to-shot basis because of the pulsed nature of the device. Arc voltages are measured with respect to the anode ground by a 1000:1 Tektronix high voltage probe attached to the cathode, while the arc current is recorded by a Rogowski loop embedded about the cathode. Both the voltage and current signals are simultaneously displayed upon a Tektronix Type 555 Dual Beam oscilloscope and recorded on high speed Polaroid film. Typical current and voltage signals are presented in Figure 2-2. The shot-to-shot terminal voltage reproducibility is better than ten percent.

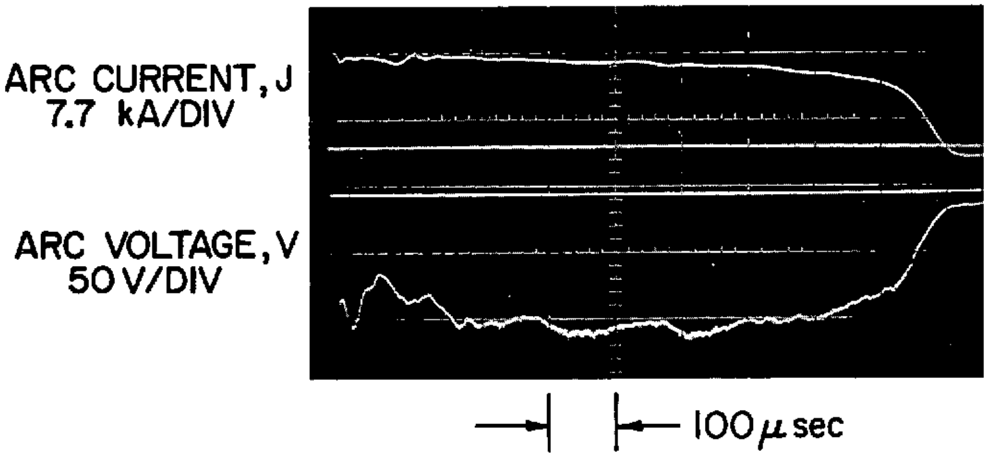

CURRENT AND VOLTAGE SIGNATURES
OF MPD DISCHARGE

FIGURE 2-2

AP25-5044

II-2-2 Local Plasma Properties

II-2-2a Plasma Velocity Vector Field

The complete specification of the velocity vector field requires knowledge of both flow angle and flow speed. These quantities are obtained locally by rather straightforward electric probe techniques.

Plasma streamline directions may be detected by cylindrical double electric probes. The double probe method was originally proposed by Johnson and Malter to measure electron temperature in decaying electrodeless plasma discharges.(25) The double probe consists of two wire electrodes connected to a bias potential source. The current which flows in the probe circuit as the bias potential is increased from zero is expressed in terms of the probe characteristic. For a double probe with equal area electrodes, the probe characteristic is symmetric about the zero current voltage for positive and negative bias potentials.

Experimental double probes are constructed from 0.076 mm tungsten wires enclosed in glass capillary tubes. Length to diameter aspect ratios of 100 insure negligible end effects. Bias voltages are maintained across a 2000 μf capacitor, and probe currents are measured directly with a P6021 Tektronix Current Probe. A typical double probe and signal response are shown in Figure 2-3. A typical probe characteristic is presented in Figure 2-4. The constant probe current magnitude for bias potentials greater than three volts is referred to as the ion saturation current.

In a flowing plasma, the magnitude of the ion saturation current depends on the relative orientation between the flow and the double probe.(26,27) For ratios of probe radius, r_p, to Debye length, λ_d, much greater than one, and supersonic flows, a minimum in probe current as a function of probe

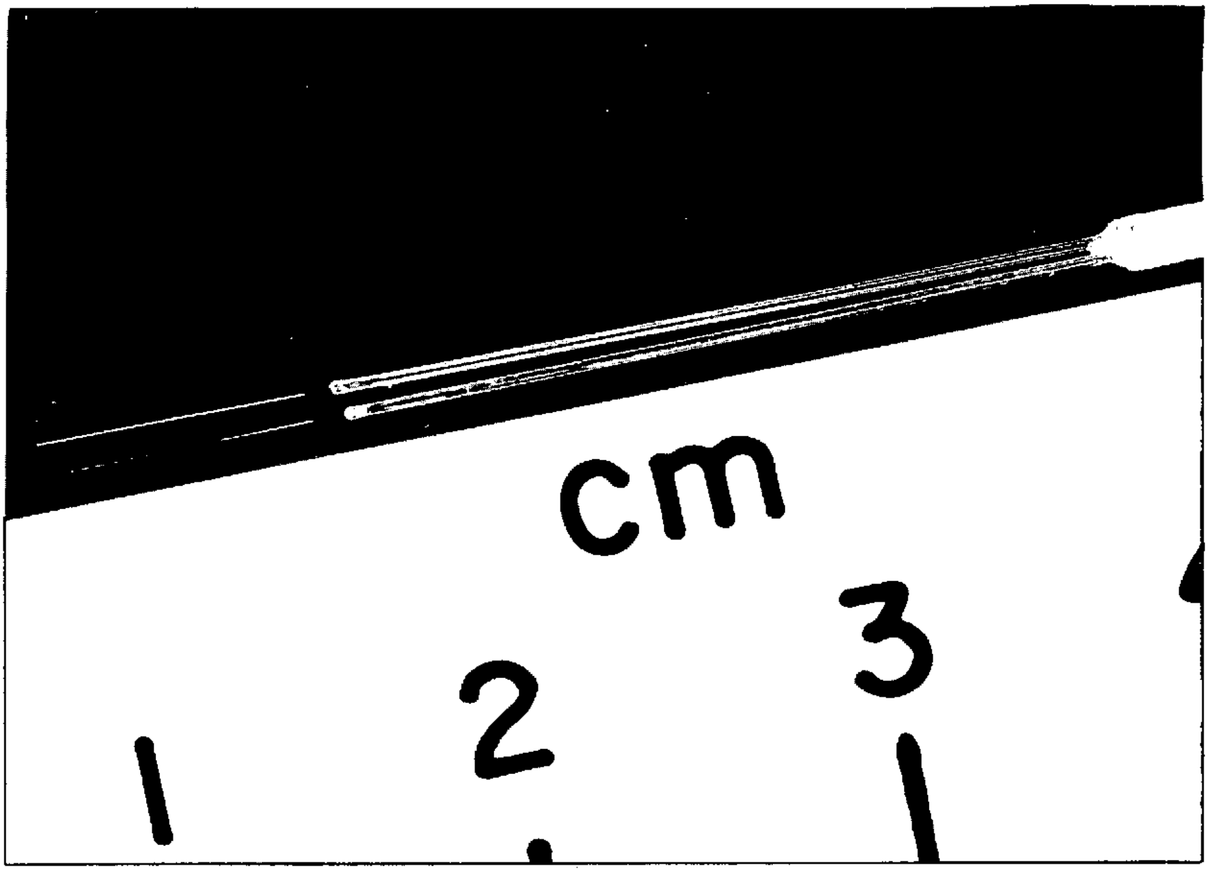

a) DOUBLE PROBE

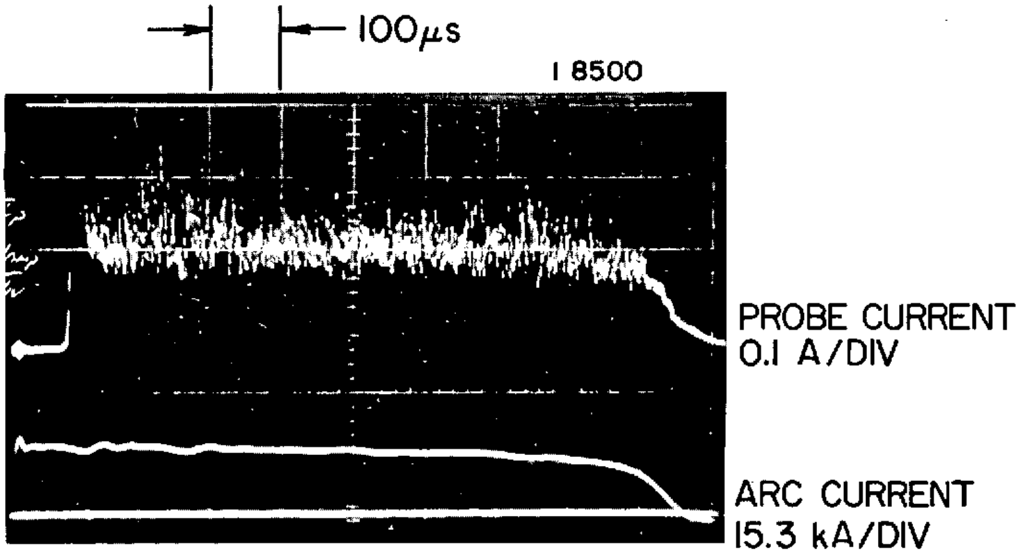

b) TYPICAL DOUBLE PROBE SIGNAL

DOUBLE PROBE

FIGURE 2-3

AP25-P440

FIGURE 2-4
AP25-4818

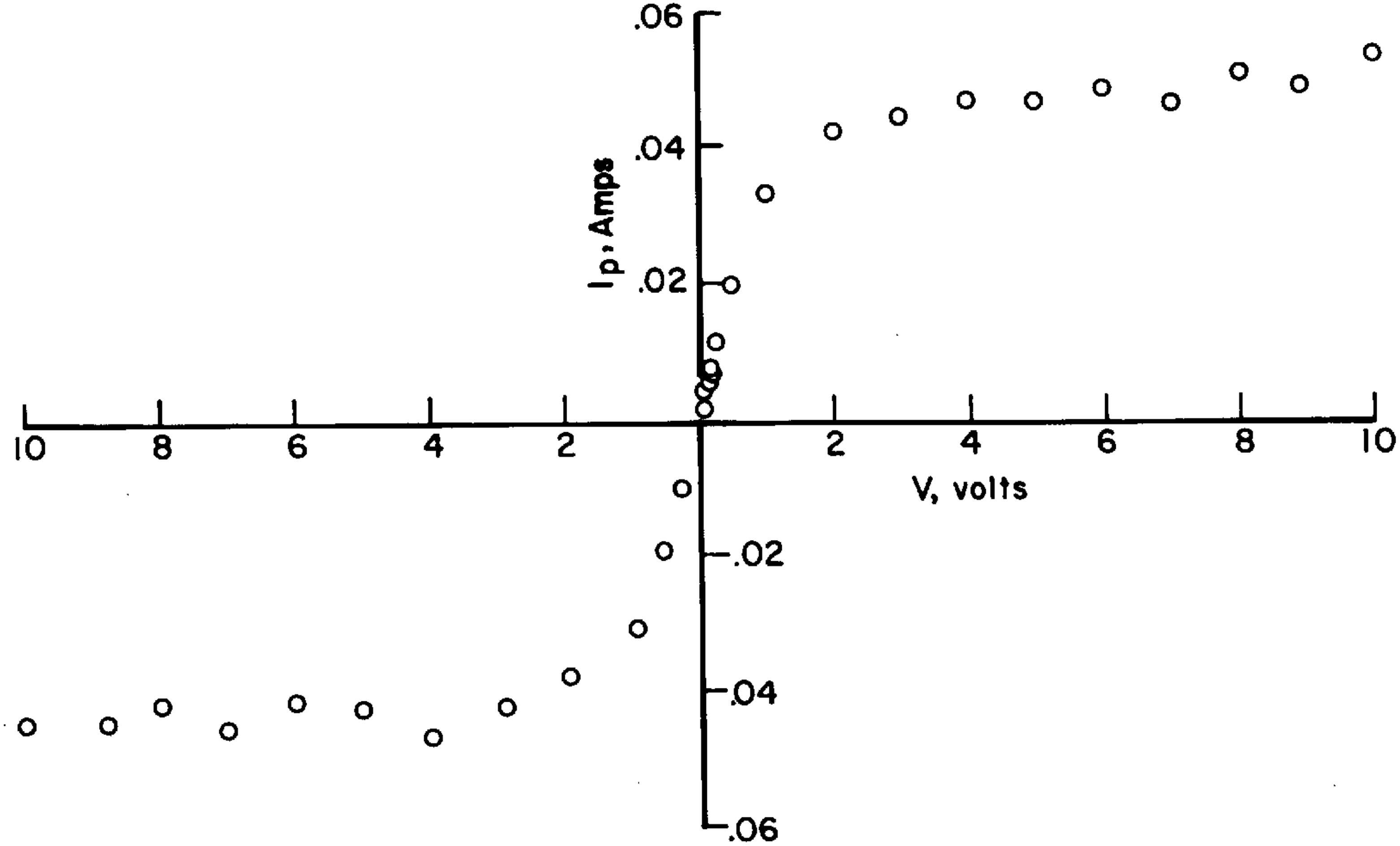

DOUBLE PROBE CHARACTERISTIC

orientation is expected when the local flow vector and the cylindrical probe axis are aligned.(27) For the given probe radii and experimental plasma conditions, r_p/λ_d is greater than 100 and the Mach number $M > 1$. The excellent probe current saturation achieved in the double probe characteristic is also indicative of the large r_p/λ_d ratios. The dependence of net probe current on relative flow angle was verified on the accelerator centerline. In addition, off axis measurements at a position where the flow angle had been previously determined by optical techniques demonstrated excellent agreement between the double probe and optical data.(28) Typical flow angle data are illustrated in Figure 2-5 indicating local flow angle of 20° for that particular location. Local flow direction throughout the discharge may be established in this way. From these data the mass streamlines associated with a given discharge pattern may be constructed.

Double electric probes may be further adapted to measure flow speeds once the streamline pattern of the discharge is known. Plasma velocities are measured using a time-of-flight technique. A pair of double electric probes biased to draw ion saturation current, separated a known distance, and oriented perpendicular to the local flow direction, are used to sense local fluctuations in ion number density which convect with the local streaming velocity.(29) Portions of the upstream and downstream probe signals representative of the quasi-steady phase of the discharge are displayed on an expanded time scale as illustrated in Figure 2-6. Fluctuation arrival times are correlated between upstream and downstream probes and combined with the known probe separation to yield time-of-flight velocities. The plasma velocity may therefore be measured in any region of the MPD discharge where density fluctuations are detectable.

FIGURE 2-5
AP25-4817

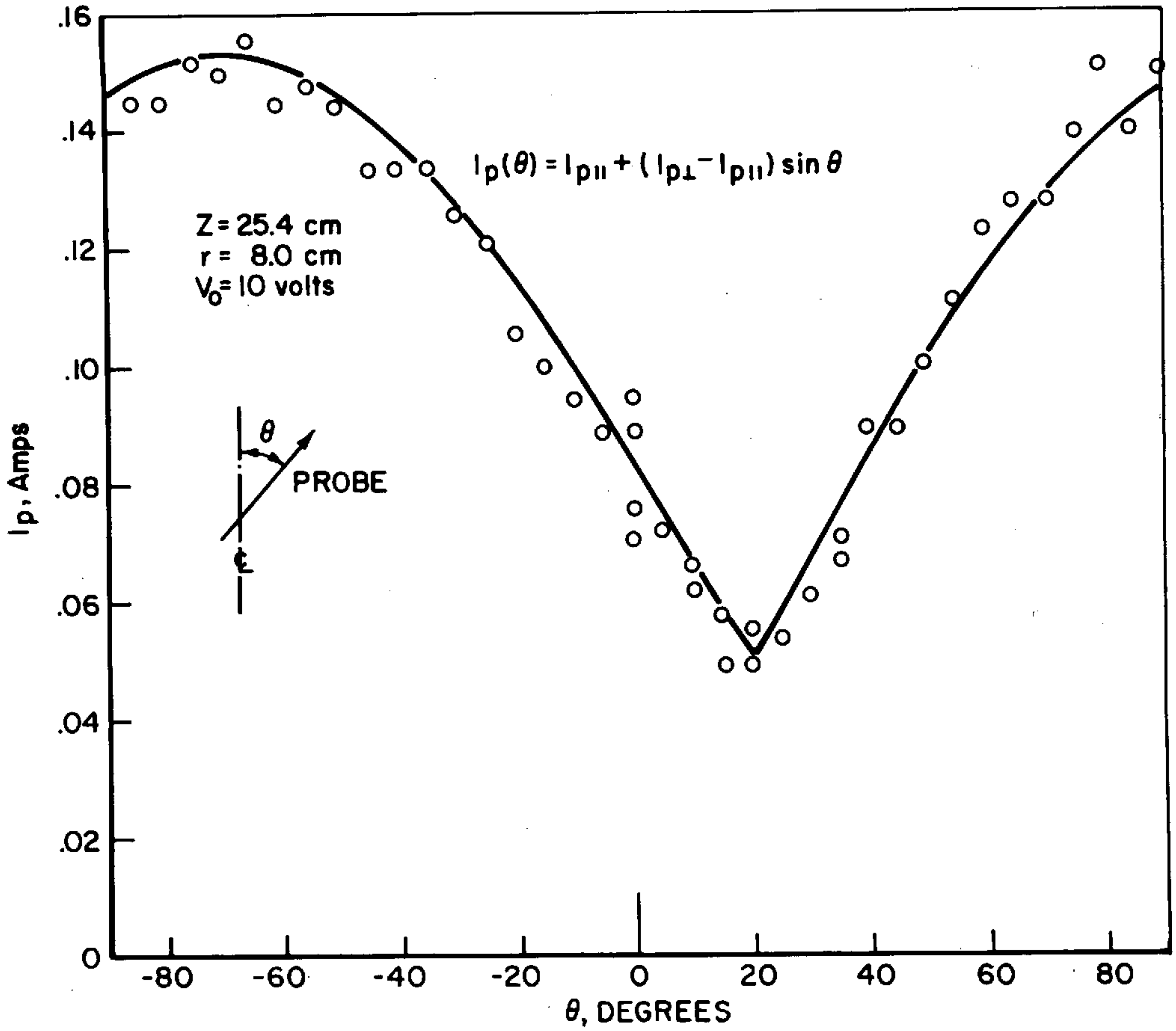

NET PROBE CURRENT DEPENDENCE ON PROBE ANGLE

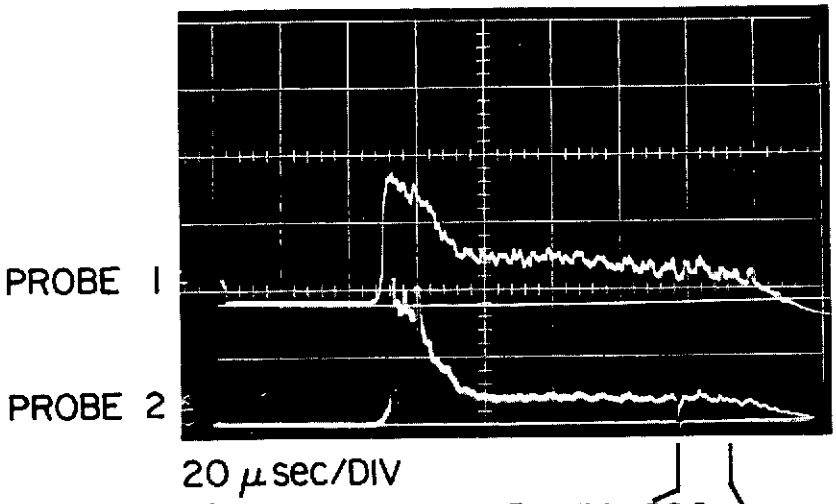

a) TYPICAL PROBE RECORDS

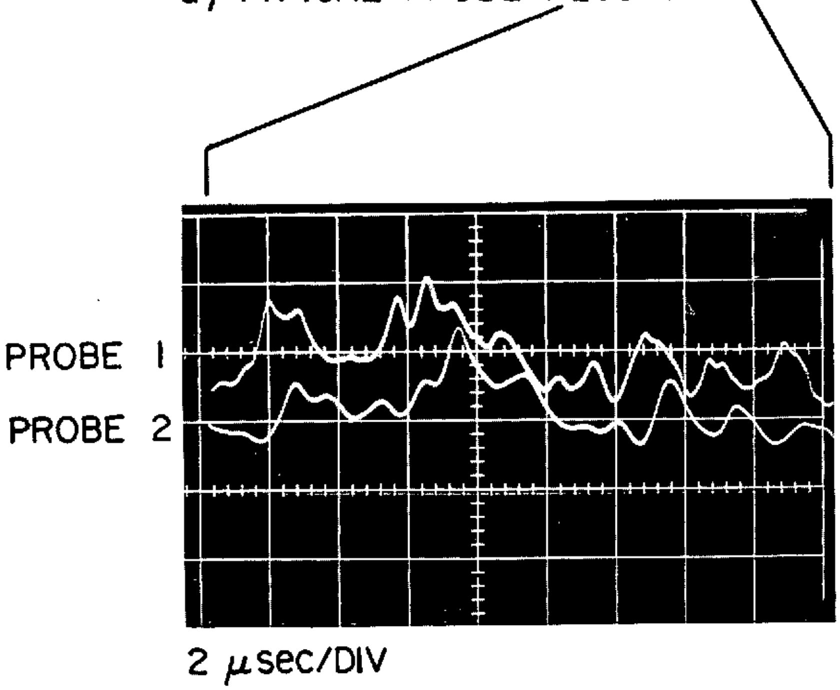

b) EXPANDED TIME

RESPONSE OF BIASED DOUBLE PROBES SHOWING PROPAGATION OF LOCAL FLUCTUATIONS

FIGURE 2-6

Despite the relative ease and straightforwardness of the time-of-flight method, care must be exercised in interpreting the time-of-flight signals. In principle, plasma wave motion could be superimposed upon the convecting plasma stream. In this case, time-of-flight velocities would equal the sum of both a convective and wave speed. To examine this possibility the velocity was measured at several locations in the discharge by three independent techniques, two of which were insensitive to plasma wave components. The velocity data from time-of-flight, ion saturation current, and Doppler shift methods were compared.(30,17) The three measured velocities were found equal within the experimental uncertainty, thereby demonstrating the equivalence between time-of-flight and plasma velocities.

II-2-2b Magnetic Field and Current Density Distributions

The self-induced magnetic field of the quasi-steady MPD discharge is azimuthal in direction. The spatial and temporal distribution of magnetic field may be obtained from induction coils properly aligned to intercept magnetic flux lines. The operation of an induction loop as a magnetic field probe has been excellently reviewed by Lovberg and will not be repeated here.(31) Magnetic field probes consisting of 200 turn coils wound from #44 wire about 2 mm nylon spools provide sufficient sensitivity, frequency response, and spatial resolution to map the quasi-steady B field distribution. Magnetic probe signals proportional to dB/dt are passively integrated through a 10 msec RC integrator and displayed on a Tektronix Type 555 oscilloscope.

The MPD discharge current density distribution may be extracted from the magnetic field data and the $\bar{\nabla} \times \bar{B} = \mu_o \bar{j}$ Maxwell equation. This procedure is discussed further in Section IV-4-2.

II-2-2c Floating Potential Distribution

A single non-biased electrode immersed in a plasma and drawing no net current from the plasma will assume a negative potential due to the disparity between the random electron and ion fluxes to the electrode surface. This potential is defined as the floating potential. The floating potential probes normally used here consist of single tungsten electrodes connected through 1000:1 Tektronix voltage probes to an oscilloscope. The probe circuit impedance of over a megohm guarantees negligible net current will be drawn from the plasma thereby satisfying the floating potential criterion. The tungsten electrode geometry is cylindrical with radii between 0.038 and 0.127 mm and lengths of several millimeters.

Floating potential profiles are of interest only insofar as they reflect the actual space or plasma potential distribution throughout the MPD discharge. To reduce floating potential to plasma potential one must equate proper expressions for the electron and ion current densities incident upon the probe for the given plasma conditions. In general, the relation between floating and plasma potential is a complicated function of ion and electron temperatures, appropriate Knudsen numbers, ion streaming velocities, and probe geometry. Only under a few experimental conditions is this reduction factor accurately known. In lieu of this factor, the space potential profiles may only be approximated by the floating potential distribution.

II-2-3 Optical Discharge Properties

The presence or absence of different species and their spatial distribution in the discharge plasma may be ascertained through several optical diagnostic methods. Discharge photography through selected narrow band spectral filters records the time-integrated luminosity patterns associated with different modes of arcjet operation. 4880 Å (argon II) and 5910 Å (tungsten and continuum radiation) filters are used in conjunction with a Burleigh Brooks Super Cambo 4 x 5 view camera fitted with a Schneider Tele-Xenar 500 mm telephoto lens.

A more precise statement regarding the atomic and ionic species composition of the discharge plasma may be made from spectroscopic data. A Steinheil GH glass prism spectrograph is used to record the radiation over the spectral region from 4200 Å to 6500 Å. The temporal dependence of individual spectral lines during the discharge pulse is monitored by a monochromator-photomultiplier combination. A Bausch and Lomb grating monochromator with a linear dispersion of 16 Å/mm, a RCA IP28 photomultiplier tube, and appropriate focusing optics make up the system.

II-3 Experimental Approach

No attempt has yet been made to optimize the performance characteristics of the arcjet apparatus just described. Rather, the facilities were designed to facilitate diagnostic observation of quasi-steady MPD discharge phenomena. The assortment of diagnostic techniques used in this program and discussed above were specifically chosen to examine certain aspects of the plasma acceleration process. In particular, terminal voltage, exhaust velocity, and spectroscopic data were initially used to assess the arcjet ablation problem. The arcjet configuration was subsequently altered in a manner suggested by these data so as to eliminate the concern over ablation. Later the magnetic, potential, and velocity vector probes were employed to determine the electromagnetic and flow field structure associated with this arcjet configuration. These data were then combined in a plasma acceleration model which suggests several directions in which improvement in arcjet performance may ultimately be realized.

Chapter III

Limiting Phenomena in Quasi-steady MPD Discharges

III-1 Introduction

The proper evaluation of performance data for both steady and quasi-steady MPD arcjets has on occasion been hampered by the perturbing influences of several extraneous phenomena. Ambient mass ingestion into the acceleration zones, insulator and electrode ablation, and the onset of voltage fluctuations all tend to distort performance data, obscure the acceleration mechanisms, and otherwise prevent the evaluation of nominal arcjet operation.(32,33) Of particular importance with respect to eventual space thruster application is the suggestion that the quasi-steady MPD arc may be fundamentally limited in attainable specific impulse and thrust power efficiency. To assess this question, it becomes imperative to develop a quasi-steady arcjet configuration whose operation is uninfluenced by extraneous factors. Given this configuration, the terminal voltage, exhaust velocity, and other pertinent arc variables may then be measured to clarify the nature of the acceleration process and determine the extent and nature of any limitation in the quasi-steady arcjet's performance.

Multimegawatt quasi-steady arcjet operation tends to produce serious insulator ablation, which must be properly accounted for in evaluating the arcjet's high-power performance characteristics, and must be virtually eliminated before long-term thruster operation can be contemplated. This chapter describes investigations of the manner in which the arc voltage and exhaust velocity of a quasi-steady MPD arc are affected by the introduction of the ablation products into the discharge and exhaust stream, and techniques for eliminating such effects.

High current operation of quasi-steady MPD arcjets also tends to be characterized by erratic, non-steady terminal voltage behavior. The second half of this chapter discusses this effect in terms of phenomena occurring in the vicinity of the arcjet's electrodes.

Finally, the criteria are summarized which when satisfied allow nominal MPD arcjet operation to ensue, free from the perturbing effects outlined above.

III-2 Insulator Ablation Background

Earlier studies of the ablation of Plexiglas insulating surfaces within the quasi-steady MPD arc at Princeton established that spectral lines of ionized carbon, oxygen and neutral hydrogen, the atomic constituents of Plexiglas, were prominently present in spectrograms of the discharge plasma.(17,34,35) Insulator ablation was further visually evidenced by the marked erosion of the Plexiglas surfaces after repeated firings of the arc. A more detailed examination of the MPD exhaust in which the exhaust plume was photographed through a series of narrow band spectral line filters revealed an azimuthally nonuniform species structure previously undetected by other diagnostic techniques.(17) Jets of ionized argon propellant aligned with the arc's mass injection orifices azimuthally alternated with jets of the ionized products of Plexiglas ablation. The entire jet structure surrounded a central core of ablation material. In addition, this arc structure depended on the ratio of the square of the arc current to the mass flow rate, $J^2/\dot{m}$, a parameter thought to demark regions of "starved" and "overfed" MPD arc operation. For "overfed" conditions the degree of ablation was significantly reduced, and the exhaust structure became correspondingly less pronounced. For "starved", highly ablative arc operation, the jets were more sharply delineated.

The following three sections describe in further detail the manner in which insulator ablation affects the terminal voltage and the exhaust velocity of the arc. Actually, several categories of ablation need be distinguished, according to the effects produced relative to nominal MPD arc operation. Ranked in descending degrees of ablation, we define domains of: (1) "ablation dominated" operation implying ablation-dominated terminal voltages and ablation-dependent velocities; (2) "reduced ablation" where only the exhaust velocities are affected; (3) "trace ablation" where the quasi-steady arc characteristics are independent of insulator material, but the presence of ablated species in the discharge is detected spectroscopically; and (4) "no ablation" detectable in any fashion.

III-3 Effects of Insulator Ablation on the Voltage-Current Characteristic

For a given accelerator geometry, current level, and input mass flow rate and distribution, the voltage-current characteristic of the MPD arc indicates the electric potential required to drive that current between the anode and cathode in the presence of plasma resistivity, plasma flow, magnetic fields and electrode sheaths. The terminal arc voltage may be expressed as the sum of ohmic, motional emf, Hall and electrode fall terms given by the generalized Ohm's law:

$$V = \int_c^A \frac{\bar{j} \cdot \overline{dl}}{\sigma} - \int_c^A (\bar{u} \times \bar{B}) \cdot \overline{dl} + \int_c^A \frac{(\bar{j} \times \bar{B}) \cdot \overline{dl}}{n_e e} + V_F \qquad (3\text{-a})$$

where $\int_c^A \overline{dl}$ implies integration along any convenient contour from the cathode to anode sheath surfaces, and V_F equals the sum of the anode and cathode falls. Order of magnitude estimates for the plasma environment of this study indicate that additional contributions to the voltage due to electron pressure gradients and ion slip are negligible.

The expected functional form of the voltage-current characteristic may be approximated apriori by considering the operational modes of the accelerator. As the arc current is increased for a given mass flow rate, the MPD arcjet undergoes a transition from an electrothermal to an electromagnetic mode.(36) For sufficiently low currents such that the $\bar{j} \times \bar{B}$ body forces within the discharge are negligible, the arc current resistively heats the discharge plasma. The creation and subsequent expansion of a resistively heated, high enthalpy plasma characterizes electrothermal plasma acceleration. Because resistive heating phenomena dominate the electrothermal mode, electrothermal terminal voltages should accordingly scale as the ohmic integral $\int \frac{\overline{j \cdot dl}}{\sigma}$ in the generalized Ohm's law. In this regime, where the degree of ionization is greater than 10^{-3}, σ equals the Spitzer conductivity which is a function of the electron temperature and the Coulomb logarithm.(37) Since changes in the electron temperature and Coulomb logarithm are small to first order in this regime, the plasma conductivity may be approximated as constant.(38,42,44) For this case, electrothermal terminal voltages will scale linearly with arc current.

As the total arc current is increased, the self-induced magnetic field B becomes increasingly more significant. The predominance of the Lorentz $\bar{j} \times \bar{B}$ body forces over Joule heating components distinguishes the electromagnetic and electrothermal modes of arcjet operation. In the Ohm's law formulation of the V-J characteristic, the electromagnetic component of arcjet operation appears as the motional emf integral $\int (\bar{u} \times \bar{B}) \cdot \overline{dl}$. Since the self-magnetic field is proportional to the current J, the back emf term will scale as uJ. In the electromagnetic mode the exhaust velocity is related to the current through the self-field thrust equation discussed in Chapter I.

$$T = \dot{m}\, u = b\, J^2 \qquad (3\text{-b})$$

For a mass flow independent of current the average exhaust velocity will scale as J^2 implying a J^3 arc voltage dependence is associated with the electromagnetic mode of arcjet operation. Thus, as the arc current is increased, one would expect the terminal voltage to experience a change from a linear to a cubic dependence upon the current, indicative of the transition from an electrothermal to an electromagnetic mode of arcjet operation.

The V-J characteristic for the quasi-steady MPD arc operating with a six-hole Plexiglas insulator end plate and a total mass flow rate of 6 g/sec is presented on a log-log scale in Figure 3-1. (All arcjet configurations discussed in Sections III-3 through III-5 operate with a common conical cathode geometry, 2.54 centimeters in length and 1.9 centimeters in base diameter.) The argon propellant is injected axially into the discharge chamber through six 0.48 cm orifices symmetrically distributed about the 2.54 cm radius as illustrated in Figure 3-4a. Superimposed upon the voltage data in Figure 3-1 are solid lines whose slopes correspond to the asymptotic behavior of the electrothermal and electromagnetic terminal arc voltages discussed above. The Plexiglas characteristic may be divided into three separate regions shown in Figure 3-1. (I) a low current region where the arc voltage is proportional to the current, (II) an intermediate current region characterized by a voltage porportional to the cube of the current, and (III) a high current region where the arc voltage scales linearly with the current. It is proposed that the functional behavior of the voltage with current within the three regions of the Plexiglas V-J charactristic indicates respectively, electrothermal, electromagnetic, and ablation-dominated modes of operation.

The expected arcjet transition from electrothermal to electromagnetic modes is indicated by the observed functional current dependencies in regions I and II of the characteristic. The abrupt transition between regions II and III, however, represents an unexpected deviation from nominal arcjet behavior.

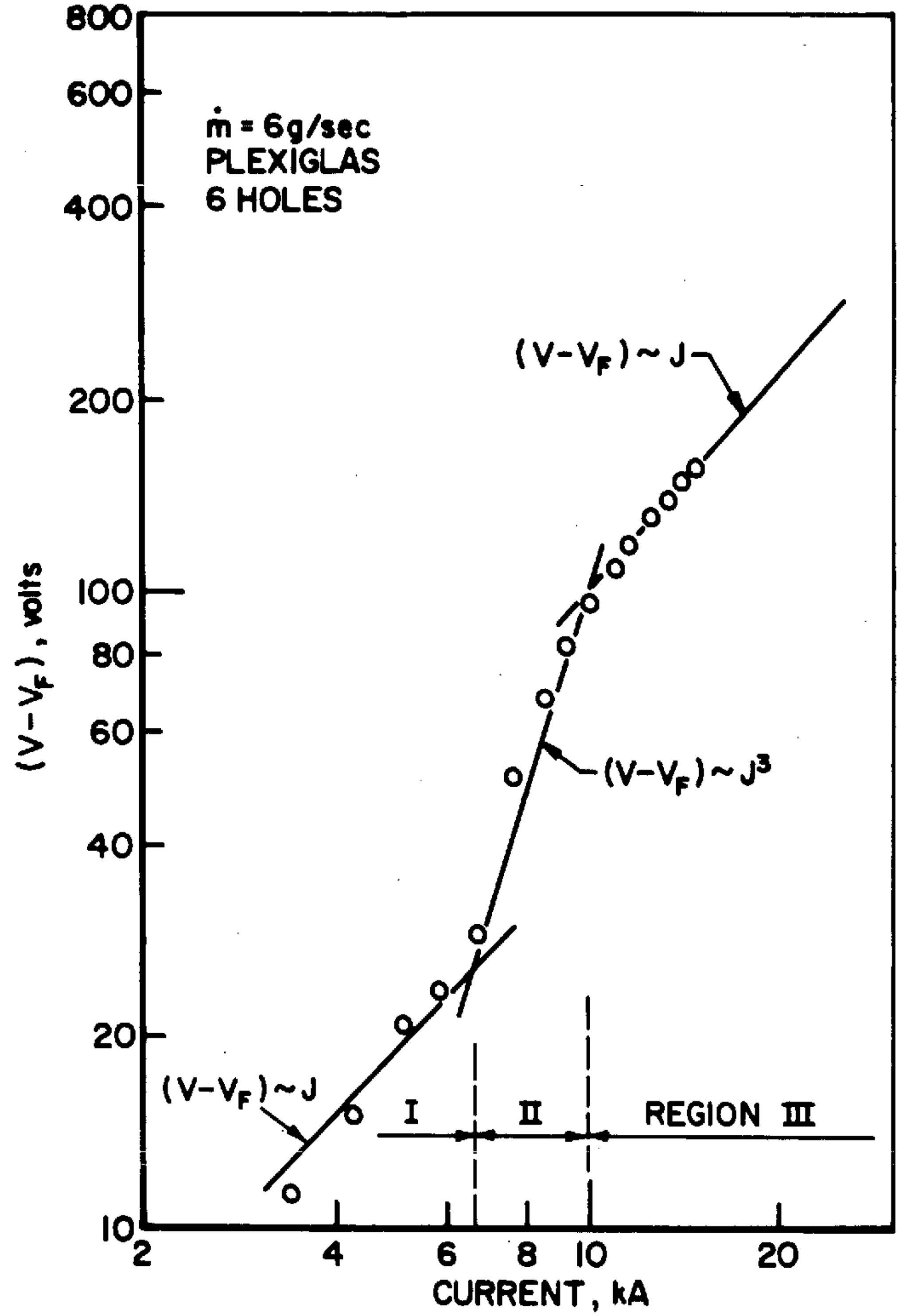

V-J CHARACTERISTIC, SIX-HOLE, PLEXIGLAS

FIGURE 3-1

AP25-4963

This second transition at approximately 10 kA is believed to be associated with insulator ablation. As postulated above, high current arcjet operation is characterized by an arc voltage proportional to the motional emf term of Ohm's law, and it seems reasonable to expect the voltage transition between region II and region III to be due to the onset of phenomena which affect the functional variation of the exhaust velocity with current. Quasi-steady thrusters using ablated electrode material as the propellant are found to ablate mass flow proportional to the square of the current.(39) For such thrusters the self-field thrust Equation 3-b implies that exhaust velocities should be independent of arc current, and indeed, velocity measurements in the "starved", highly ablative region III of our Plexiglas characteristic indicate the average exhaust velocity is independent of current.(14) It follows, then, that ablation-dominated terminal arc voltages will scale linearly with arc current. One concludes that region III of the Plexiglas characteristic represents an ablation-dominated regime of arcjet operation. Since the quasi-steady MPD arcjet is intended to operate in a non-ablating mode, the decision was made to eliminate rather than to account for the cause and effects of the insulator ablation.

For given levels of incident thermal energy flux, refractory insulating surfaces are less prone to ablate than Plexiglas surfaces. Accordingly, boron nitride was substituted for Plexiglas because of its higher thermal diffusivity and ablation temperature. In Figure 3-2 the voltage-current characteristic for the same mass injection configuration and mass flow rate as above is now shown with boron nitride as the insulator material instead of Plexiglas. Regions I and II appear much the same as in the Plexiglas case, but no similar transition to region III of ablation-dominated voltages is seen in the boron nitride case. Instead, the high current regime, $J \gtrsim 10$ kA, continues to

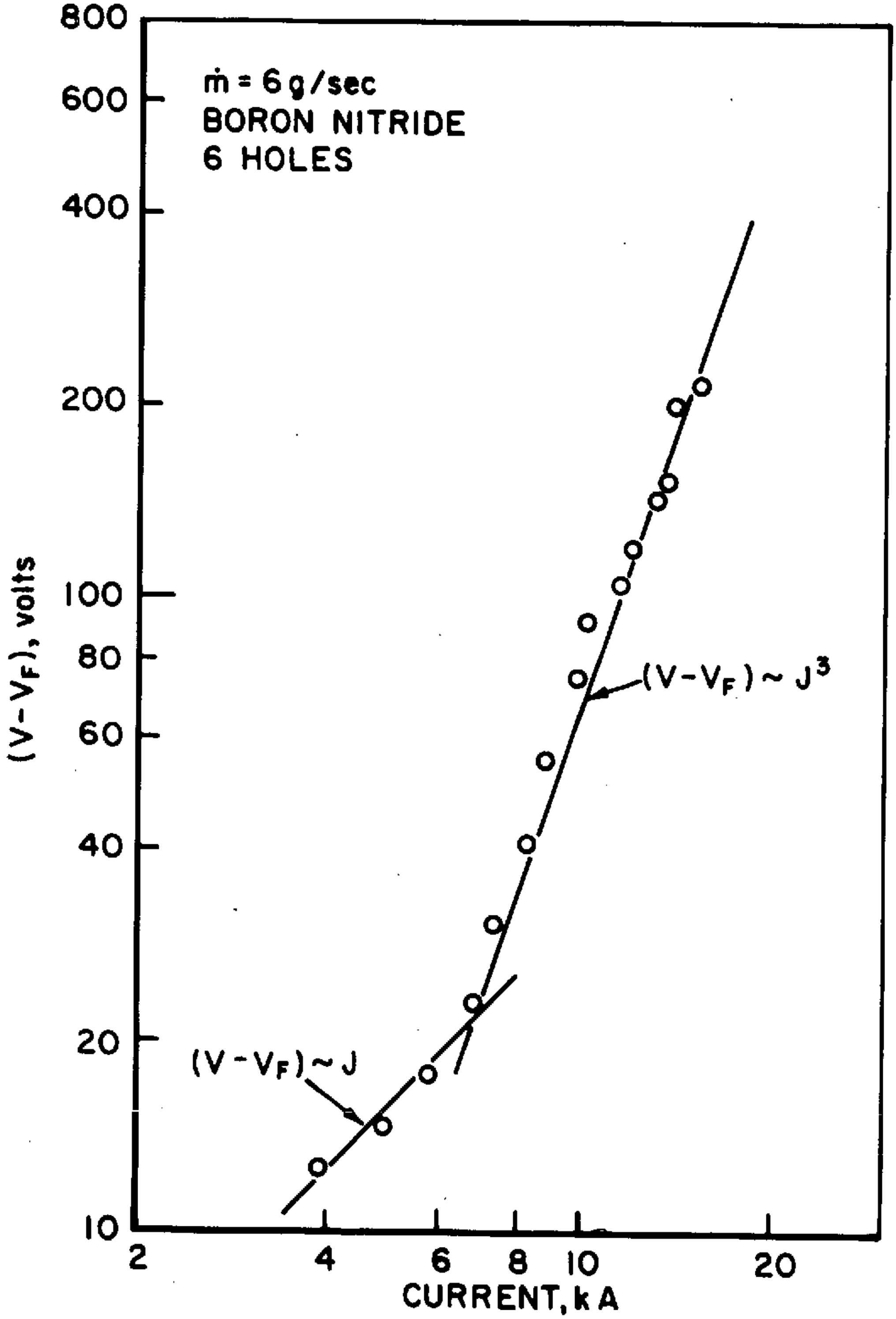

V-J CHARACTERISTIC, SIX-HOLE, BN

FIGURE 3-2
AP25·4965

be characterized by a J^3 voltage dependence in spite of spectral evidence of ionized boron and nitrogen in the discharge plasma. Apparently the refractory nature of the boron nitride insulation reduces the degree of ablation to such an extent that the terminal voltages are no longer ablation-dominated.

It is also found in the boron nitride experiments that the azimuthal jet structure of the discharge seen with Plexiglas is no longer evident. As described below, however, significant effects on the jet velocity remain. That is, use of boron nitride insulation within the MPD arc chamber reduces the degree of ablation from the previous "ablation-dominated" level to ablation category (2), "reduced ablation".

III-4 Effects of Insulator Ablation on the Exhaust Velocity

Insulator participation in MPD arcjet processes was originally suggested by examination of the radial profiles of exhaust velocity and species distribution for an arcjet operating at 15.3 kA with 6 g/sec argon injected through a six-hole Plexiglas end plate.(14) The radial velocity profile of Figure 3-3 is taken at a downstream position near the end of the electromagnetic acceleration region where magnetic field measurements show that 90% of the total arc current flows upstream of this point. The plasma velocities are measured using a time-of-flight technique (Section II-2-2a). The profile consists of a central core region with an average plasma velocity of 21.0 km/sec and an outer annular region with an average velocity of 8.8 km/sec. Superimposing Bruckner's radial species distribution(17) upon this velocity profile, the ablation products of the Plexiglas insulator (carbon, oxygen, and hydrogen) are found to occupy the central core while the injected argon propellant occupies the outer region. It is therefore legitimate to ask whether this velocity profile, particularly the high speed central core, is reflective of a normal $\bar{j} \times \bar{B}$ body force distribution or is a consequence of ablation and the particular insulator material employed within the arc chamber.

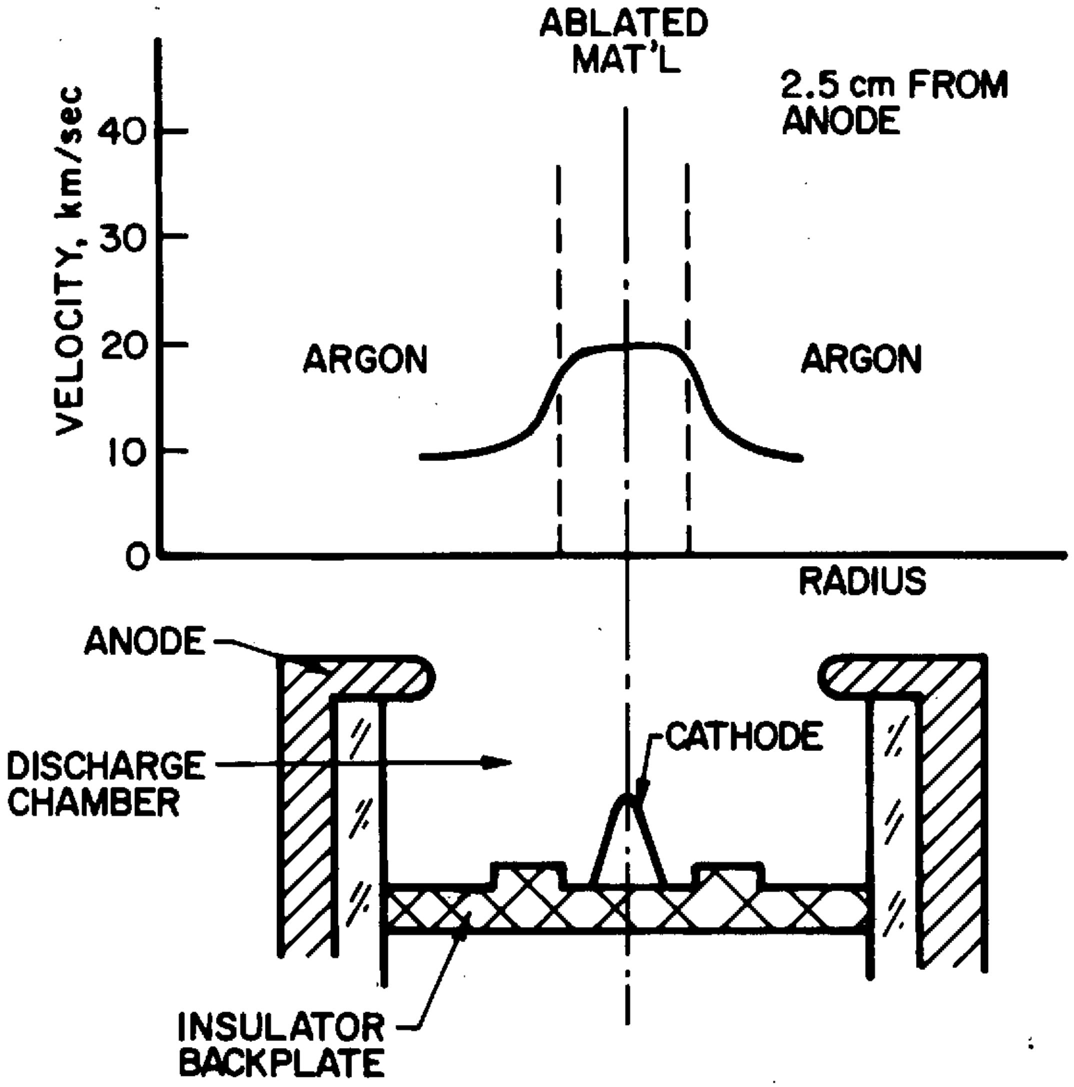

RADIAL DISTRIBUTION OF PLASMA SPECIES AND VELOCITY, $J = 15.3$ kA, $\dot{m} = 6$ g/sec, SIX-HOLE PLEXIGLAS

FIGURE 3-3
AP25-4966

The continuum nature of the discharge plasma just downstream of the anode orifice allows the centerline plasma, consisting of the ionized products of Plexiglas dissociation (carbon, oxygen, and hydrogen - $C_5H_8O_2$), to be treated as a monofluid with an effective ion mass equal to the weighted average atomic mass of the ablation products.

$$m_{plex} = \frac{5m_c + 8m_h + 2m_o}{15} = 6.7 \text{ a.m.u.} \qquad (3\text{-c})$$

The mass of an argon ion, m_a, is 40 a.m.u. The ratio of the inverse square root of these ion masses equals within 2½ % the experimentally measured velocity ratio. That is to say,

$$\frac{u_{plex}}{u_a} = \left(\frac{m_a}{m_{plex}}\right)^{\frac{1}{2}} \qquad (3\text{-d})$$

From this it may be inferred that the exhaust velocities exhibit an inverse square root dependence on the mass of the species being accelerated. Similar observations have been made in steady state devices operating with bi-species propellants.(49) This mass dependence will henceforth be employed in an empirical spirit as an indicator of ablation's influence on the exhaust velocity. The high centerline velocity associated with the Plexiglas configuration thus appears to be a consequence of the low average atomic mass of the centerline plasma, and therefore a direct result of insulator ablation. Hence, region III of the six hole Plexiglas V-J characteristic is classified as "ablation-dominated" in that both the arc voltage and exhaust velocity are ablation-dominated.

When boron nitride is substituted for the Plexiglas insulation for the same six-hole mass injection geometry, the time-of-flight velocity on the centerline where spectrograms of the discharge indicate ionized boron and nitrogen are confined, is

16.0 ± 6.0 km/sec. As before, the centerline "boron nitride" plasma may be treated as a monofluid with an effective ion mass of 12.4 a.m.u. Accordingly, Equation 3-d predicts a centerline "boron nitride" plasma velocity of 15.6 km/sec. Thus it appears that even though boron nitride insulation reduces the degree of ablation to the extent that the terminal arc voltage is no longer ablation-dominated, the insulator material continues to affect nominal MPD arc operation through its influence on the exhaust velocity for this combination of operating conditions, insulator material and mass injection geometry.

In a further attempt to eliminate the insulator affect upon the exhaust velocity, the manner in which the propellant is injected into the discharge chamber was next explored.

For the six-hole mass injection configuration, visual and spectroscopic data suggest that the insulator ablation is most severe about the base of the centrally located cathode. This is to be expected since the inverse radial dependence of the current density tends to maximize the thermal energy flux from the plasma to the insulating surfaces about the base of the cathode. In addition, the lack of injected argon propellant about the cathode base may create locally "starved" regions which in turn tend to encourage insulator ablation.

Therefore, in an attempt to supply argon propellant to the cathode region and remove solid insulator surfaces from the vicinity of the cathode, a revised boron nitride annular cathode base mass injection configuration was designed and constructed. The annulus channel, one side of which is the rear side of the cathode itself, is angled at 45° to provide a radial component of injected propellant flow, as shown in Figure 3-4b.

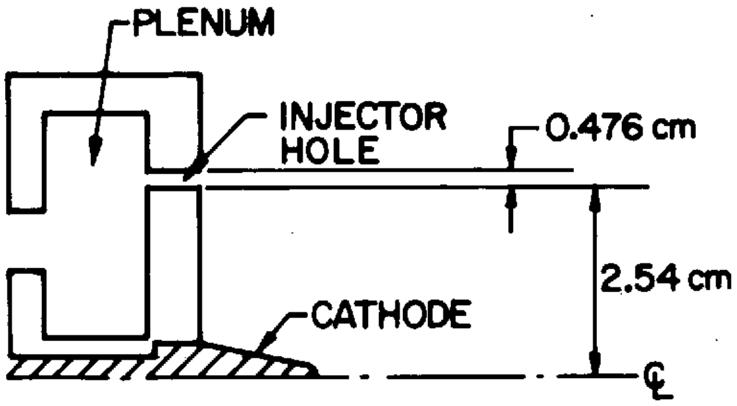

a) 6 HOLE GEOMETRY

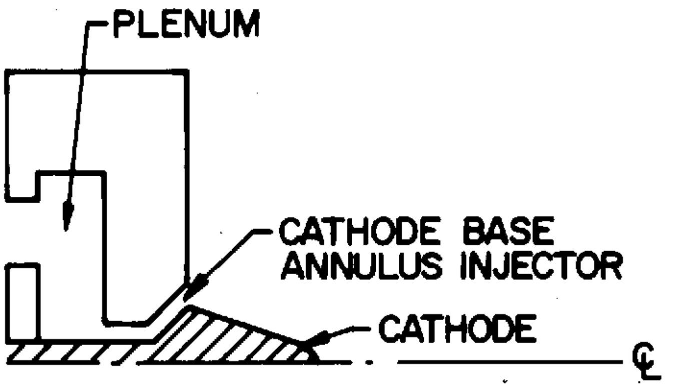

b) ANNULAR CATHODE BASE GEOMETRY

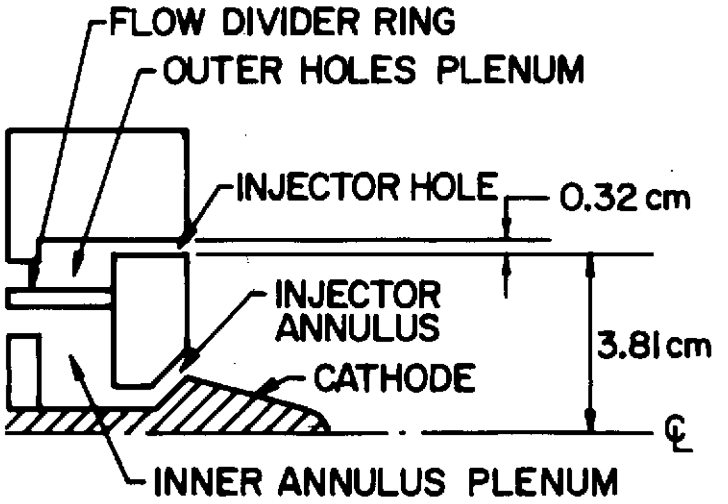

c) 12 HOLE CATHODE ANNULUS GEOMETRY

MASS INJECTION CONFIGURATIONS

FIGURE 3-4

AP25-4964

Figure 3-5 is the measured V-J characteristic for this boron nitride annular cathode base injection geometry for an argon mass flow rate of 6 g/sec. Again, a line indicative of the electromagnetic accelerator mode is superimposed upon the terminal voltage data. The revised injection geometry still shows no tendence toward transition to ablation-dominated operation in the high current regime. It is also interesting to note that region I of the V-J characteristic has been eliminated and the low current regime now exhibits the cubic dependence of region II. This may suggest that mass injection directly into regions of maximum $\bar{j} \times \bar{B}$ body force helps promote the dominance of the electromagnetic mode of arcjet operation even for relatively low values of total arc current. Even though discharge spectra at $J = 15.3$ kA, $\dot{m} = 6$ g/sec continue to indicate the presence of BII, BIII, NII and NIII in the discharge for this new configuration, the centerline exhaust velocity is now measured to be 9.0 km/sec, Figure 3-6, suggesting this injection geometry is capable of reducing ablation to a "trace" level where the exhaust velocity is no longer ablation-dominated.

In summary, the combination of an annular cathode base mass injection geometry and a refractory boron nitride insulator result in an arcjet configuration whose voltage characteristic and exhaust velocity are independent of insulator material. However, this has been achieved at the cost of higher terminal voltages as seen in comparing the absolute magnitudes of the arc voltages for the two different boron nitride injection geometries. For example, at $J = 10$ kA the six-hole geometry voltage is 95 volts, where at the same current the annular cathode base BN geometry operates at a terminal voltage of 320 volts. Such a dramatic increase in the terminal voltage for a given current implies a significant change in arcjet operation. The effort to reduce this terminal voltage while maintaining MPD arcjet operation independent of insulator material will now be discussed.

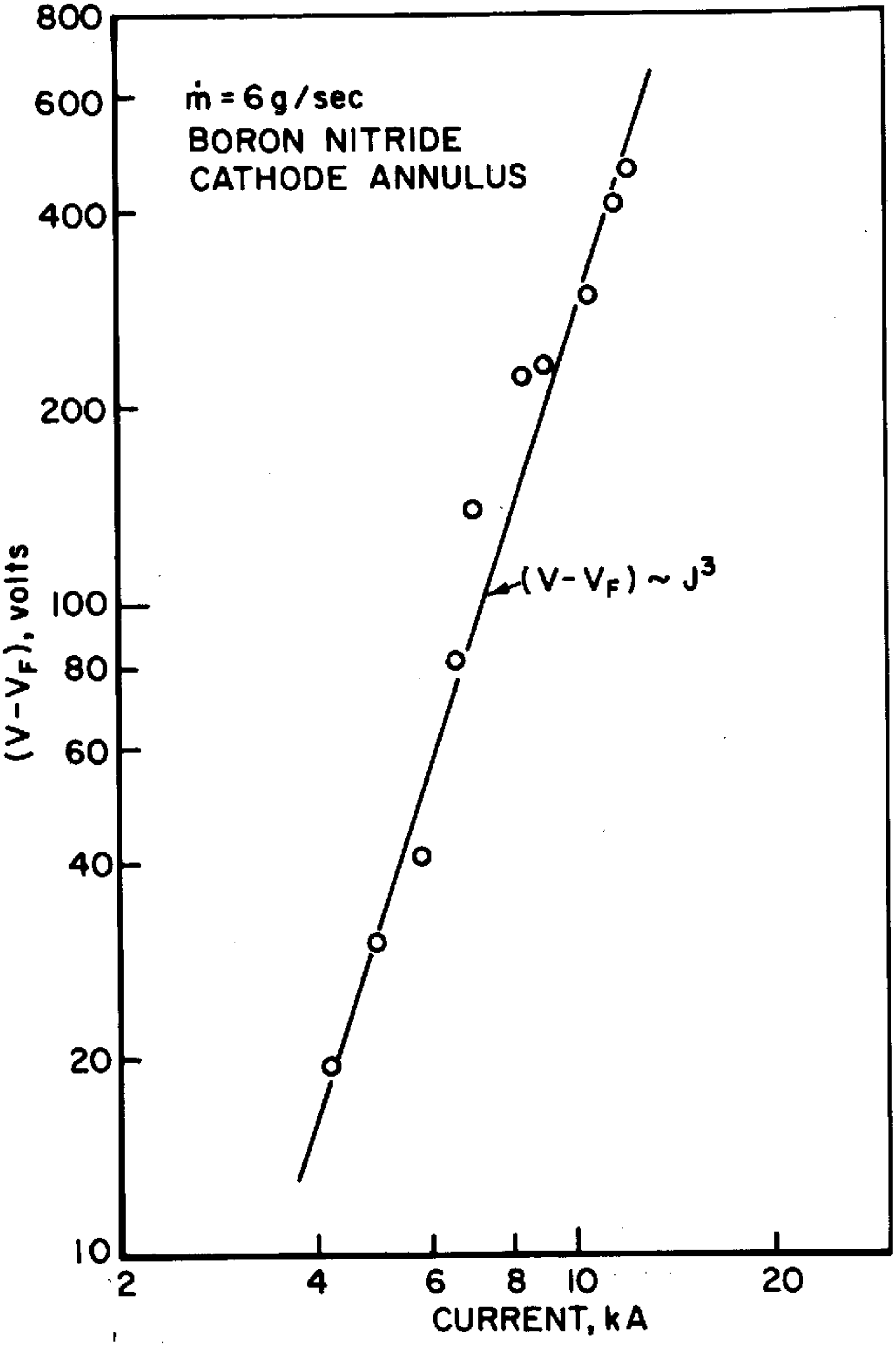

V-J CHARACTERISTIC, CATHODE ANNULUS, BN

FIGURE 3-5
AP25·4967

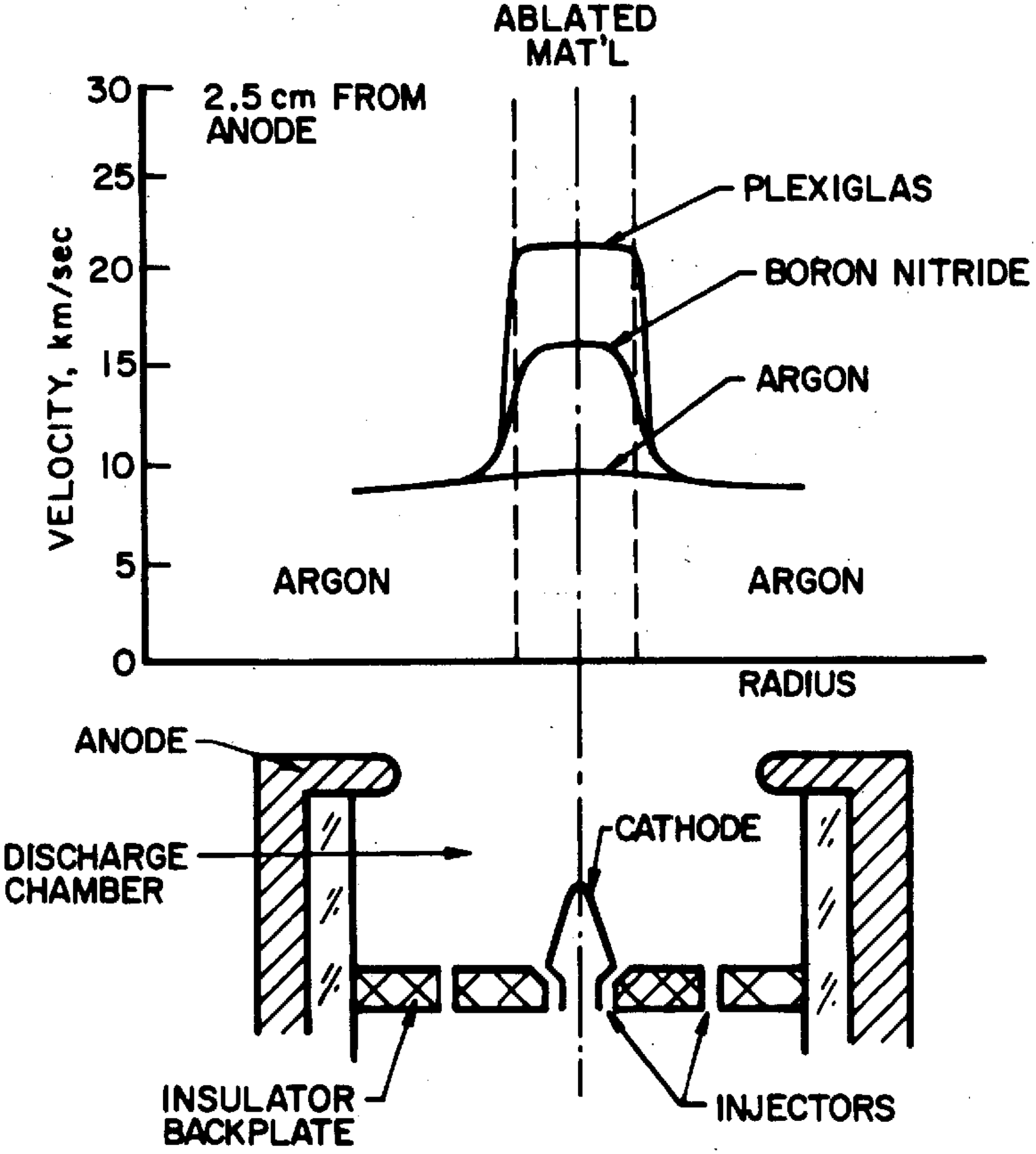

PLASMA CENTERLINE VELOCITIES
J = 15.3 kA , $\dot{m}$ =6g/sec

FIGURE 3-6
AP25-5045

III-5 Effects of Mass Injection Geometry on Terminal Voltage and Exhaust Velocities

For a given current, mass flow, and exhaust velocity, MPD arcjet efficiency is inversely proportional to the terminal arc voltage. Thus MPD arcjet operation at the lowest possible terminal voltage becomes desirable. The empirical experience outlined above suggests that some combination of large and small radius mass injection configurations might provide both lower voltages and arc operation independent of insulator material. To explore this possibility, floating potential surveys were taken for both injection geometries at $J = 9$ kA, $\dot{m} = 6$ g/sec. to identify regions of relative voltage increase.

Potential measurements begin a millimeter from the anode in the anode plane, proceed radially inward to the centerline, and then axially inward to a position a millimeter from the cathode tip. The floating potentials, uncorrected for electron temperature gradients, ion flow, collisional, and magnetic field effects,are plotted as a function of radial and axial location along the path described above in Figure 3-7. The anode fall potentials, defined as the potential measured at the one millimeter radial position, are equal for both injection configurations. The most pronounced difference between the two profiles is found in the steep interelectrode voltage gradient for the annular cathode base injection geometry case.

This voltage gradient suggests that a local starvation of injected propellant exists in the outer anode regions of the discharge, an effect elsewhere observed to have a strong influence on the terminal voltage.(19) The cathode base injection configuration apparently tends to concentrate injected mass about the centerline, whereas mass injection at a larger radius (six-hole injection geometry) provides relatively more mass in the outer anode regions of the discharge.

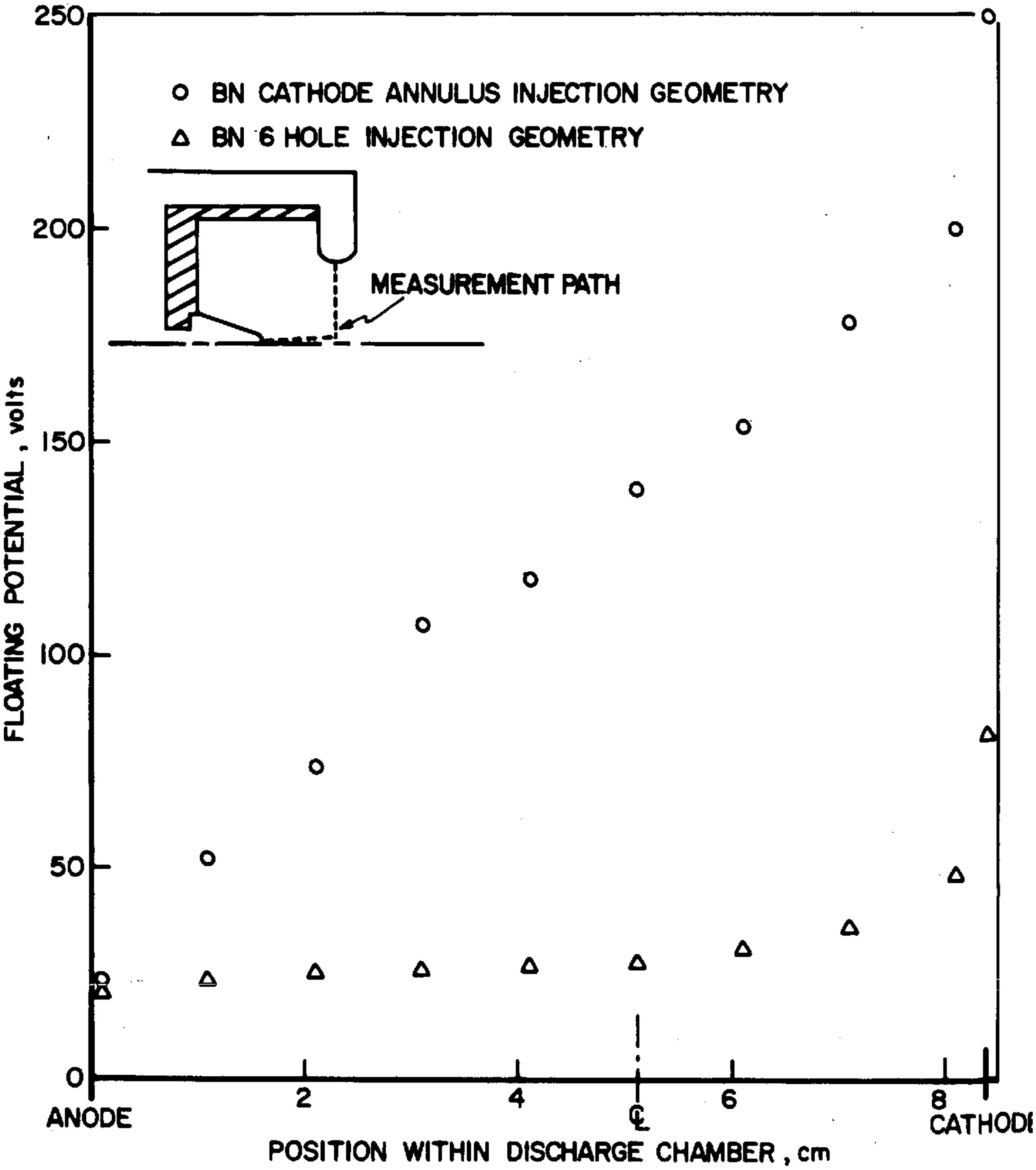

FLOATING POTENTIAL DISTRIBUTIONS

$J = 9.0$ kA, $\dot{m} = 6$ g/sec

FIGURE 3-7

AP25·4968

In light of these results, it seemed reasonable to assume that a combination of the two previously employed mass injection configurations would act to reduce the terminal voltage. In order to determine the optimum flow division between the outer radial region and the inner cathode region of the discharge chamber, a new boron nitride mass injection geometry was designed as illustrated in Figure 3-4c. Twelve 0.32 cm holes symmetrically distributed about a 3.81 cm radius assure a uniform mass distribution in the vicinity of the anode. A 45° cathode base annulus similar to one used previously allows argon propellant to be delivered about the cathode. A flow divider ring establishes two independent plenum areas so that the mass flow division between inner annulus and outer holes can be controlled. The percentage flow division is monitored by varying the relative area ratios of the choked orifices feeding the two independent plenums. In such a manner the entire range of flow division between 100% inner flow; 0% outer flow (designated by 100:0) to 0% inner flow; 100% outer flow (0:100) may be spanned.

The V–J characteristics at 6 g/sec as a function of flow division are shown in Figure 3-8. It is seen that the functional dependence of arc voltage on arc current is itself dependent on flow division in the low current regime and independent of flow division in the high current regime. Region I continues to scale as voltage proportional to current,and region II as the cube of the current. The voltage as a function of percent flow through the inner annulus is presented in Figure 3-9 for currents of 5, 10, and 15 kA and a mass flow rate of 6 g/sec. At the lowest current the voltage appears to be insensitive to flow division, whereas at the high currents the voltage monotonically increases with % flow through the inner annulus. Thus, to minimize arc voltage it behooves one to operate as far to the left on the curves of Figure 3-9 without reintroducing the ablation-dominated

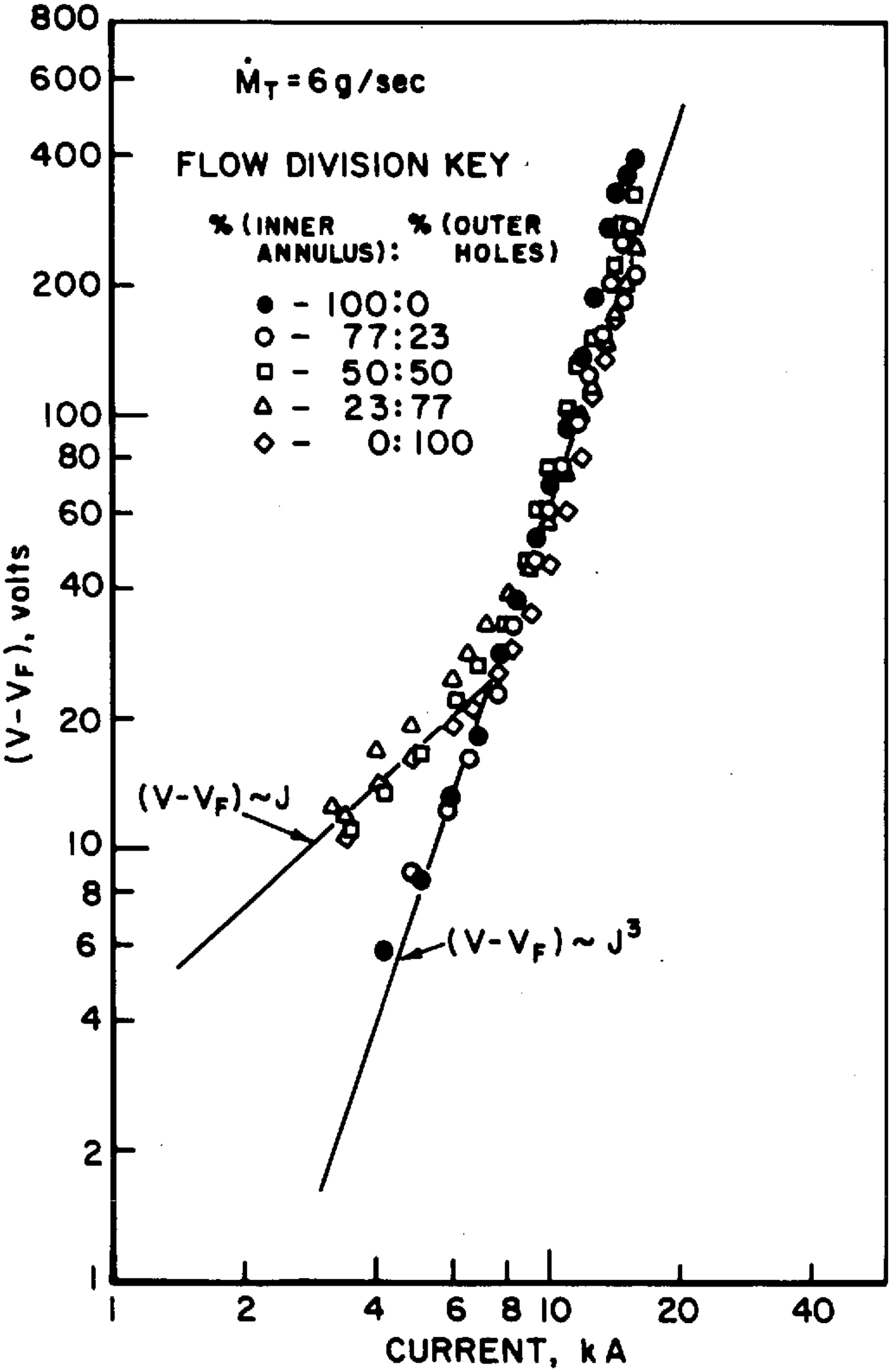

V-J CHARACTERISTICS vs FLOW DIVISION

FIGURE 3-8
AP25-4969

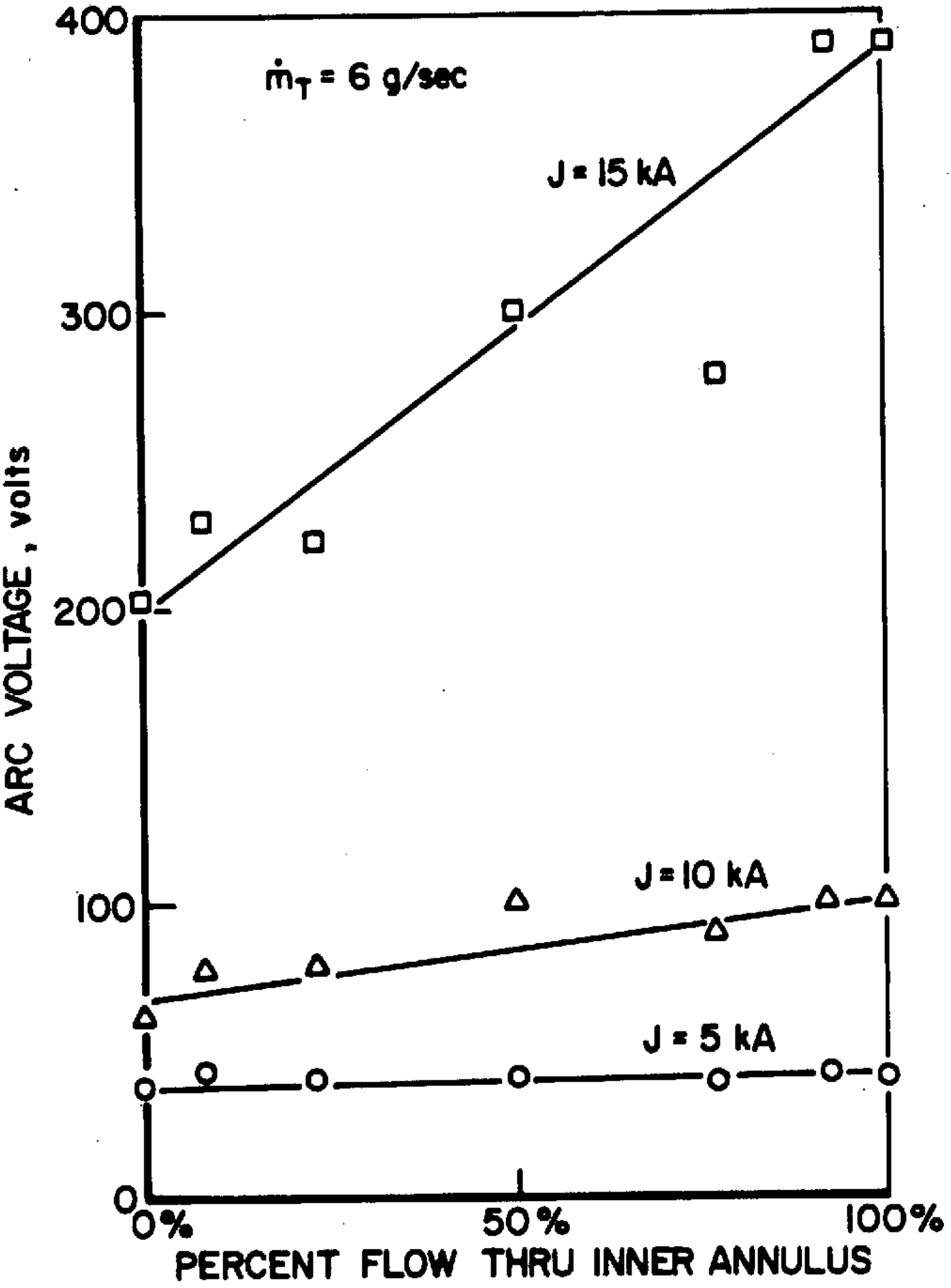

ARC VOLTAGE vs PERCENT FLOW THROUGH INNER ANNULUS

FIGURE 3-9
AP25-4970

exhaust velocity associated with 0% inner; 100% outer flow division operation. To determine this minimum voltage point of operation it is necessary to obtain the exhaust velocity's dependence on the % flow division. This relationship is presented in Figure 3-10 where the velocities are measured on the accelerator's centerline 2.5 cm downstream of the anode face. A critical mass flow rate through the inner annulus, $\dot{m}_c$, between 1.4 g/sec and 3.0 g/sec, exists such that for $\dot{m}$ (inner annulus) $>$ $\dot{m}_c$ the exhaust velocity is relatively constant about the argon velocity, while for $\dot{m}$ (inner annulus) $< m_c$ the exhaust velocity jumps to the neighborhood of the "boron nitride" plasma velocity calculated from the boron nitride version of Equation 3-d. Comparison of the voltage and velocity results implies that high current arcjet operation in the electromagnetic mode without insulator ablation effects at a minimum terminal voltage is achieved for this geometry with a 50:50 flow division. This mass injection geometry in conjunction with boron nitride insulation henceforth becomes the standard configuration in which the accelerator is operated.

III-6 Effects of Cathode Surface Area on the Terminal Voltage

Even with refractory insulating materials and an appropriate mass injection geometry, the previously described arcjet configuration exhibits a limited range of operation over which the arc voltage is essentially constant and steady for the duration of the current pulse. For a given mass flow rate, as the arc current is increased, a particular current, J^*, is reached beyond which the terminal arc voltage signal becomes unsteady. The onset of this voltage fluctuation with increasing arc current is illustrated in Figure 3-11 for a mass flow rate of 6 g/sec. J^* in this case is approximately equal to 12 kA while the characteristic frequency of the fluctuation is of the order of several hundred kilocycles. For mass flow rates other than 6 g/sec, the fluctuation occurs for arc currents such that the parameter $(J^*)^2/\dot{m}$, the arc current

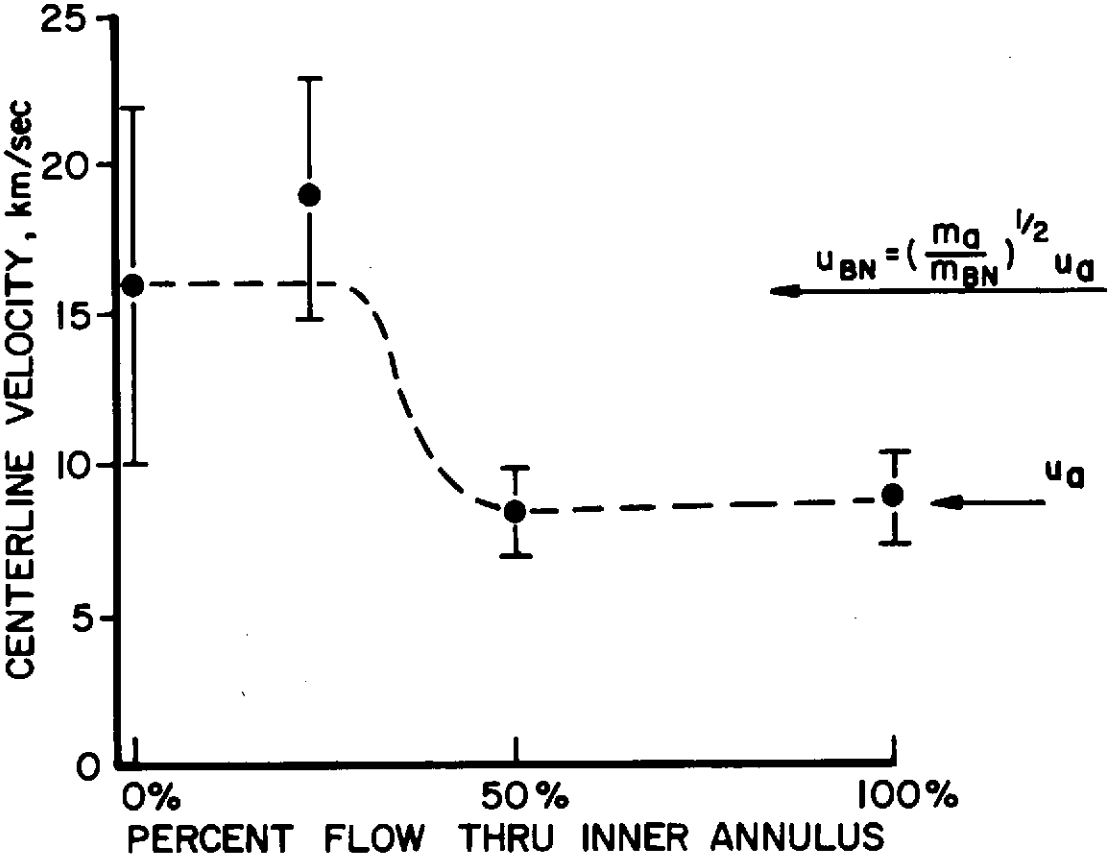

CENTERLINE VELOCITY vs FLOW DIVISION, J = 15.3 kA, $\dot{m}_T$=6g/sec

FIGURE 3-10
AP25·4971

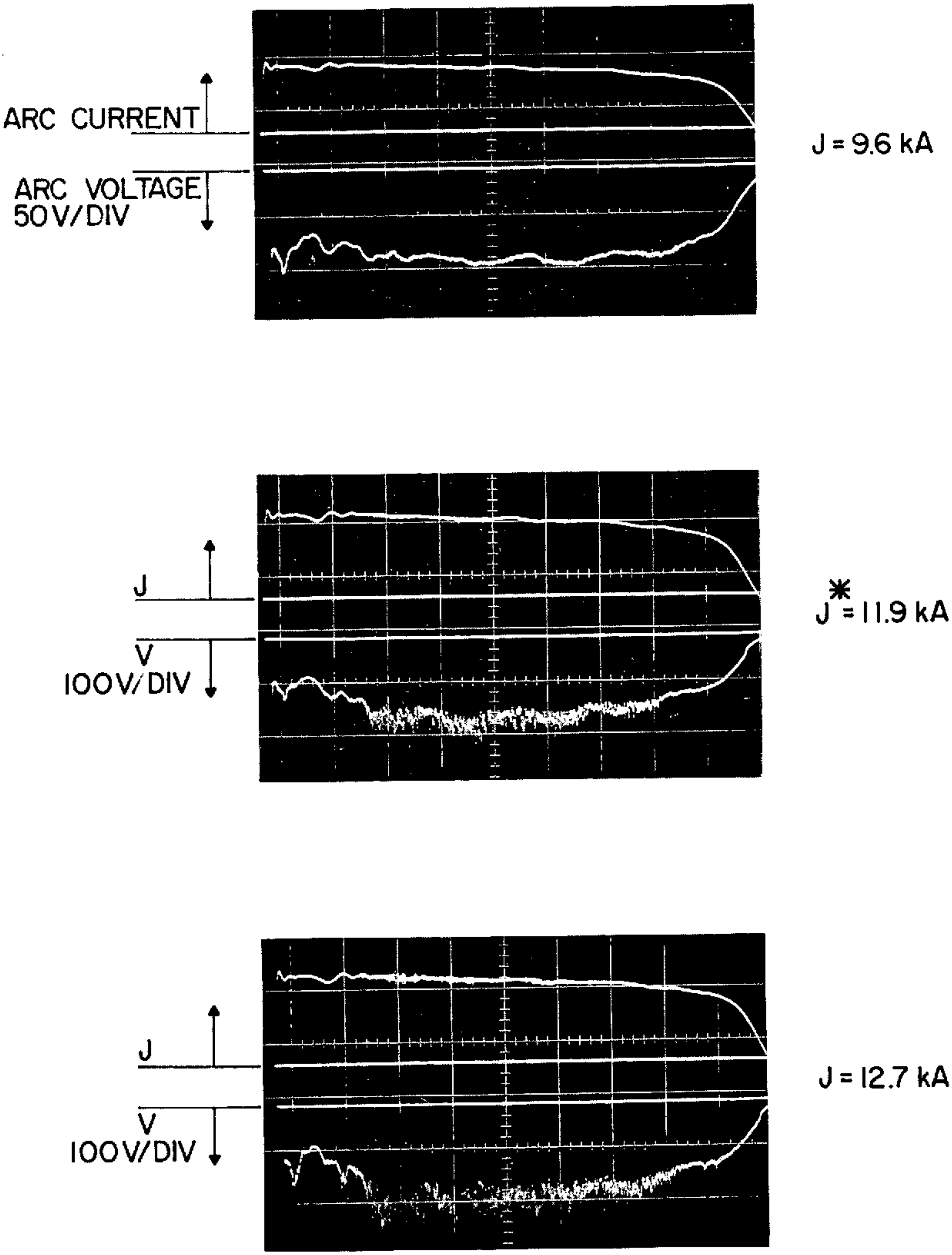

TERMINAL VOLTAGE FLUCTUATIONS

$\dot{m}$ = 6 g/sec, 50:50 FLOW DIVISION, CATHODE I

FIGURE 3-11

AP25-P-435

squared divided by the mass flow rate, is constant. This discharge phenomenon has only been observed for those quasi-steady arcjet configurations whose terminal voltages are not "ablation-dominated" because of their insulators.

The onset of such voltage fluctuations has been previously reported as indicative of the fundamental limitation of the quasi-steady MPD arcjet and has been used to define empirically a limiting value of the parameter $J^2/\dot{m}$ (Section I-3-4). In this manner Malliaris experimentally observed and analytically supported a critical $J^2/\dot{m}$ equal to 40 kA^2-sec/g for argon. However, for the case mentioned above, $(J^*)^2/\dot{m}$ equals 24 kA^2-sec/g. The AVCO and Princeton accelerators are similar in every detail except for their cathode geometries and thus their cathode surface areas. That the onset of a voltage fluctuation and hence the disparity between the critical $J^2/\dot{m}$ values might be associated with cathode phenomena is also suggested by spectral filter photographs of the cathode shown in Figure 3-12 which reveal different surface luminosity patterns for arc currents greater or less than J^*. Hence, the possibility arises that the onset of erratic arcjet voltage behavior is not indicative of a fundamental performance limitation imposed on the plasma flow, but rather a manifestation of electrode processes occurring in the vicinity of the cathode.

In order to investigate the relationship between erratic, non-steady arcjet behavior and cathode surface area, the accelerator was operated with several different cathode geometries for a given mass flow rate and mass injection geometry. The cathode geometries and their respective surface areas are illustrated and tabulated in Figure 3-13 and Table I. (For notational convenience, x_c for cathode 7 represents only the total cathode length. The length of the conical section for this cathode is 2.54 cm.) In all cases 6 g/sec argon is injected into the discharge chamber, with the inlet flow equally divided among twelve

FIGURE 3-12
AP 25-P-503

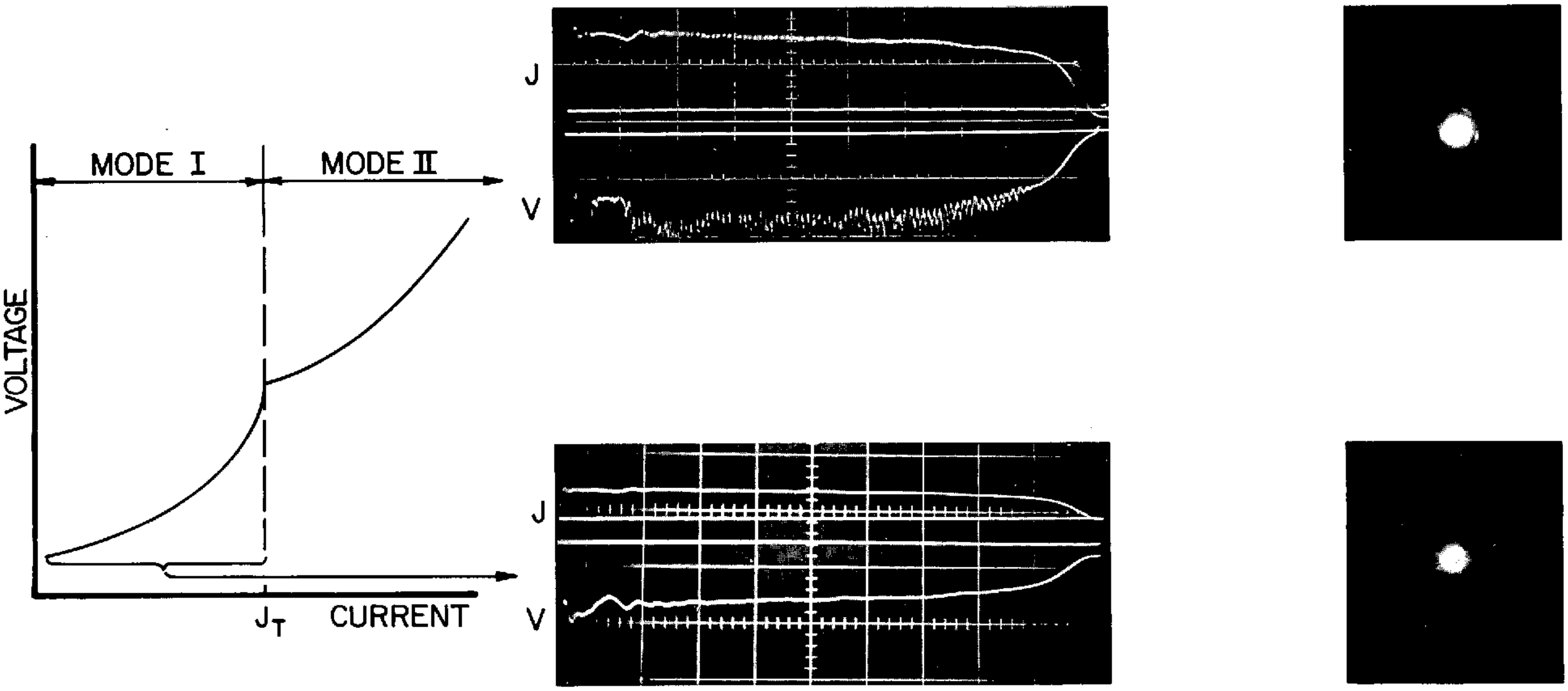

a) TYPICAL V-J CHARACTERISTIC

b) VOLTAGE SIGNATURE

PECTRAL PHOTOS
F CATHODE
5910 Å

DISCHARGE MODE CHARACTERISTIC

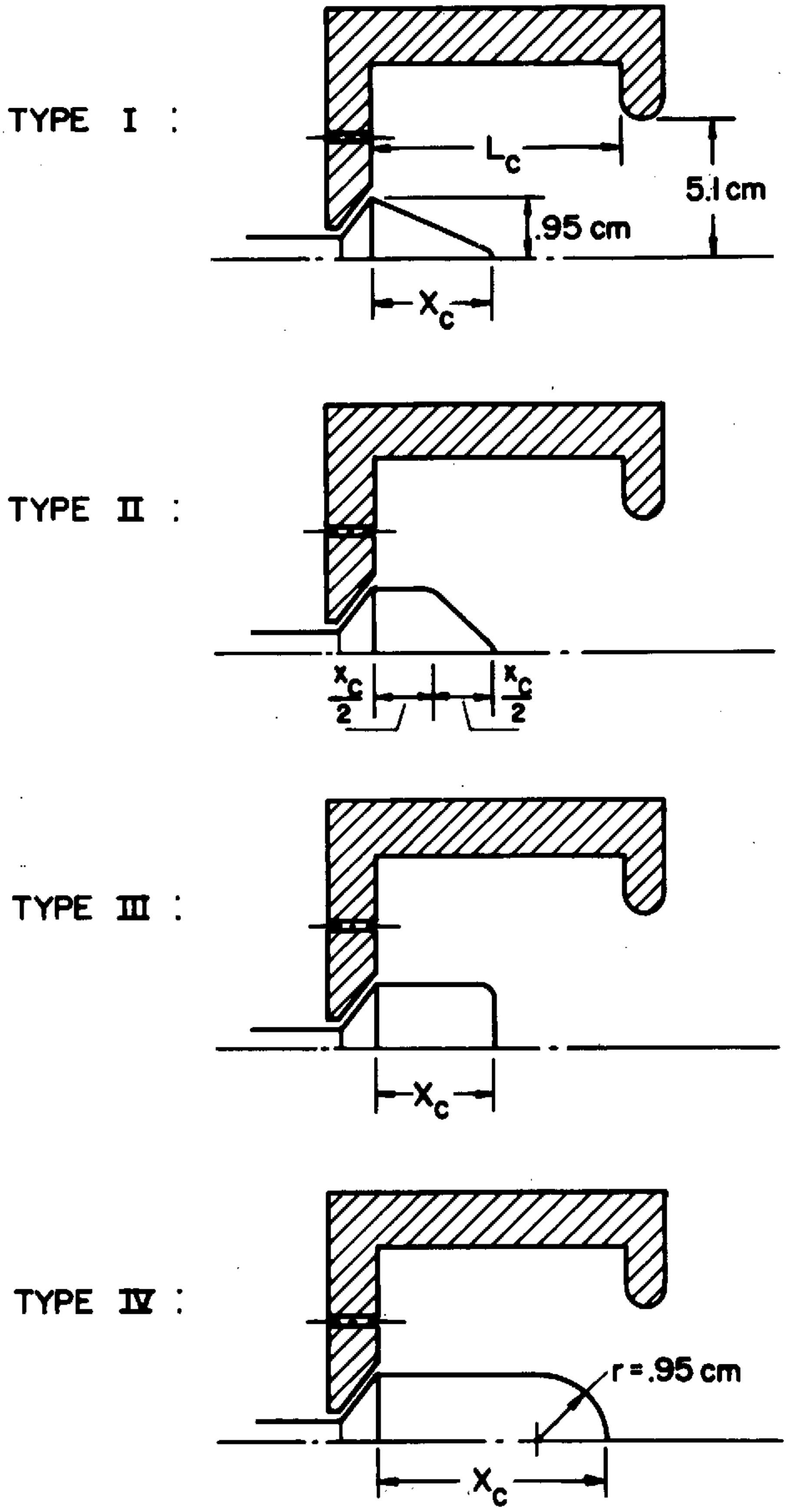

CATHODE GEOMETRIES

FIGURE 3-13
AP25.4999

0.318-cm-dia outer holes symmetrically distributed around the 3.81-cm radius, and the other half injected through an inner annulus about the base of the cathode (referred to as 50:50 flow division). In addition, the same maximum cathode diameter was maintained for all cathode geometries so as to minimize the number of variable cathode dimensions. Because of this constraint, accelerator configurations which employed cathodes whose surface areas were greater than 20 cm^2 necessitated varying the mean anode to cathode space, $L_c - X_c$. However, the dependence of the voltage fluctuation onset current, J^*, upon this distance, or alternatively on the chamber depth for a given cathode as shown in Figure 3-14, was found to be rather weak. Hence, the J^* - cathode area data are presented for accelerator configurations with a common chamber depth of 5 cm.

Table I

Cathode No.	Geometry		Surface Area, cm^2
1	Type I	x_c = 2.54 cm	10.23
2	Type II	x_c = 2.54 cm	13.66
3	Type III	x_c = 2.54 cm	19.35
4	Type II	x_c = 5.08 cm	25.97
5	Type IV	x_c = 5.08 cm	31.70
6	Type III	x_c = 5.08 cm	34.60
7	Type II	x_c = 7.62 cm	41.27

The current range over which the arc voltage becomes unstable is presented as a function of cathode surface area in Figure 3-15. The current associated with the onset of the fluctuation, J^*, scales directly with the cathode area and monotonically increases. Recent experiments with extremely long cathodes ($15 < x_c < 25$ cm) made of stainless steel suggest J^* continues to increase for even larger cathodes but at an ever decreasing rate. J^* appears to approach an upper limit of 25 kA.(41)

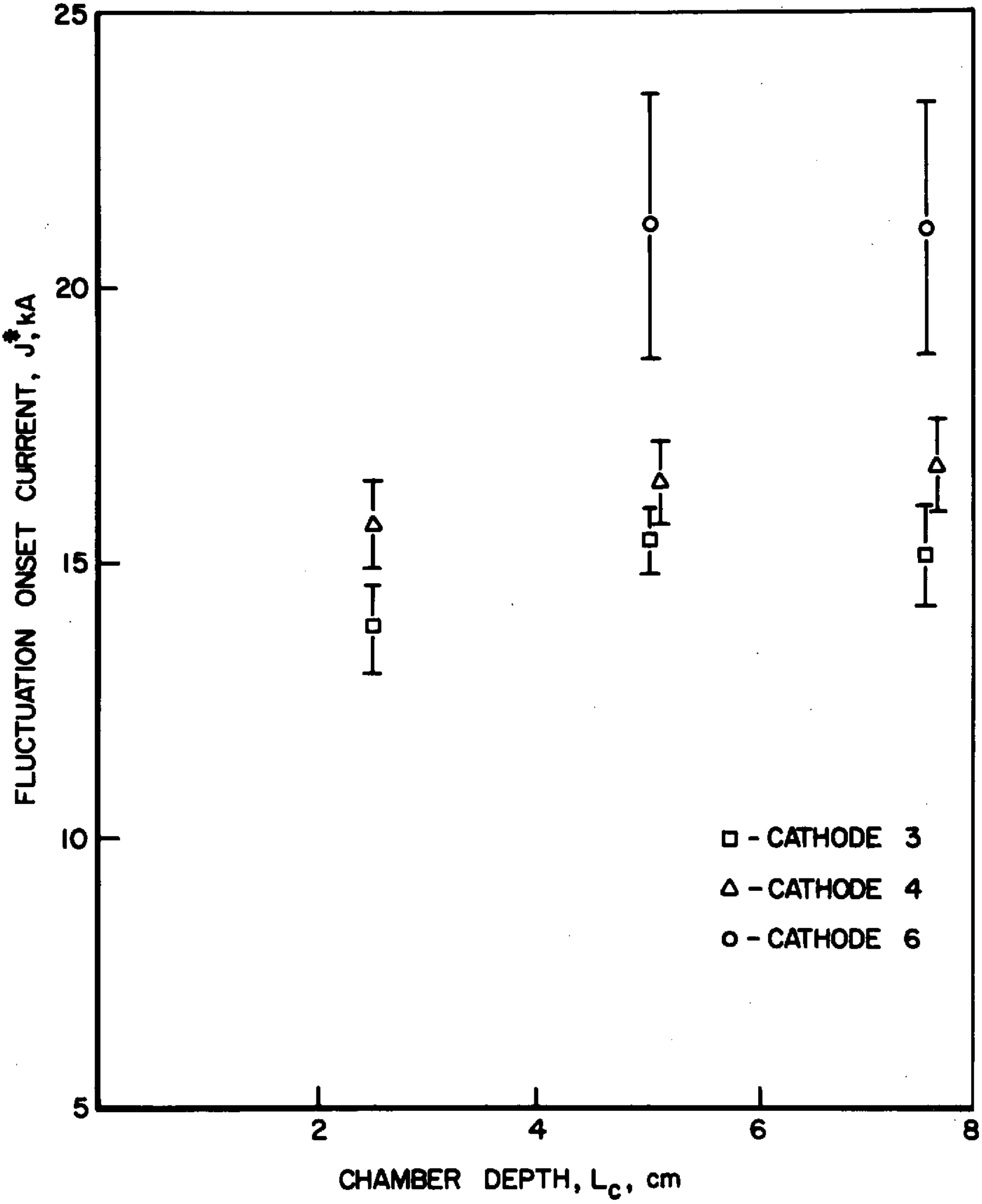

FLUCTUATION ONSET CURRENT vs CHAMBER DEPTH

$\dot{m}$ = 6 g/sec, 50:50 FLOW DIVISION

FIGURE 3-14

AP 25-5000

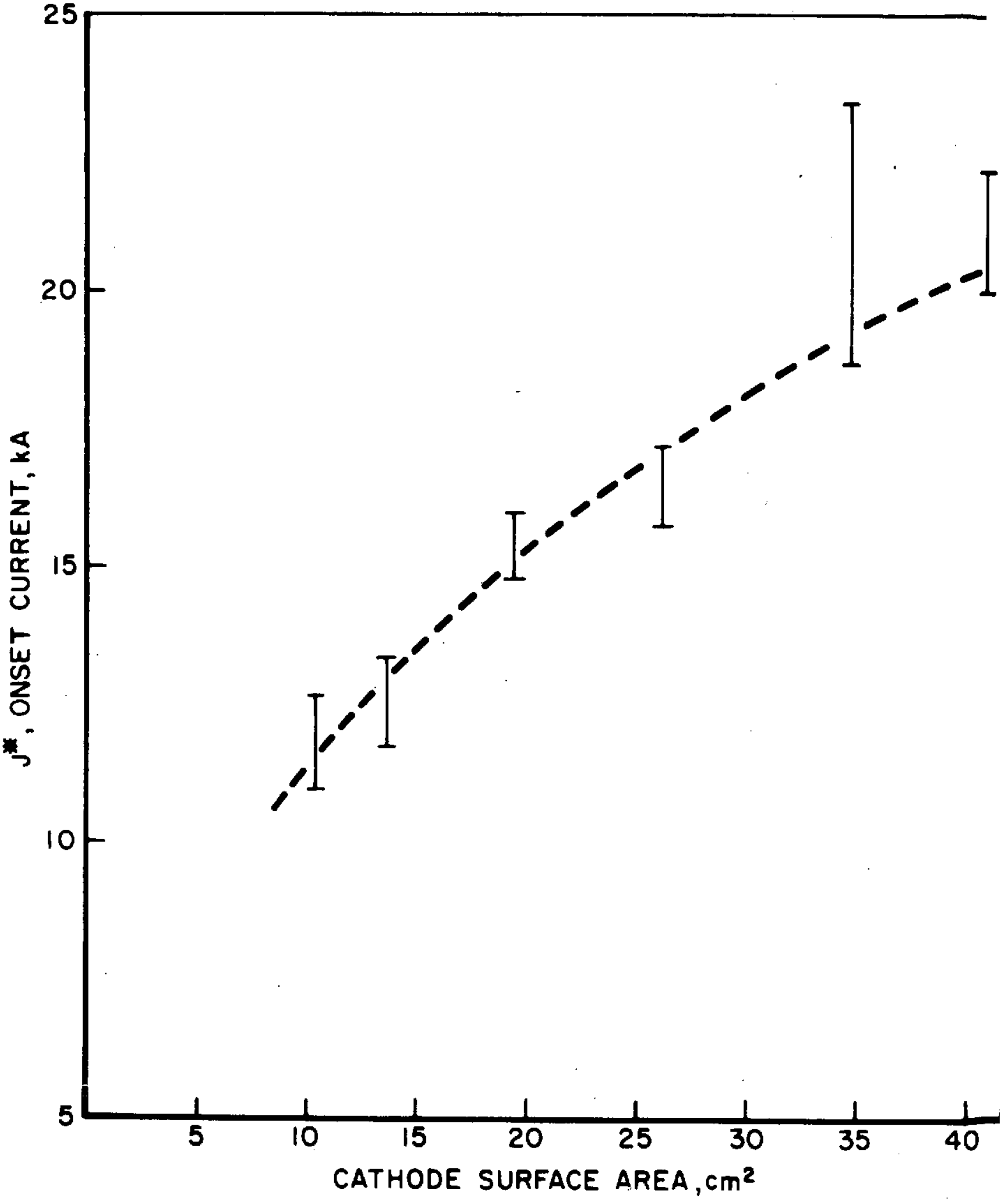

ONSET OF TERMINAL VOLTAGE FLUCTUATION

FIGURE 3-15
AP25·5001

Regardless of the exact functional form of J*, it is immediately evident that the terminal voltage instability phenomenon does not define a unique value of the $J^2/\dot{m}$ parameter as previously suggested.

Potential probes located arbitrarily close to the anode and cathode demonstrate the fluctuations in the terminal voltage signal are localized about the vicinity of the cathode. The potential drop between the cathode and a potential probe several millimeters off the cathode surface is measured differentially and labelled V_C. The floating potential several millimeters off the anode lip is simultaneously measured with respect to the anode ground and is labelled V_A. Figure 3-16 compares the oscillogram signatures of the terminal voltage, V_A and V_C for an arc current greater than J*. The cathode voltage signal clearly reproduces the onset time, frequency and amplitude of the terminal voltage fluctuation.

The onset of terminal voltage fluctuations is further characterized by a sudden increase in the local electric field about the cathode. Figure 3-17 presents V_C, V_A and the terminal voltage V as a function of current for a cathode 7, 50:50 flow division, 6 g/sec arc configuration. The current at which the cathode voltage sharply increases corresponds exactly with J^* determined from the terminal voltage-current characteristic. The anode voltage V_A also exhibits a similar sharp increase in magnitude although at a lower current of 8 kA. This value approximately equals the ion current which would be generated by the complete single ionization of the outer 3 g/sec argon mass flow rate.

It is interesting to note that the terminal voltages at which the sudden increase in cathode potential and discharge instability occur are insensitive to the cathode surface area. Preliminary stainless steel large cathode results suggest V^*

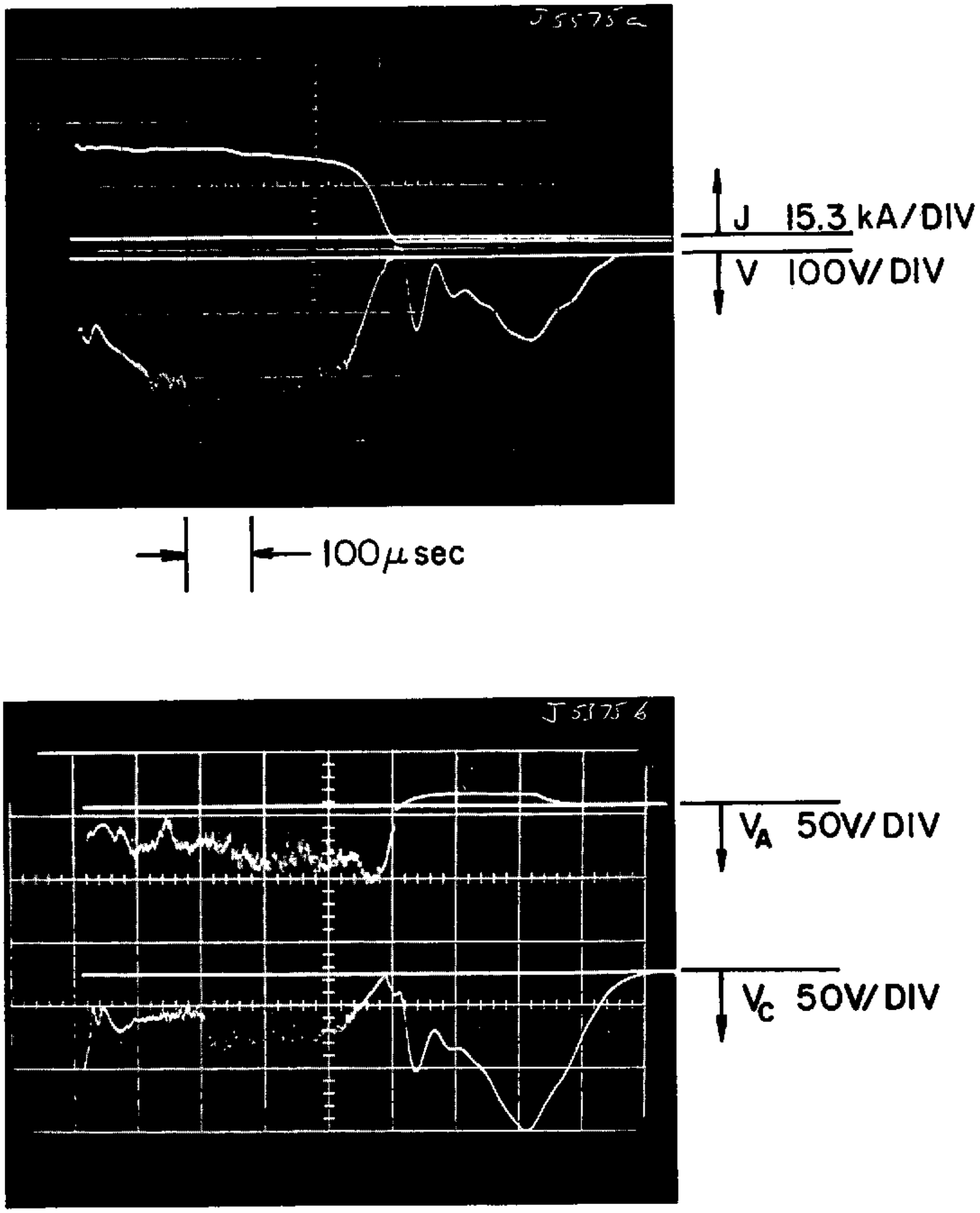

TERMINAL VOLTAGE AND FLOATING POTENTIAL SIGNATURES

FIGURE 3-16
AP 25-P-525

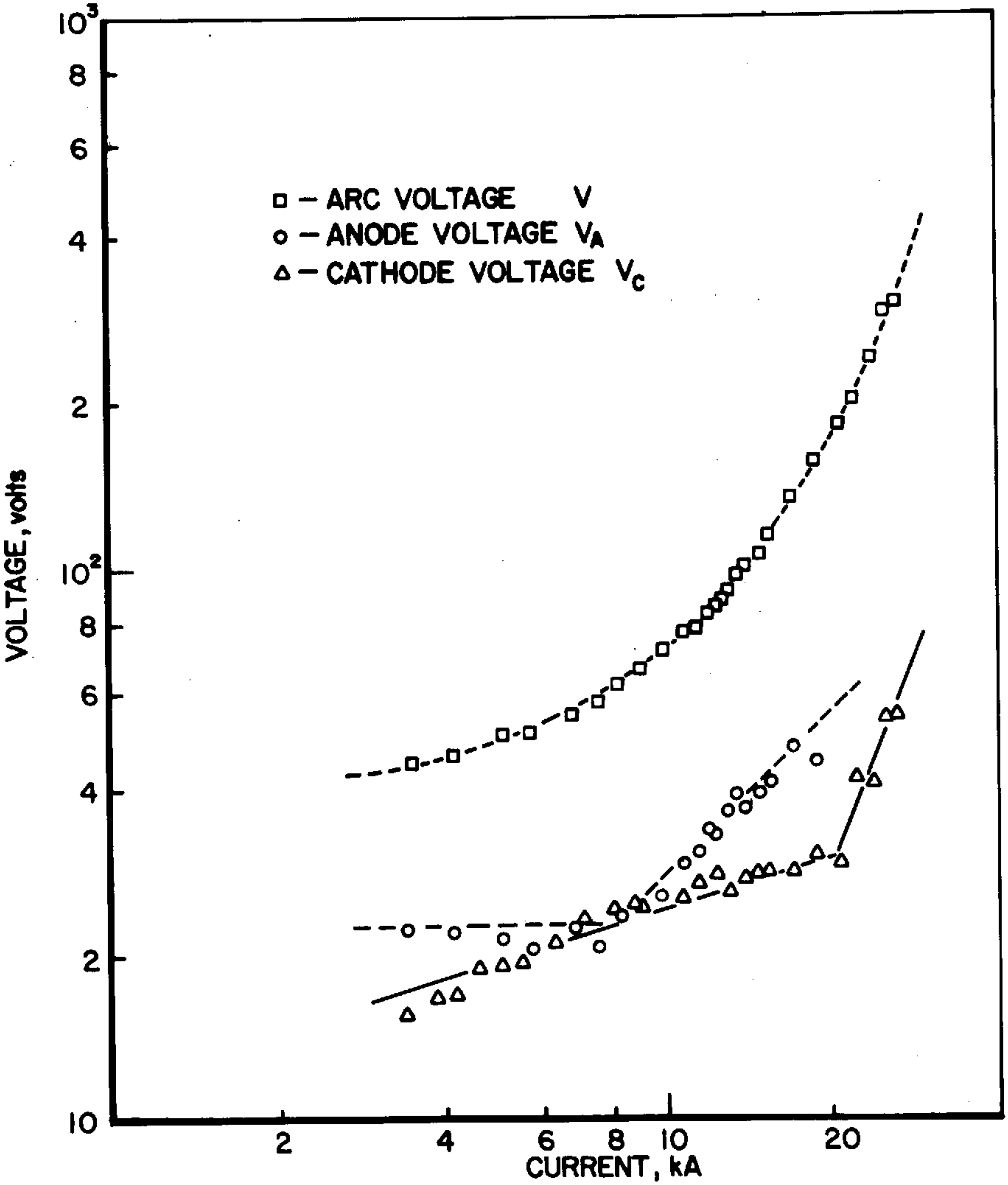

ANODE AND CATHODE VOLTAGE–CURRENT CHARACTERISTICS

FIGURE 3-17
AP25-5046

is also insensitive to cathode material.(41) These critical voltages are presented as a function of cathode surface area in Figure 3-18. The common voltage associated with the onset of the voltage fluctuations is 180 volts ± 30%. Thus it would appear that for arc conditions such that the terminal voltage exceeds V^*, the local electric field about the cathode sharply increases and becomes oscillatory. It is tempting to speculate that this critical voltage and the changes in the field properties about the cathode reflect a change in the local current emission processes. However, since the electron emission and current conduction processes in the cathode region of an arc discharge are extremely complex and pertinent experimental data do not presently exist, further clarification of this suggestion must await future work.

In any case, one concludes that in order to conduct a given current without undue difficulty, the quasi-steady MPD arc requires a minimum cathode surface area for a given mass flow rate.

It should also be pointed out that as a consequence of increased cathode surface areas, terminal arc voltages for a given arc current and mass flow rate decrease in magnitude. All else remaining the same, this trend implies increased overall arcjet efficiencies. Arc voltages as a function of cathode area are given in Figure 3-19 for arc currents of 10, 15, and 20 kA. For each particular current the arc voltage approaches a lower limit as the cathode area is increased. Thus a minimum arc impedance associated with large cathode operation may be defined and is calculated to be approximately 6 milliohms for this configuration. This value is of the same order as the impedance corresponding to the limiting values of J^* and V^*; that is $V^*_{max}/J^*_{max} \simeq$ 180 volts/25 kA $\simeq$ 7 milliohms. This trend has been theoretically predicted for a parallel plate MPD discharge using a one-dimensional, scalar conductivity model of the discharge.(12)

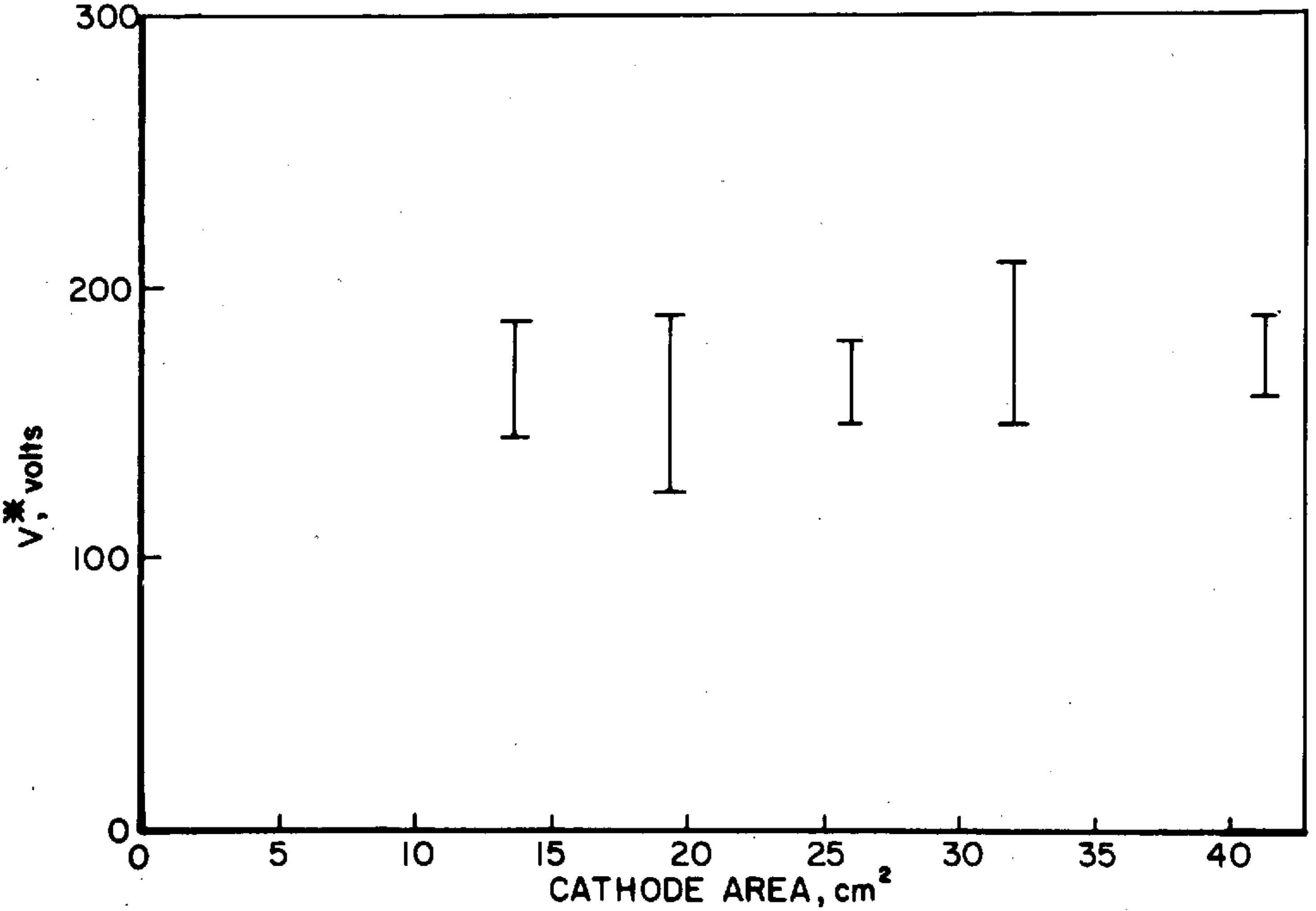

CRITICAL TERMINAL ARC VOLTAGES

FIGURE 3-18

AP 25·5047

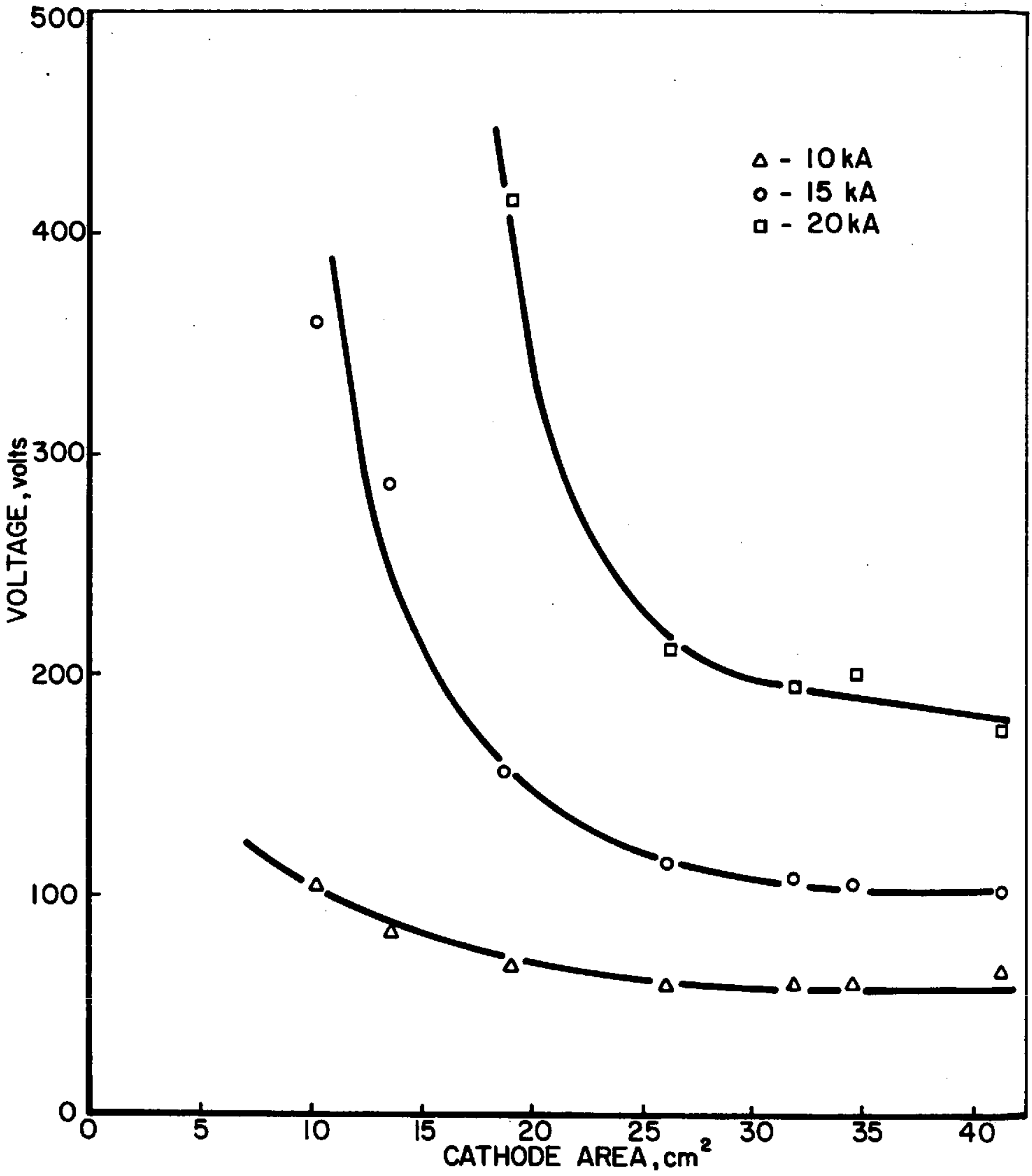

VOLTAGE - CATHODE AREA CHARACTERISTICS

FIGURE 3-19
AP 25-5048

III-6-1 Propellant Flow Division Revisited

One may now return to examine the effect that mass injection geometry has upon the steadiness and magnitude of the terminal voltage for given arc currents and cathode geometries in light of the previously discussed cathode area effect. Division of the 6 g/sec injected argon is varied between 100% inner: 0% outer flow and 0% inner: 100% outer flow for two cathode geometries. The V-J characteristics for each cathode geometry are measured as a function of flow division. Two effects are noted. The functional dependence of the onset current J^* is dependent upon the relative area of the given cathode as shown in Figure 3-20. For the smaller cathodes typified by the cathode 1 data in Figure 3-20, J^* is insensitive to the manner in which the argon is distributed throughout the discharge chamber. The magnitude of J^* for all flow divisions is equal to 12 kA, the value associated with the area of cathode 1. However, in the case of larger cathodes represented by the cathode 5 data in Figure 3-20, J^* exhibits a nearly discontinuous dependence upon the flow division. When greater than 50% of the injected mass flow is delivered to the outer radial regions of the discharge chamber, the voltage goes unstable at a J^* associated with the surface area of cathode 5. The sudden drop to a lower instability onset current as less than 50% of the mass flow is injected towards the anode region suggests that a second instability phenomenon associated with anode starvation may be present. The sudden growth of fluctuating electric fields in the vicinity of the anode when insufficient charge carriers are delivered to that region is well documented.(28,40) This is further suggested in Figure 3-21 which presents the arc voltage as a function of flow division for cathode 5, total mass flow rate of 6 g/sec, and currents of 5, 10, and 15 kA. The sudden rise in the terminal voltage associated with outer mass flow rates of less than 3 g/sec in the 15 kA case may be tentatively identified as a manifestation of anode starvation.

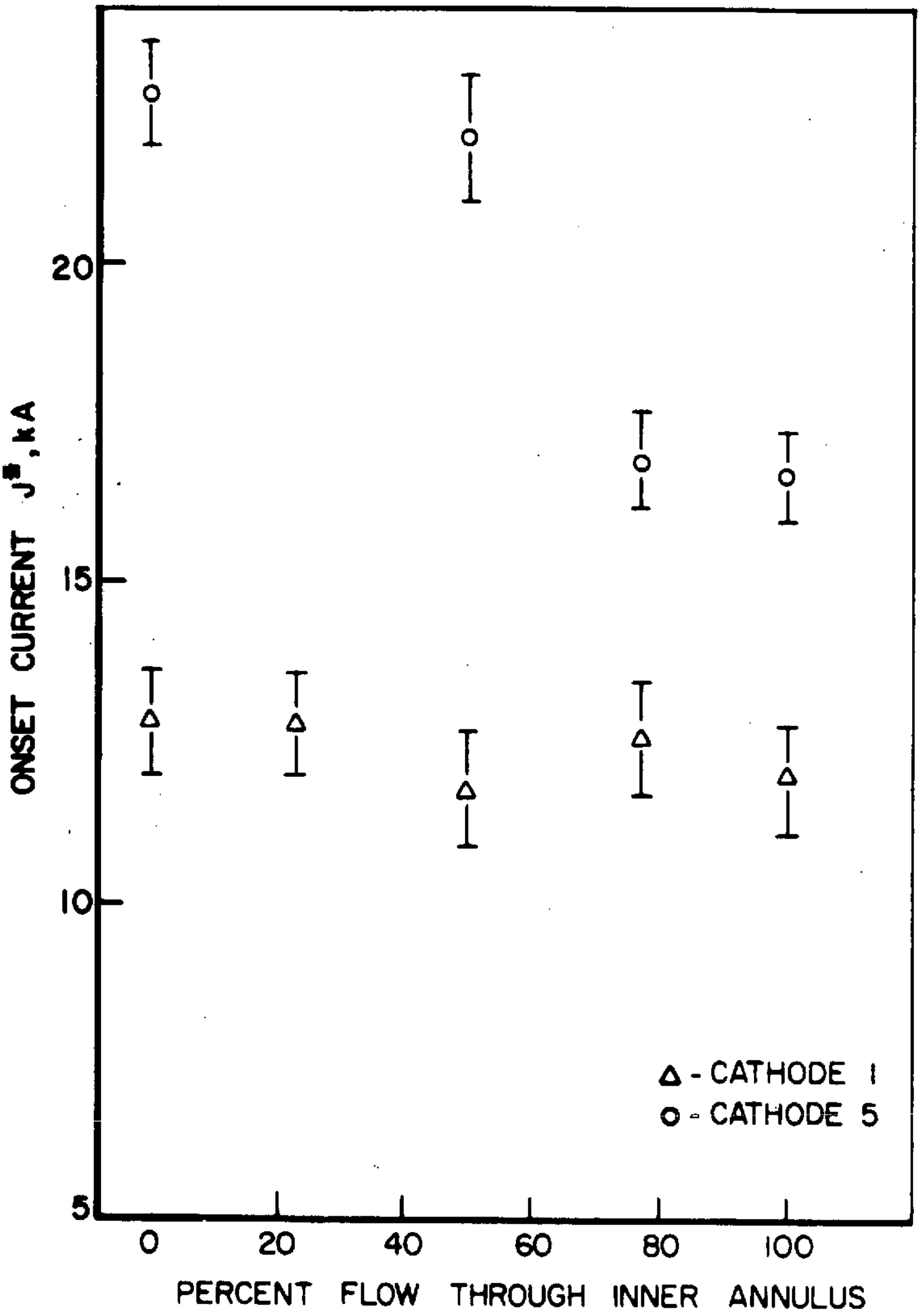

ONSET CURRENT vs FLOW DIVISION

$\dot{m} = 6$ g/sec

FIGURE 3-20
AP 25-5002

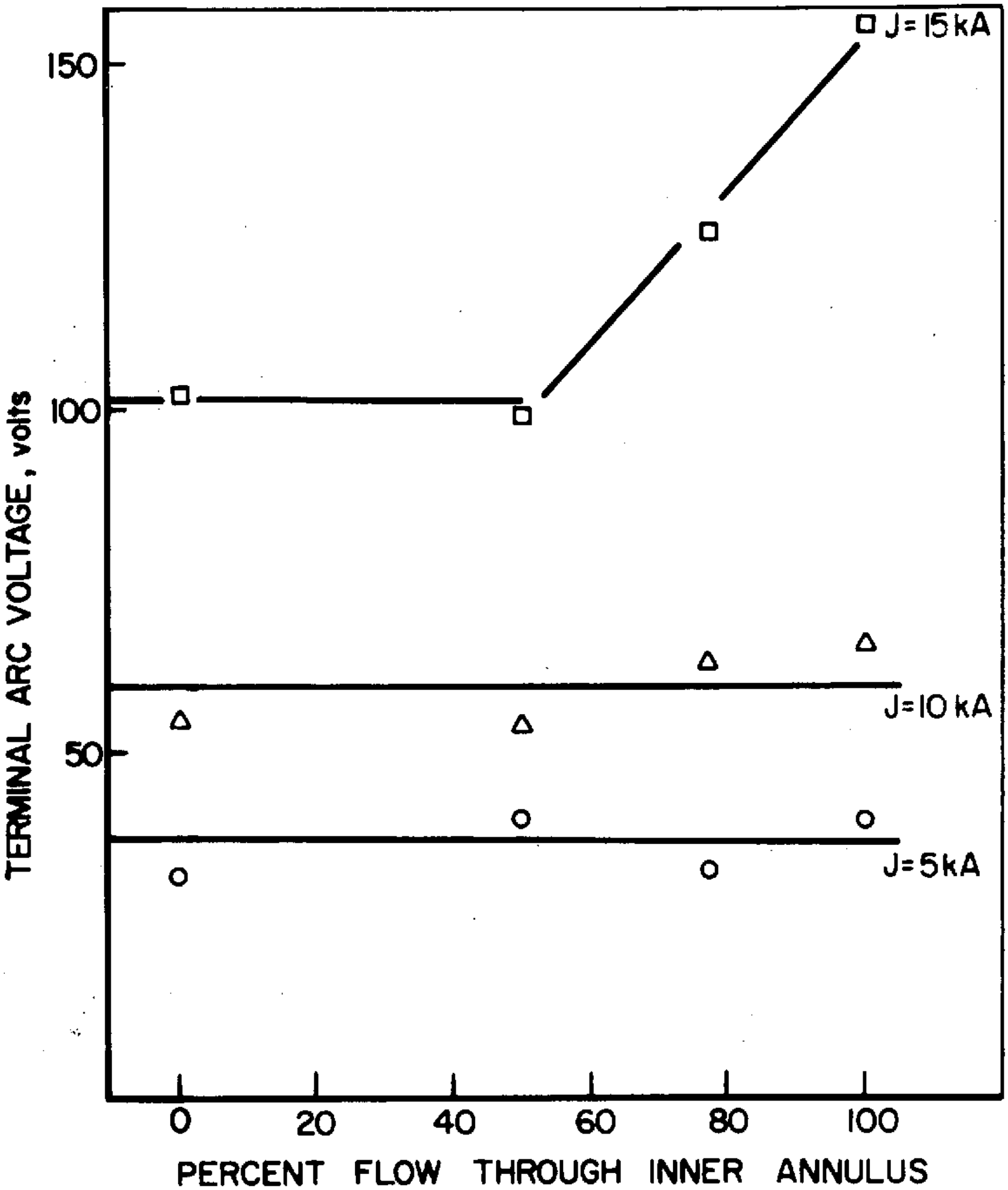

ARC VOLTAGE vs FLOW DIVISION

$\dot{m}$ = 6g/sec, CATHODE 5

FIGURE 3-21
AP25 · 5003

III-6-2 Insulator Ablation Revisited

Referring back to Figure 3-15 it would seem that quasi-steady operation free from spurious effects is attainable for increasing arc currents at a fixed mass flow rate by appropriately increasing the cathode surface area. However, ablation measurements of the arc discharge demonstrate that this is not the case. The discharge plasma has been viewed through a monochromator-photomultiplier optical arrangement selectively tuned to observe either the 4497 Å BIII and/or 4630 Å NII spectral lines. The absence or presence of spectral radiation from either ablated species is recorded as a function of arc current for various cathode geometries and a mass flow rate of 6 g/sec with 50:50 flow division. The current at which ablated species are initially detected in the discharge plasma is then plotted against the area of that configuration's cathode and is shown in Figure 3-22. Also included in Figure 3-22 is the voltage fluctuation onset current J^* previously shown in Figure 3-15.

Based on Figure 3-22, it now appears that even for a large enough cathode to avoid voltage fluctuations, an upper limit on arc current for quasi-steady operation is imposed by insulator ablation. For arcjet configurations with smaller cathodes, the onset of insulator ablation and terminal voltage fluctuations coincide. One may postulate that the local electric fields required to enhance the emission process due to the insufficient cathode area in turn increase the magnitude of the local Joule heat flux to the neighboring insulator surfaces thereby initiating insulator ablation. However, as is seen in the larger cathode cases, insulator ablation begins at a current lower than one would expect if the onset of ablation were solely associated with the cathode area phenomenon. In fact, the onset of insulator ablation appears to plateau at a current, J_A^*, of approximately 15.3 kA for an injected mass flow rate of 6 g/sec. Furthermore, for the same cathode area, argon mass flow rates and

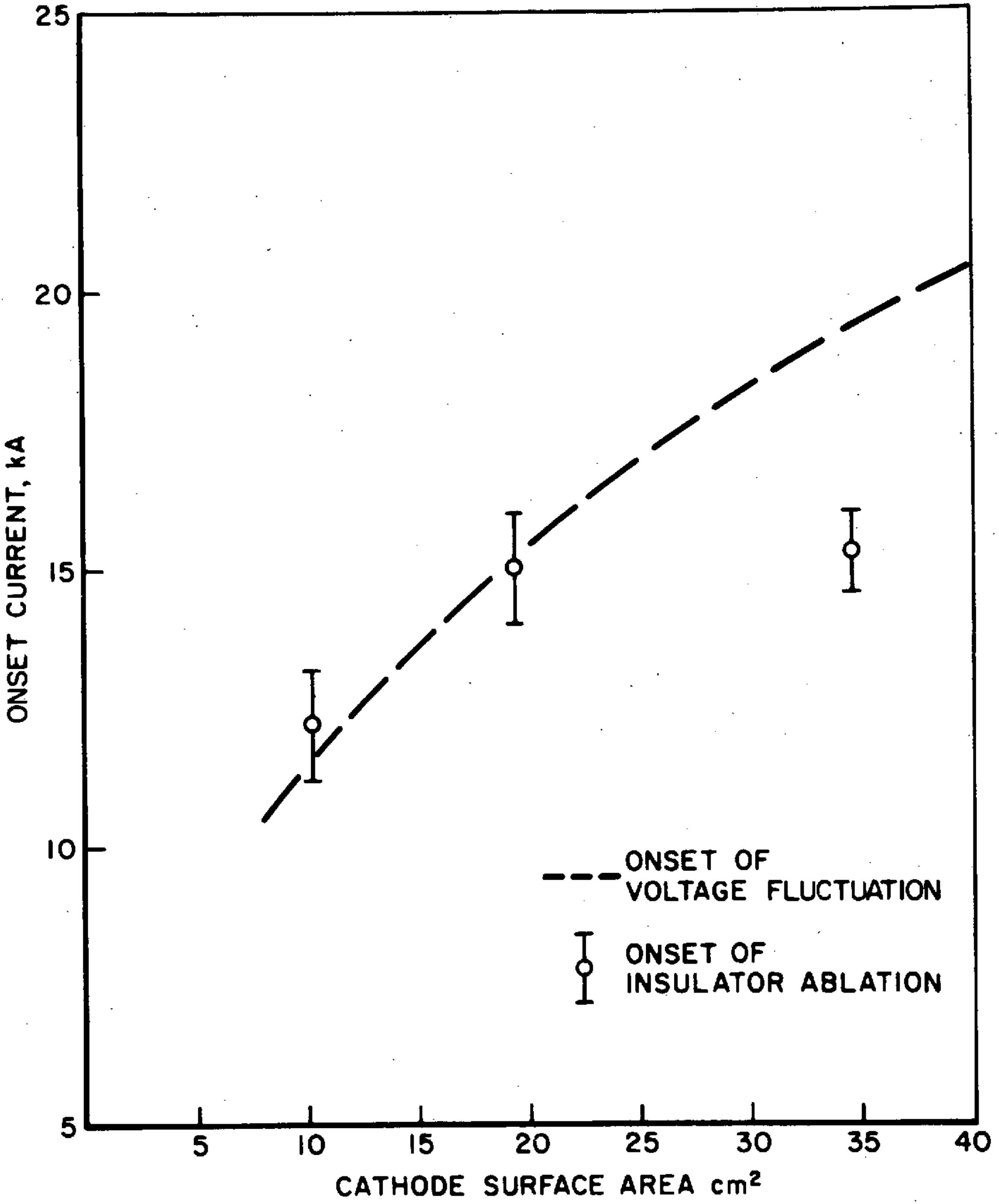

ONSET OF INSULATOR ABLATION

FIGURE 3- 22

AP25 · 5004

their respective ablation onset currents scale such that $(J_A^*)^2/\dot{m}$ is constant. This value of $(J_A^*)^2/\dot{m}$ equals 39 kA^2-sec/g.

The significance of this value depends upon the details of the boron nitride ablation process. Most likely, arc operation with large cathodes for 39 $kA^2\text{-sec/g} \leq J^2/\dot{m} \doteq (J^*)^2/\dot{m}$ is characterized by local electric field and current density distributions such that the Joule energy transfer to the insulating boron nitride is sufficient to raise the surface temperature to its ablation limit. In this case insulator ablation would be a normal consequence of arcjet operation with that particular insulator. Non-ablating arcjet operation between 39 $kA^2\text{-sec/g} \leq J^2/\dot{m} \doteq (J^*)^2/\dot{m}$ would therefore simply require substitution of a more refractory-insulating material. Since arcjet operation in this range is not required for this study, further investigation of these points was not warranted and thus not pursued.

III-7 Criteria for Nominal Quasi-steady MPD Arc Operation

It is now possible to list three criteria which must be satisfied in order to produce a quasi-steady MPD arc configuration whose characteristics are independent of the previously mentioned extraneous effects. I - use of refractory insulator materials in order to resist the onset of insulator ablation due to the thermal and radiative energy fluxes associated with high power quasi-steady operation. II - use of an appropriate mass injection geometry (in this case, 50:50 flow division) in order to (a) remove direct insulator-cathode contact in regions of intense Joule heating, (b) provide propellant directly to the most vigorous acceleration zones of the discharge, and (c) provide sufficient charge carriers in the vicinity of the anode to conduct the total current. III - use of a cathode of sufficient surface area to allow the required cathode surface emission without inducing intense electric field oscillations.

These results are summarized in Figure 3-23 in which several regimes are delineated in the current-cathode area plane. Only within the region labelled "nominal arc-jet operation" does the accelerator function independently of insulator material and free from terminal voltage fluctuations. This region is bounded on the left by the ablation and fluctuation onset curves, and above by only the insulator ablation curve. The following chapter discusses properties of the plasma acceleration process for an MPD discharge characterized by the starred point within this region.

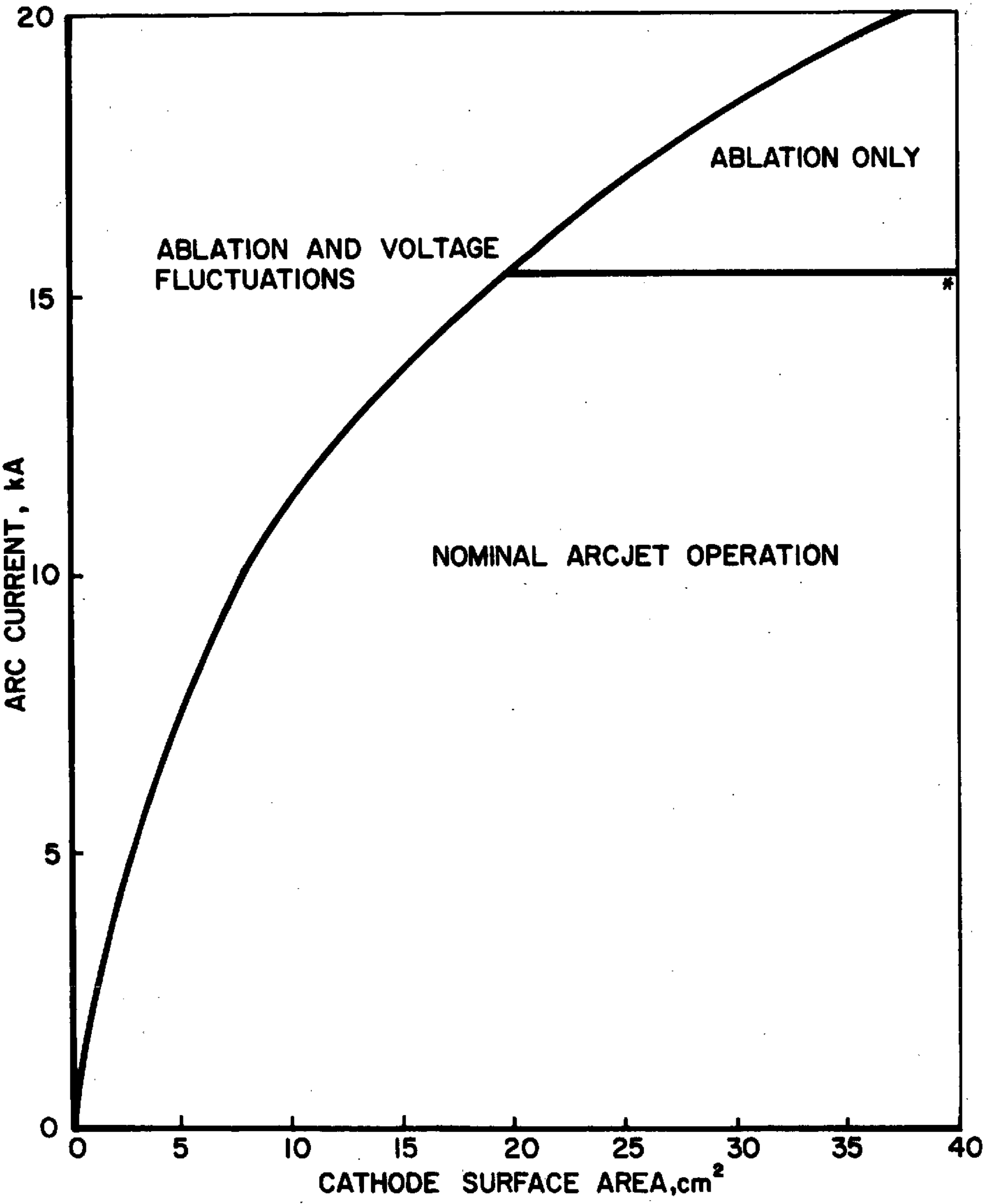

MPD OPERATIONAL REGIMES
$\dot{m}$ = 6 g/sec, 50:50 FLOW DIVISION

FIGURE 3-23
AP25-5049

Chapter IV

Quasi-steady Plasma Acceleration Processes

IV-1 Introduction

Understanding the plasma acceleration mechanisms within the quasi-steady MPD arcjet represents one of the first steps toward acquiring a fundamental comprehension of the thruster's capabilities. The exact nature of the plasma acceleration process in quasi-steady MPD arcjets has remained elusive, although several semi-empirical models have been proposed. Against this background of theoretical uncertainty and incomplete experimental evidence, claims that quasi-steady electromagnetic accelerators are fundamentally limited in attainable exhaust velocities appear to be somewhat premature. However, it would be inappropriate to dismiss such claims lightly, since the MPD arcjet's ultimate applicability as a space thruster will be defined in terms of its maximum performance capabilities. Further clarification of the plasma acceleration process is needed to define these capabilities.

For the purposes of this program, the local plasma acceleration processes will be examined in light of changes in the local velocity vector through the MPD arc discharge. In principle, the total velocity vector field of the accelerator may be determined by the simultaneous solution of the mass, momentum and energy conservation equations for given initial and boundary conditions. The electromagnetic variables responsible for the Lorentz body force in the momentum equation and the Joule heating term and the energy equation must be consistent with Maxwell's equations. In addition, a generalized Ohm's law which describes the coupling between the electromagnetic and gasdynamic variables must be prescribed. An appropriate equation of state and expressions for the plasma transport properties including a plasma conductivity law are required to complete the set. In practice the coupled nonlinear nature of the governing partial differential equations presents a problem of extreme mathematical complexity.

In contrast, the quasi-steady plasma acceleration problem becomes more tractable when discussed in a semi-empirical manner. This chapter presents the measured exhaust velocity profile for an accelerator operating at an arc current of 15.3 kA and an argon mass flowrate of 6 g/sec. The electromagnetic discharge structure responsible for the plasma acceleration is also presented. These data are combined in a quasi-phenomenological model of the acceleration process and finally discussed in light of the claim that quasi-steady accelerators are fundamentally limited.

IV-2 Experimental Conditions

The plasma acceleration process may be studied for any desired combination of arcjet parameters so long as the overall accelerator configuration lies within the "nominal" regime of Figure 3-22. There is particular interest, however, in examining the exhaust velocity profile of the quasi-steady accelerator for operating conditions such that the parameter $J^2/\dot{m}$, the arc current squared divided by the argon propellant mass flow rate, approximately equals 40 kA^2-sec/g. Claims have been made previously that the acceleration mechanisms are fundamentally limited at these conditions (Section I-3-4). Furthermore, the results of Chapter III indicate that arcjet operation free from (boron nitride insulator) ablation is restricted to $J^2/\dot{m}$ less than or equal to 40 kA^2-sec/g.

For this study, this condition is realized experimentally with an arc current of 15.3 kA and a total argon mass flow rate of 6 g/sec. The mass injection configuration equally divides the total propellant flow between inner and outer injection orifices. Three grams per second are injected directly about the cathode through an inner cathode base annulus.

The remaining 3 g/sec enter the discharge chamber through twelve 0.32 cm holes symmetrically distributed about the 3.81 cm radius.

Referring to Figure 3-22, a cathode area greater than 20 cm^2 is required for this combination of arc current and mass flow. A thoriated-tungsten type II cathode 1.91 cm in diameter, 7.62 cm in length, with a 2.54 cm conical tip provides sufficient electrode area ($\sim$41 cm^2) to insure stable arcjet operation.

This arcjet configuration satisfies the three criteria for nominal MPD arcjet operation discussed in Chapter III. This insures that experimental arc voltages and exhaust velocities are unperturbed by extraneous effects. The terminal arc voltage for this configuration equals 115 volts. Typical current and voltage signatures at these conditions are shown in Figure 4-1. The exhaust velocity profile is discussed below.

IV-3 Axial Velocity Profile

The axial velocity profile measured using the time-of-flight probe technique on the accelerator's centerline is presented in Figure 4-2. The axial distance z is measured downstream from the anode plane. Velocity measurements within the discharge chamber were precluded due to the lack of discernable ion density fluctuations required by the time-of-flight technique. The plasma leaves the discharge chamber at a velocity less than 9.0 km/sec. Final exhaust velocities of 12.5 km/sec are observed several anode orifice diameters downstream. This final exhaust velocity exceeds by nearly 50% the Alfven critical speed of 8.7 km/sec for argon, previously suggested as the upper limit to which propellant may be accelerated by a quasi-steady MPD arc operating at these conditions.

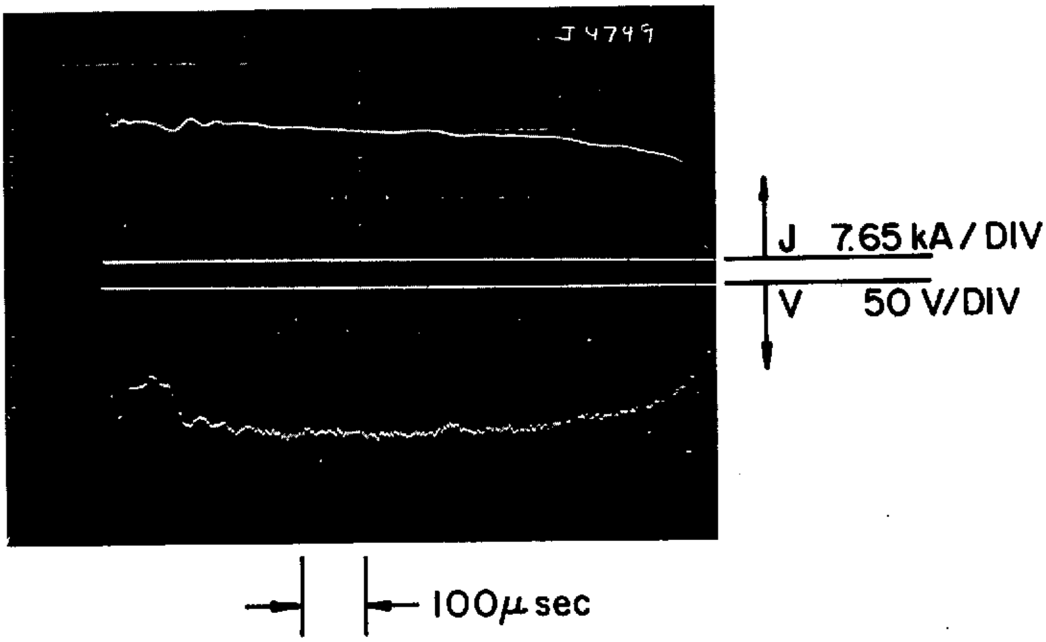

ARC CURRENT AND VOLTAGE SIGNATURES

FIGURE 4-1
AP25-P-526

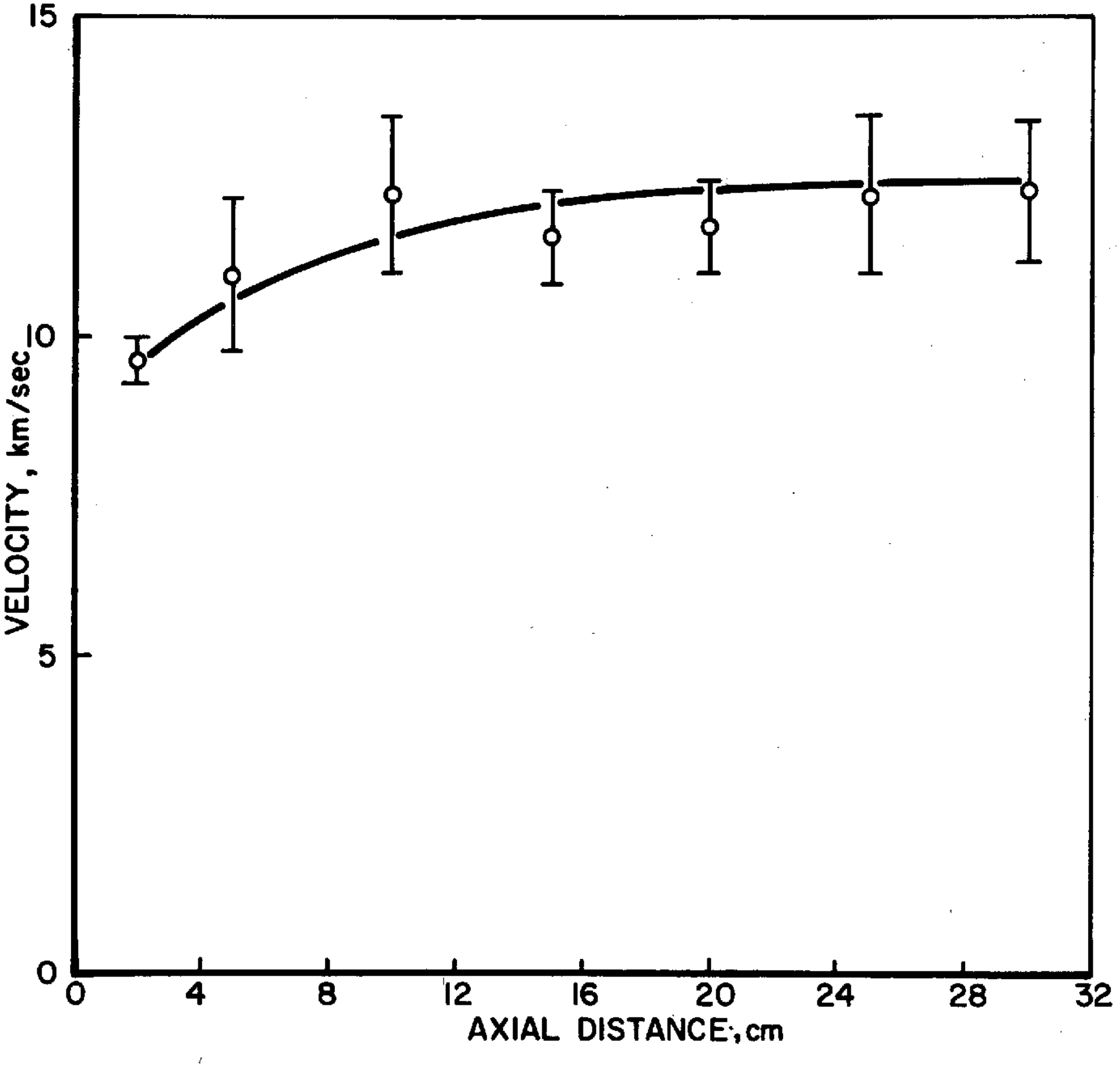

CENTERLINE AXIAL VELOCITY PROFILE

FIGURE 4-2

AP25-5050

IV-4 Electromagnetic Structure of the MPD Discharge

The exhaust velocity profile results primarily from the combined action of electromagnetic body forces upon the accelerated propellant mass. The magnitude and direction of the electromagnetic body forces may be ascertained from measured distributions of current density and magnetic field. In this way the local acceleration processes may be related to the local $\bar{j} \times \bar{B}$ distribution. Alternatively, the plasma acceleration process may be viewed as the conversion of some portion of the electrical input power $(\bar{j} \cdot \bar{E})$ into directed motion of the propellant. Evaluation of the local $\bar{j} \cdot \bar{E}$ power deposition within the arc discharge requires knowledge of the electric fields as well as the current density distribution. From these distributions of magnetic field, current density and electric field, a qualitative model of the quasi-steady acceleration mechanisms will emerge.

IV-4-1 Magnetic Field Distribution

Because the arc discharge is cylindrically symmetric, the induced self magnetic field (B) is azimuthal. The B field distribution is determined from axial and radial induction coil surveys. Azimuthal probe surveys for selected radial locations within the discharge confirm the presumed cylindrical symmetry of the magnetic field. The magnetic field distribution stabilizes in two characteristic times. Approximately 200 μsec after discharge initiation, the magnetic field within the discharge chamber assumes a quasi-steady distribution. At a somewhat later time, approximately 450 μsec into the 1000 μsec current pulse, a quasi-steady distribution throughout the entire flow field is achieved. This quasi-steady distribution, presented in Figure 4-3, is maintained for the duration of the current pulse. In this figure, lines of constant magnetic induction are superimposed upon a schematic of the accelerator chamber.

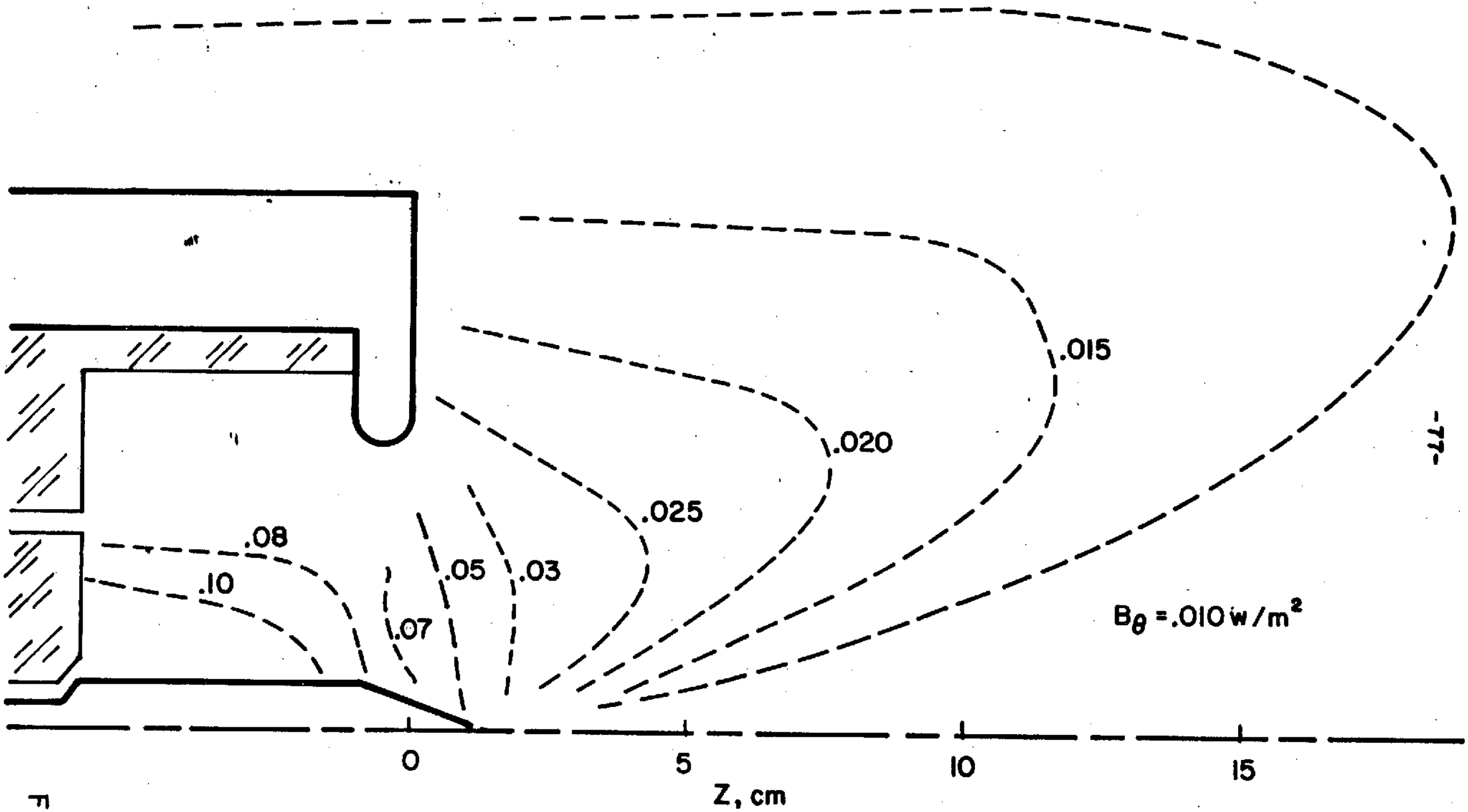

FIGURE 4-3
AP25-5051

QUASI - STEADY MAGNETIC FIELD DISTRIBUTION

IV-4-2 Current Density Distribution

The quasi-steady current density pattern is derived directly from the magnetic field data. Employing Ampere's law and the azimuthal symmetry of the discharge, enclosed current contours may be constructed according to Equation 4-a.

$$J_{EN}(r,z) = \frac{2\pi r \ B(r,z)}{\mu_o} \tag{4-a}$$

An enclosed current contour is defined such that the specified current associated with a particular contour flows downstream of that contour. Each enclosed contour also represents a current streamline. The magnitude of the local current density vector may be estimated by dividing the current between two adjacent current contours by the normal area through which it flows. The direction of the current density vector corresponds directly to that of the local current streamline. The quasi-steady current distribution for the total discharge current of 15.3 kA is illustrated in Figure 4-4. Each current contour is labelled with the amount of current in kiloamperes which flows downstream of it.

A significant fraction of the total arc current flows in the region exterior to the discharge chamber. The current streamlines within the accelerator chamber emerge from the cathode with a density distribution peaked at both ends of the cathode as shown in Figure 4-5. The current contours then bend axially downstream before turning radially toward the anode. Anode current attachment concentrates about the lip region of the anode. Outside the discharge chamber nearly fifty percent of the total arc current billows far downstream in the exhaust plume before returning and attaching on the outer surfaces of the anode barrel. The current density vector within several centimeters of the accelerator's centerline

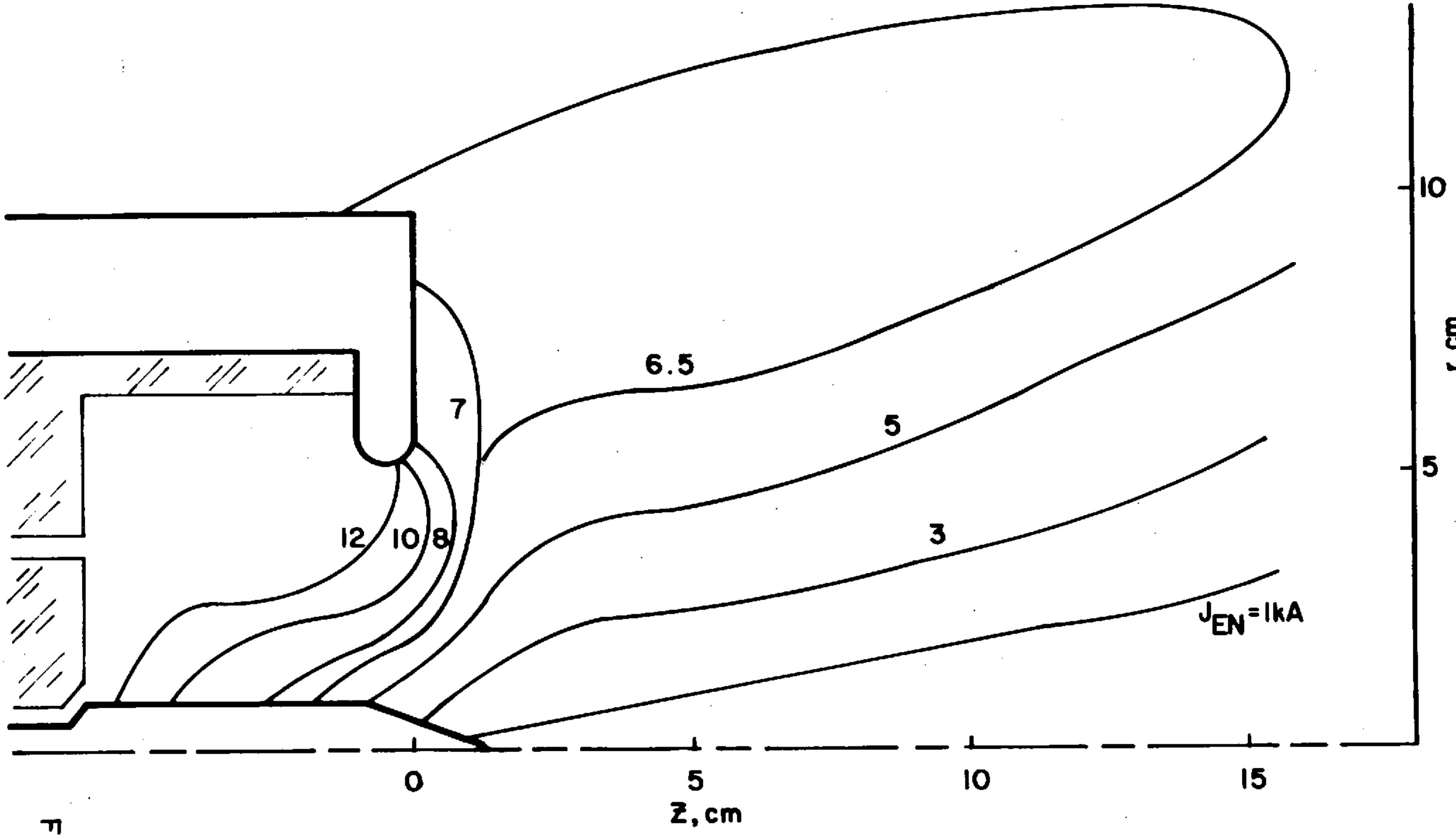

QUASI-STEADY ENCLOSED CURRENT CONTOURS
J= 15.3 kA

FIGURE 4-4
AP25-5052

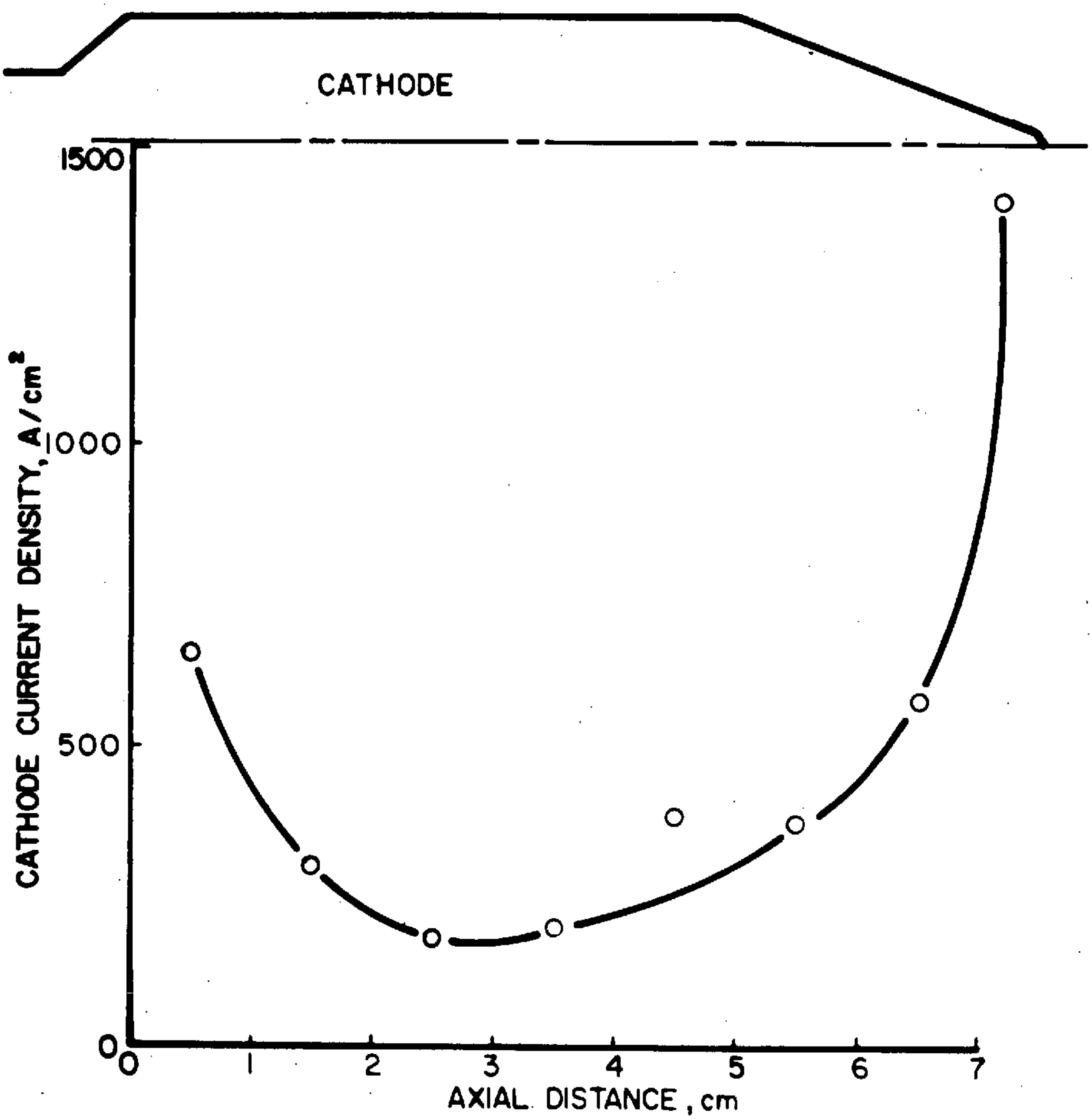

CATHODE CURRENT DENSITY DISTRIBUTION

FIGURE 4-5
AP25-5063

in this exhaust region is primarily axial. This current density pattern is characteristic of the moderate magnetic Reynolds number, O(1-10), associated with the discharge flow.

IV-4-3 Potential Patterns and Electric Fields in the MPD Discharge

The local electric fields, which integrate to the terminal arc voltage, arise as a result of current conduction across the flowing, finite conductivity discharge plasma. Current conduction processes across the electrode-plasma interfaces also create potential gradients commonly referred to as electrode falls.

The local electric field equals the gradient in plasma potential which, in turn, is related to the experimentally measurable floating potential. For small distances over which the gradients in electron temperature, flow vector, and collision frequencies are negligible, the electric field may be evaluated from the difference in floating potential. The quasi-steady distribution of equi-floating potential contours is shown in Figure 4-6. The cathode is at 115 volts negative with respect to the anode ground. The labelled equi-potential contours are also negative with respect to the ground, the negative signs being omitted from Figure 4-6 for convenience. 20 and 90 volt contours envelope the anode and cathode regions respectively. The equi-potential contours in the outer radial regions of the downstream exhaust are approximately parallel to the current streamlines.

IV-4-4 $\bar{j}\cdot\bar{E}$ Power Deposition in the MPD Discharge

Evaluation of the total arcjet power distribution throughout the MPD accelerator requires local evaluation of $\bar{j}\cdot\bar{E}$, the dot product between the current density and electric field vectors. For this purpose, the accelerator may be subdivided into several separate regions, A through F, as is done in Figure 4-7. These regions, excluding the electrode fall

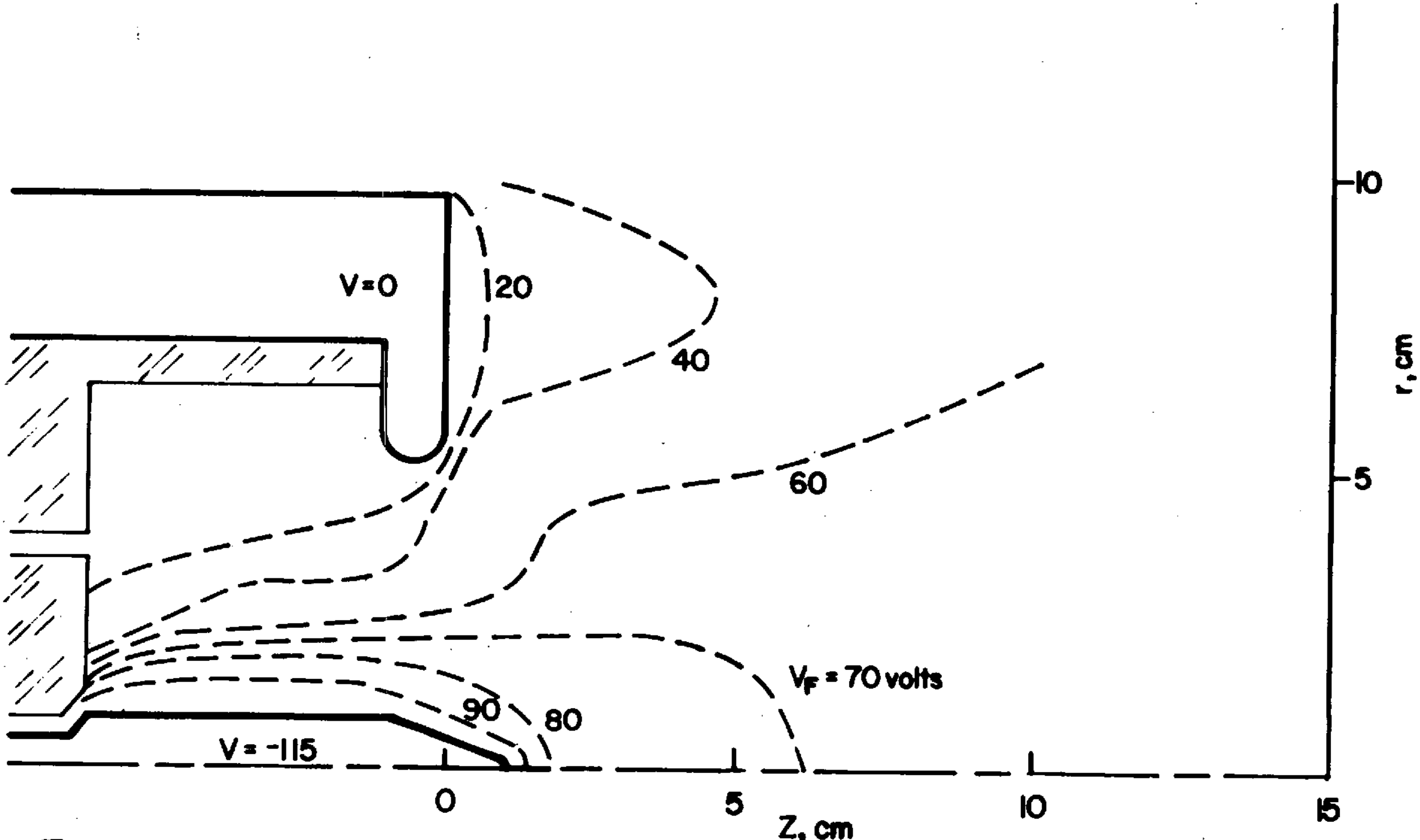

QUASI - STEADY FLOATING POTENTIAL CONTOURS

FIGURE 4-6
AP25-5055

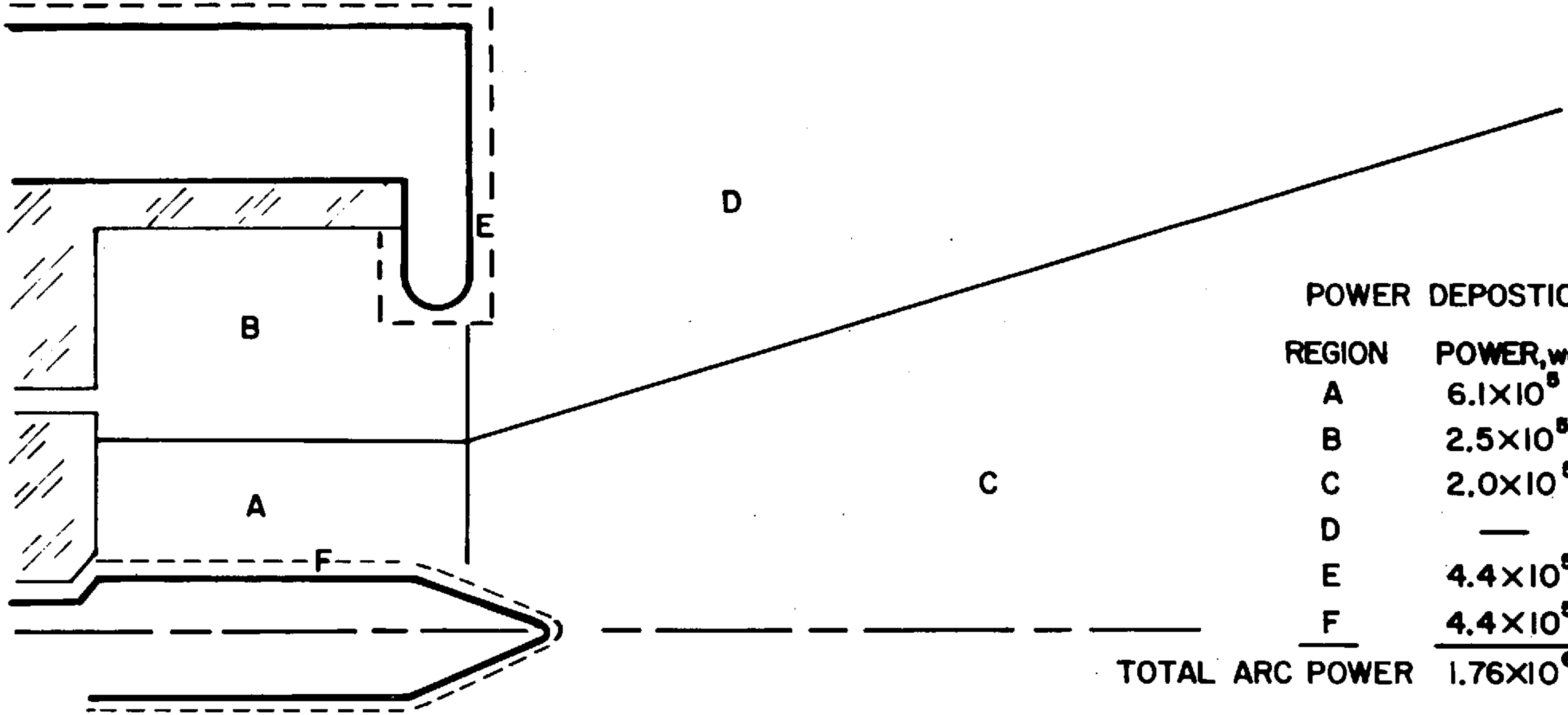

POWER DEPOSTION

REGION	POWER, watts
A	6.1×10^5
B	2.5×10^5
C	2.0×10^5
D	—
E	4.4×10^5
F	4.4×10^5
TOTAL ARC POWER	1.76×10^6

$\bar{j}\cdot\bar{E}$ POWER DISTRIBUTION

FIGURE 4-7
AP25-5070

regions E and F, are further divided into incremental volume elements in which average values for the magnitude and direction of the $\bar{j}$ and $\bar{E}$ vectors are assigned. The product of local power density and incremental volume element when summed over each region represents the total electrical power deposited in that region. This regional power deposition is summarized in Table I. At 15.3 kA and 6 g/sec the total arc power is 1.76 megawatts.

TABLE I

Region	$(\bar{j}\cdot\bar{E})$(vol),watts	Region description
A	6.1×10^5	inner chamber flow
B	2.5×10^5	outer chamber flow
C	2.0×10^4	inner exhaust flow
D	---	outer exhaust flow
E	4.4×10^5	anode fall
F	4.4×10^5	cathode fall
Total Arc Power	1.76×10^6	

To first order, no power addition appears in region D of the discharge because the electric field is perpendicular to the current density vector, thereby making $\bar{j}\cdot\bar{E}$ zero throughout the volume. The power lost to the anode in region E is estimated from recent work relating anode power fraction to total arc power in the quasi-steady MPD discharge.(42) For $J^2/\dot{m} = 40$ kA^2-sec/g, these results extrapolate to an anode power fraction of 25%; i.e. 25% of the total arc power or 4.4×10^5 watts is accounted for by loss mechanisms in the vicinity of the anode. With the anode fall and bulk plasma flow regions accounted for, the remaining input power must appear in the cathode fall region F to provide an overall power balance of the arc.

The distribution of local power deposition for the MPD accelerator operating at 15.3 kA and 6 g/sec may now be summarized: Approximately fifty percent of the total arc power is invested in the plasma flow which occupies regions A, B, C, and D in Figure 4-7. The major power addition to the plasma flow occurs within the discharge chamber, with negligible power addition ensuing in the downstream exhaust. The remaining fifty percent of the total power appears in the electrode fall regions of the discharge.

IV-5 Flow Field Characteristics of the MPD Discharge

IV-5-1 Flow Directions

The flow pattern in the exhaust of the accelerator is determined from velocity vector measurements. Local flow directions are measured using the flow angle probe technique discussed earlier in Section II-2-2a. The mass streamlines constructed from these local flow angles parallel the current streamlines in the inner exhaust region C depicted in Figure 4-7. Precise flow vector measurements in the outer exhaust region D are difficult to obtain due to a decrease in the probe's sensitivity to the flow orientation. Despite this decreased accuracy, flow vectors not parallel to the current streamlines are identified. The mass streamlines appear to diverge more rapidly than the current streamlines in the outer exhaust region.

IV-5-2 Flow Mach Numbers

The flow in region C of the exhaust is supersonic. Bow shocks are photographed off the hemispherical tips of rods introduced into this inner flow several centimeters downstream of the anode orifice. Oblique shocks attached to wedges of different turning angles are also observed. As these wedges are moved axially inward towards the anode plane, the oblique shock angles increase indicative of lower incident flow Mach numbers. Finally no shocks are seen in the vicinity of the anode orifice indicating near sonic conditions there.

Insufficient knowledge of the shocked plasma's thermodynamic state precludes exact Mach number calculations from the shock angle data. However, the oblique shock relations for a perfect gas with an appropriate ratio of specific heats provide a first order estimate.(43) Using this method, the flow Mach number seven centimeters downstream of the anode orifice is estimated between two and three.

IV-5-3 Luminosity Patterns

Photographs through narrow band spectral filters display the luminosity patterns of the discharge. Spectrograms of the discharge reveal singly ionized argon (AII) as the predominant species. Argon II line radiation in the downstream exhaust extends to radii beyond the anode barrel of the accelerator although the spectral intensity monotonically decreases with radius. Referring again to Figure 4-7, the predominant argon II radiation photographed through a 4880 Å filter is confined to the inner flow regions A and C. The outer edge of the AII luminosity in region C coincides with a mass streamline previously defined by the velocity vector measurements in Section IV-5-1. The correspondance among the 4880 Å AII luminosity boundary, the mass streamline and the demarcation of the A-C and B-D flow regions is illustrated in Figure 4-8 where all three are superimposed together.

The remaining regions of the discharge, B and D, are essentially dark, except for a small toroidal volume located in the anode plane between the anode lip and region A.

IV-6 Quasi-steady MPD Acceleration Processes

Having discussed the pertinent electromagnetic and flow field characteristics of the MPD discharge, a model of the acceleration mechanisms responsible for the measured plasma velocity profile may be constructed. A complete description of the flow processes would require additional profiles of

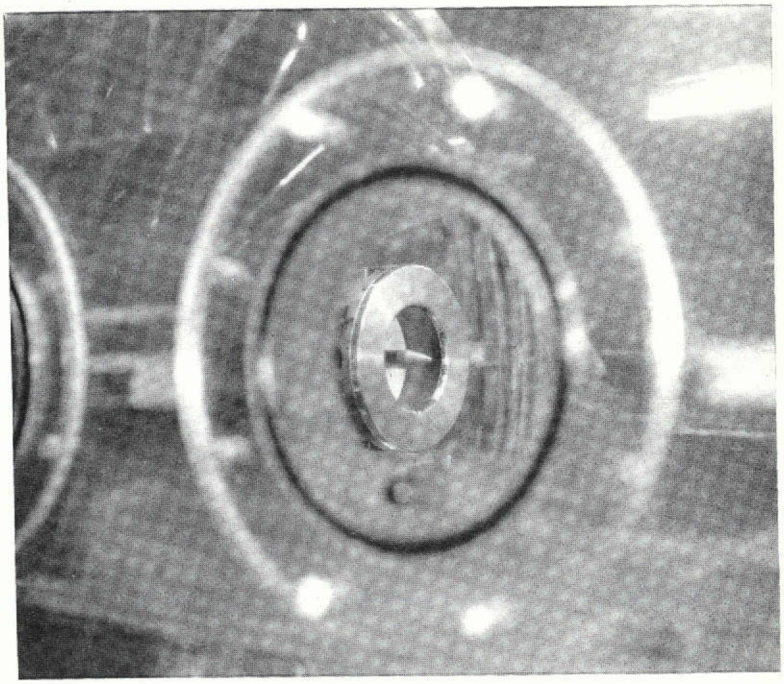

a) REFERENCE PERSPECTIVE

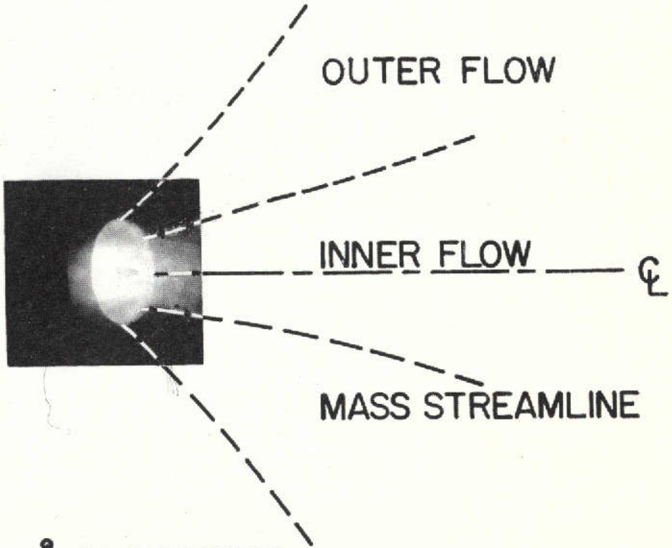

b) 4880Å LUMINOSITY

ARGON II LUMINOSITY PATTERNS

FIGURE 4-8

AP25P·527

number density, ion and electron temperatures, and pressure throughout the discharge. For this arcjet configuration, these profiles have not yet been determined. However, reasonable estimates of these variables based upon previous measurements for other configurations may be made, when appropriate. This allows a phenomenological model of the plasma acceleration process to be formulated.

IV-6-1 Two-Flow Plasma Acceleration Model

The total injected argon propellant is divided into two independent mass flows associated with chamber injection at large and small radii. The local power deposition and luminosity profiles in regions A and B of the discharge chamber suggest this flow division is essentially maintained as the two flows are accelerated axially downstream out of the chamber and into the exhaust regions. The plasma acceleration process will thus be modelled in terms of two separate inner and outer propellant flows, schematically illustrated in Figure 4-9.

Inner and outer flow separation is a consequence of the electromagnetic discharge structure within the accelerator chamber. In particular, there are substantial differences between the axial power deposition profiles for the two flow regions. Figure 4-10 compares the incremental power addition to each flow as a function of axial distance downstream from their respective injection orifices. Approximately 180 kW are deposited immediately in the inner flow as it emerges from the cathode base injection annulus. This power level is commensurate with complete single ionization of the injected 3 g/sec argon. Once ionized, the prevailing $\bar{j} \times \bar{B}$ body forces tend to confine radially and accelerate axially the inner flow. Only after leaving the discharge chamber does the inner flow expand radially.

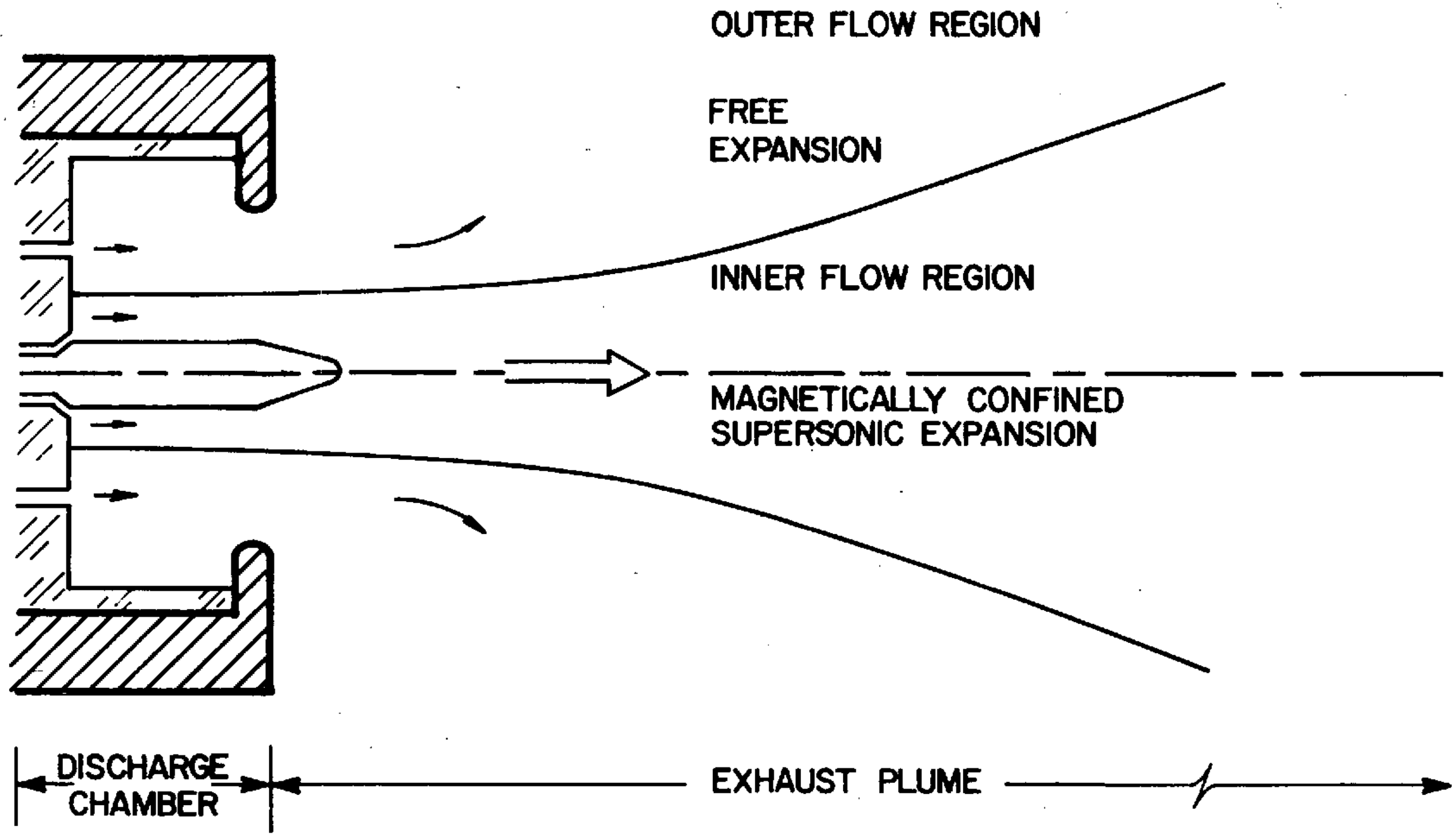

TWO-FLOW ACCELERATION MODEL

FIGURE 4-9

AP25·5059

FIGURE 4-9
AP25·5059

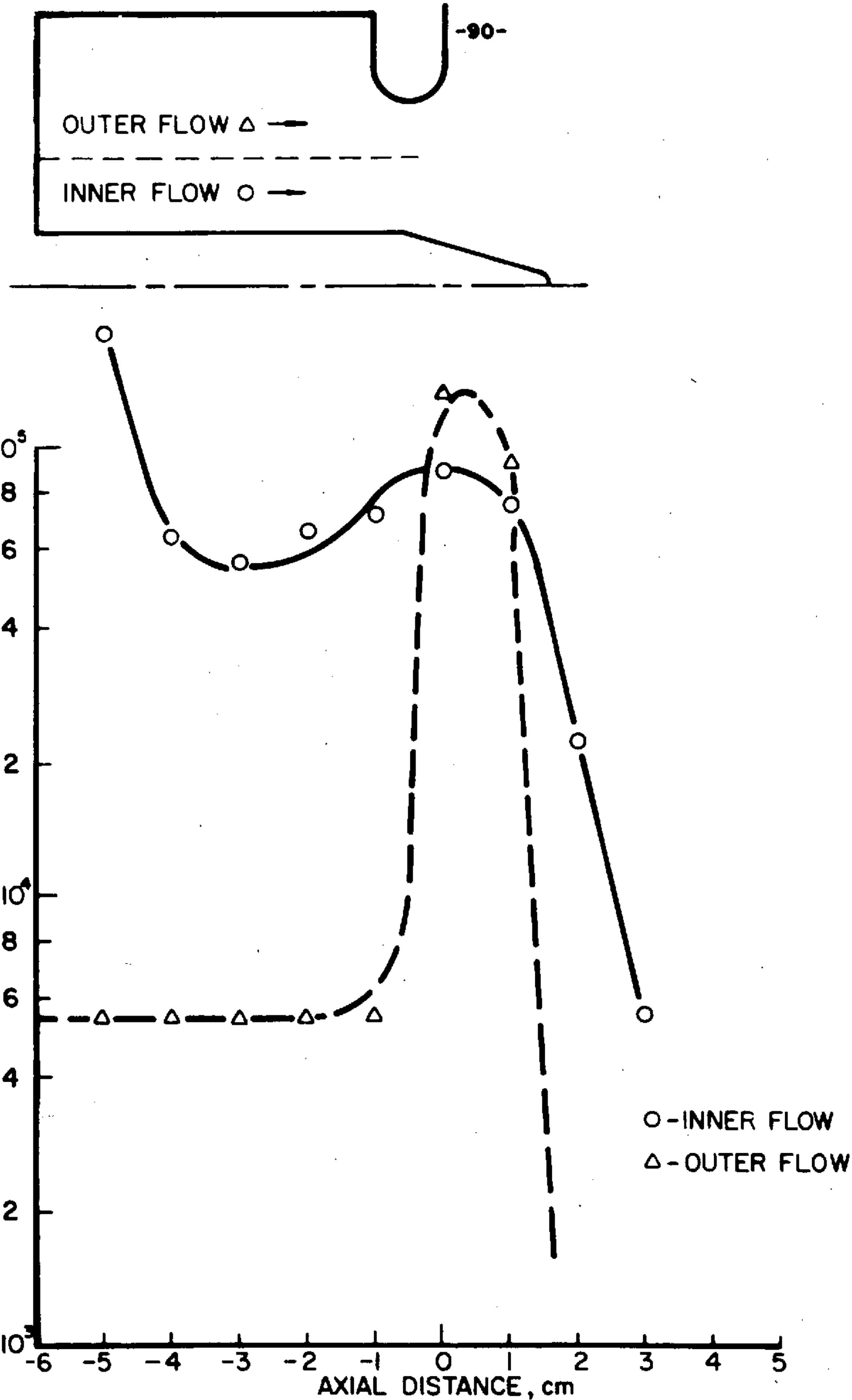

INCREMENTAL INPUT POWER PROFILES

FIGURE 4-10

AP 25-5054

C ~ 2

In contrast, negligible input power appears in the outer flow upstream of the anode lip region. A total of only 27 kW is deposited in this region. Thus, it may be inferred that only a small fraction of the 3 g/sec outer mass flow rate is ionized upstream of the anode. This is also consistent with the absence of ionized argon line radiation in this region of the discharge. In addition the local current density and magnetic field are substantially lower in this region. As a consequence of the weak local Lorentz forces, the initial axial flow direction of the outer propellant stream will be only slightly perturbed. To this approximation, the integrity of the two concentric inner and outer flows is preserved as they are accelerated downstream.

IV-6-2 Inner Flow Region

Two-thirds of the electrical input power invested in all the plasma flow regions appears as total enthalpy of the inner propellant flow. In addition, nearly 100 percent of this inner flow power addition is accomplished within the discharge chamber as shown in Figure 4-11. Negligible power addition occurs in the exhaust. The discharge chamber and exhaust plume regions of the inner flow are distinguishable by this localization of power input. As such, the flow processes within each will be treated separately.

IV-6-2a Discharge Chamber

The inner propellant mass flow is ionized, heated, and accelerated through the sonic point within the discharge chamber. The net result of these processes may be examined in terms of a power balance across the region.

The total input power, P_T, invested in the inner flow within the discharge chamber is 6.1×10^5 watts, exclusive of the cathode fall power. Of this total, a certain amount, P_R, is lost through radiative processes. The remaining power appears

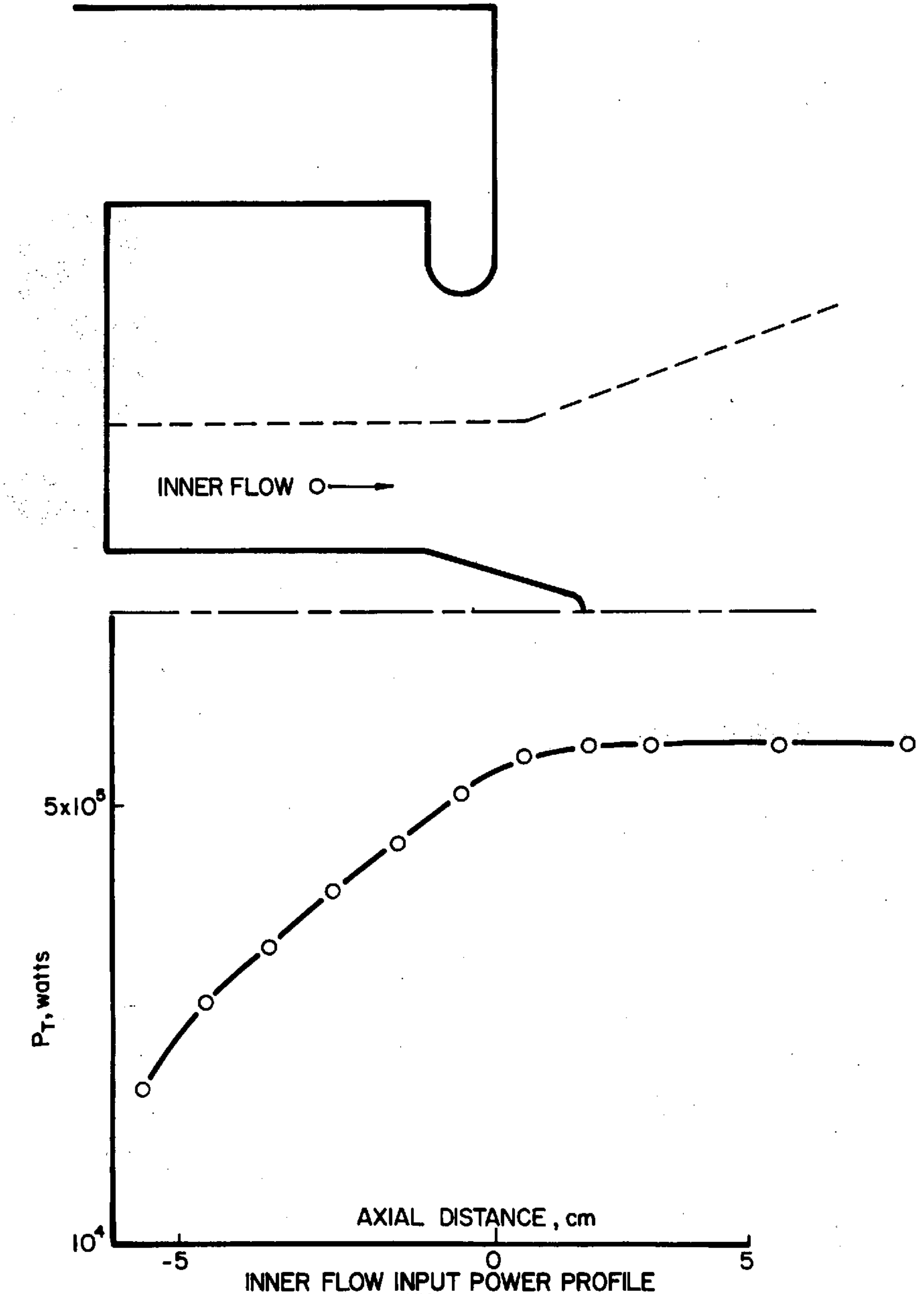

INNER FLOW INPUT POWER PROFILE
FIGURE 4-11
AP 25-5056

directly in the flow.

$$P_{FLOW} = P_T - P_R \tag{4-b}$$

This flow power is partitioned between enthalpic and kinetic modes.

$$P_{FLOW} = \dot{m}\ (h + u^2/2) \tag{4-c}$$

where $\dot{m}$ is the accelerated mass flow rate, h the flow enthalpy, and u the mean flow velocity.

A quasi-equilibrium expression for the flow enthalpy is assumed, in the form

$$h = \int_{o}^{T_e} C_p(T,p)\ dT + 5/2\ R \int_{T_e}^{T_i} dT \tag{4-d}$$

where T_e and T_i are the electron and ion temperatures, C_p is the heat capacity at constant pressure and R equals the argon gas constant. The first integral in Equation 4-d represents the contribution to the flow enthalpy from both excitation and ionization as well as the energy content of the ion and electron random motion at temperature T_e.(44) Generally the excitation and ionization processes in devices of this type limit the electron temperature to between one and two volts. After initially being ionized, the plasma experiences a significant axial acceleration. The resulting high velocities are characterized by flow times short compared to characteristic electron-ion energy equi-partition times(37) thereby establishing a non-equilibrium situation. Because electron-ion collisions are unable to establish an equilibrium temperature distribution in time, additional enthalpy appears in ion random motion alone, thereby raising the ion temperature above the electron temperature. This non-equilibrium effect is accounted for by the second integral in Equation 4-d.

Equations 4-b, 4-c, and 4-d may be rearranged to express the flow velocity in terms of input and radiated power, accelerated mass flow rate, pressure and electron and ion temperatures such that:

$$u = \left[2\left(\frac{P_T - P_R}{\dot{m}} + 5/2\ R\ (T_e - T_i) - \int_0^{T_e} c_p(p,T)\ dT\right)\right]^{\frac{1}{2}} \qquad (4\text{-e})$$

Order of magnitude estimates of P_R, p, T_e and T_i at a given axial location are required to calculate the local flow velocity from the measured power input up to that point. The measurement techniques for any one of these variables require a major experimental effort in terms of the sophistication and time demanded by the particular measurement. In lieu of their actual measurement, these estimates must rely upon previous data obtained at similar operating conditions, albeit for different arcjet configurations.

Plasma radiation phenomena in an environment of this type are extremely complex. An exact formulation of the input power radiated away by bremmstrahlung and line radiation is beyond the scope of this work. The power density radiated in free-free transitions for a Maxwellian electron distribution is given by Spitzer as:

$$P_{ff} = 1.42 \times 10^{-34}\ Z^2\ n_e n_i\ T_e^{\frac{1}{2}}\ \text{watts/cm}^3 \qquad (4\text{-f})$$

where Z is the ion charge number and $n_{e,i}$ are the electron and ion number densities.(37) For a singly ionized argon plasma with an electron number density equal to 10^{15} cm^{-3} and T_e between one and two volts:

$$P_{ff} = 0\ (\ 1\ \text{watt/cm}^3)$$

The power radiated away by bremmstrahlung from the 10^2 cm^3 inner flow volume may be approximated as:

$$P_R^{ff} = P_{ff}\ (Vol) \ = 0(10^2 \text{ watts})$$

a negligible amount relative to the total input power. However, power losses from bound-bound transitions may be significant. A line radiation flux of 2000 watts/cm^2 has previously been found typical of this plasma environment.(45) The luminous inner flow region within the discharge chamber radiates from a surface area of $0(10^2\ cm^2)$. From this surface,

$$P_R^{bb} = 0(2 \times 10^5 \text{ watts})$$

will be radiated away. The assumption of no recombination within this discharge region implies the power loss from free-bound transitions is negligible. The total input power lost to radiation is therefore

$$P_R = P_R^{bb} + P_R^{ff} = 0(2 \times 10^5 \text{ watts})$$

Electron temperatures consistent with previous probe measurements and observed levels of ionization, pressures inferred from static pressure measurements in the discharge chamber, and argon ion temperatures extrapolated from Doppler width data are listed below.(16,17,46)

$$T_e = 0(19{,}000\ ^oK)$$
$$p = 0(10^{-2}\text{-}10^{-1} atm)$$
$$T_i = 0(60{,}000\ ^oK)$$

For $P_T = 6.1 \times 10^5$ watts just outside the discharge chamber and an accelerated inner mass flow rate of 3 g/sec, the corresponding exit velocity is calculated from Equation 4-e to be $8.0 \leq u_e \leq 10.4$ km/sec. The experimentally measured plasma velocity 2 centimeters downstream is 9.6 ± .4 km/sec. The inner propellant flow thus is slightly supersonic as it departs the discharge chamber with an elevated ion temperature and an electron temperature consistent with the conductivity requirements of the discharge.

IV-6-2b Exhaust Plume

The flow in the inner exhaust plume of the discharge is accelerated supersonically to a final velocity of 12.5 km/sec. This acceleration region extends several anode orifice diameters downstream. Within this region the electromagnetic body forces are normal to the flow streamlines (Section IV-5-1). Thus, electromagnetic body forces tend to confine rather than accelerate the flow in the streamwise direction. The axial acceleration, however, may be accounted for by the radial divergence of the hot, electromagnetically confined inner plasma flow.

The mathematical description of the expansion process is significantly simplified for one-dimensional flows. Radial profiles of velocity and number density at several axial locations justify the 1-D assumption as a first approximation of the flow field. The one-dimensional mass, momentum, and energy relations for a given streamtube may be written as:(47)

$$d(\rho uA) = 0 \tag{4-g}$$

$$\rho udu + dp = 0 \tag{4-h}$$

$$dh + udu = dq \tag{4-i}$$

where A is the normal streamtube area, dq the energy addition per unit mass from Joule heating, and ρ, u, p, and h the common nomenclature for density, velocity, pressure, and enthalpy. The flow enthalpy may be expressed as

$$h = 5/2\ p/\rho + h_I \tag{4-j}$$

where h_I is the internal energy content due to excitation and ionization. The energy addition, dq, to the expanding flow is found to be insignificant compared to the total energy content (Section IV-4-4). Thus, dq may be approximated as zero.

Significant argon ion recombination (AIII → AII or AII → AI) in this exhaust region of the discharge has not been experimentally observed.(48) Recombination times for these processes are characteristically long, compared to local flow times. This suggests the plasma flow may be treated as frozen, i.e.,

$$dh_I = 0$$

Hence, the one-dimensional energy equation becomes

$$d(5/2\ p/\rho) + u\,du = 0 \tag{4-k}$$

Equation 4-k integrates to

$$5/2\ \ p/\rho + u^2/2 = K \tag{4-l}$$

where the integration constant K represents the total specific flow enthalpy exclusive of excitation and ionization energies, The constant K may be evaluated from either the sonic velocity u^* or the maximum velocity u_{max} according to Equation 4-m.

$$K = \frac{5+\gamma}{2\gamma}\ u^{*2} = \frac{u_{max}^{\ 2}}{2} \tag{4-m}$$

where the sonic condition $\gamma p^*/\rho^* = u^{*2}$ has been used.

Equations 4-g, 4-h, 4-k, and 4-m may be solved for the streamline area as a function of u, K, and the minimum area A^*. It is easily shown that

$$A/A^* = \left[\frac{K - u^{*2}/2}{K - u^2/2}\right]^{3/2} \left(\frac{u^*}{u}\right) \qquad (4\text{-n})$$

or, in terms of the streamtube radius r,

$$r = r^* \left[\frac{K - u^{*2}/2}{K - u^2/2}\right]^{3/4} \left(\frac{u^*}{u}\right)^{1/2} \qquad (4\text{-o})$$

Mass streamline coordinates $r(z)$ for given r^* values may be calculated when the measured axial velocity profile $u(z)$ in Figure 4-2 is substituted into Equation 4-o. K and u^* are evaluated from $u_{max} = 12.5$ km/sec. The flow streamlines associated with $r^* = 1.0$, 1.5, and 2.0 centimeters are shown in Figure 4-12. Circular and triangular data symbols represent two experimentally measured streamlines. The circular data symbols also represent the outermost boundary of the AII luminosity photographed through the 4880 Å filter. Streamline agreement between the one-dimensional expansion model and the experimental data is excellent. Thus, the downstream acceleration of the inner propellant flow may be accounted for by the radial expansion of the high enthalpy plasma discharged from the accelerator chamber.

Questions may arise as to the sensitivity of these results to the shape of the measured velocity profile and the assumption of negligible recombination in the expanding flow. The above calculations were repeated for an arbitrarily chosen linear velocity profile substituted for the measured profile of Figure 4-2. The corresponding streamline shapes calculated from Equation 4-o for the linear profile differed noticeably from the experimentally measured flow directions. Recombination enthalpy was arbitrarily introduced onto the flow by including dh_I in Equation 4-k. Even for relatively small degrees of assumed

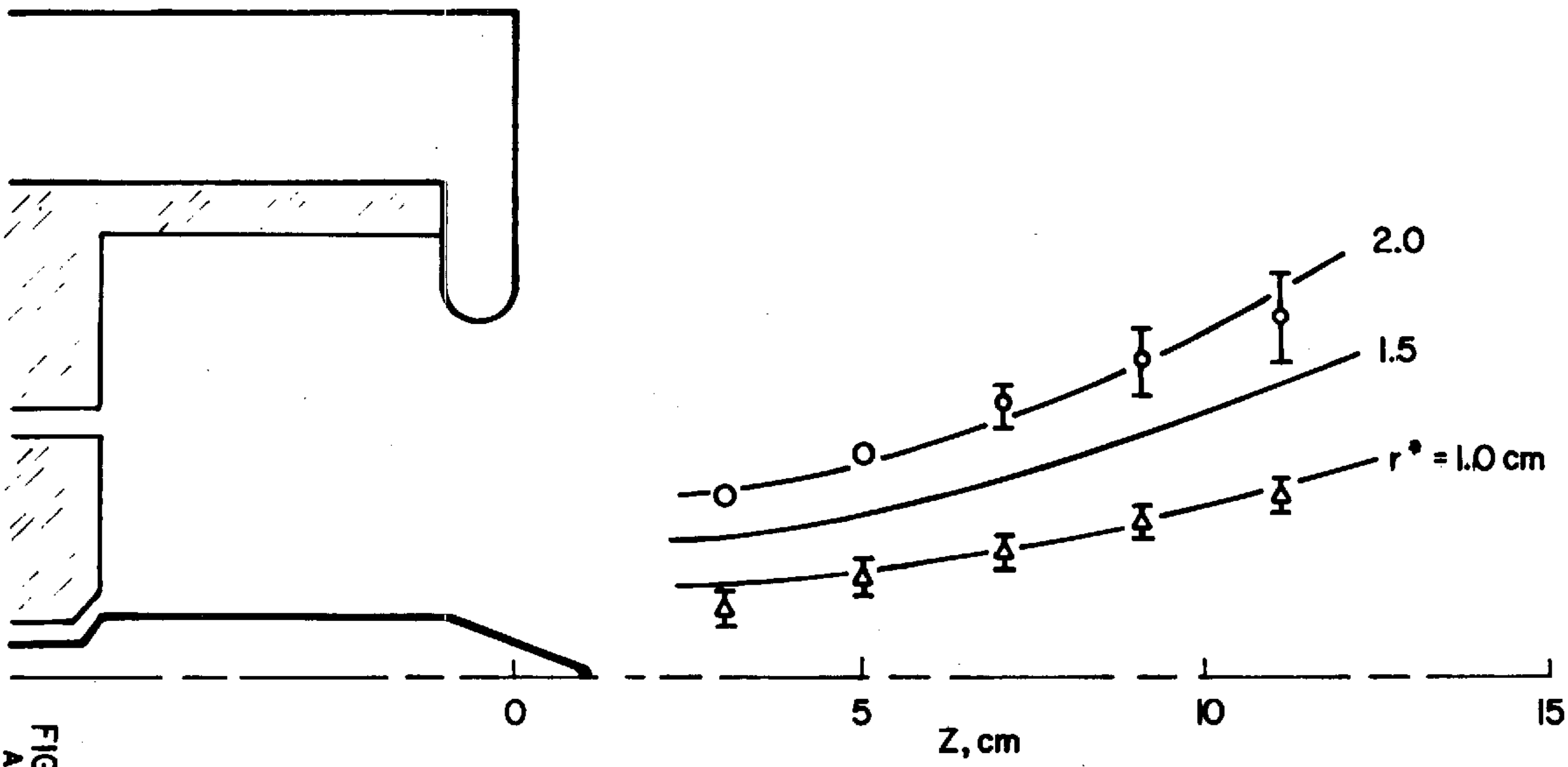

CALCULATED AND EXPERIMENTAL MASS STREAMLINES

FIGURE 4-12
AP25-5057

recombination, the calculated streamlines bore no resemblance to the measured flow patterns.

IV-6-3 Outer Flow Region

Plasma acceleration appears qualitatively less significant in the outer flow regions of the discharge. Reduced levels of power addition, local $\bar{j} \times \bar{B}$, and luminosity suggest lower velocities, densities, and ion temperatures in the outer flow. Estimates of these temperatures and velocities may be made in the same spirit as in Section IV-6-2.

IV-6-3a Discharge Chamber

The interesting feature of the outer flow inside the discharge chamber is the localization of power addition off the tip of the anode previously illustrated in Figure 4-10. Because of this, significant ionization of the injected propellant is delayed until the flow enters the vicinity of the anode orifice. The local power addition there is commensurate with full ionization of the incident propellant flux. It should be recalled that outer flow mass injection was originally required to prevent severe terminal voltage fluctuations and minimize the total arc voltage. Similar behavior has been reported for different arcjet configurations operating at conditions where the anode region appears locally "starved" of propellant. One may speculate that the outer flow functions primarily to provide a source of conduction electrons in the vicinity of the plasma-anode interface.

The outer flow plasma velocity in the anode plane may be estimated using the power balance Equation 4-e. However, ion temperatures in this region of the discharge have not been previously measured. To circumvent this problem, advantage may be made of the near sonic conditions existing in the vicinity of the anode orifice (Section IV-5-2). The ion temperature may be expressed in terms of the acoustic speed c_s,

$$c_s^2 = R (\gamma_e T_e + \gamma_i T_i)$$

where $\gamma_{e,i}$ are the respective electron and ion specific heat ratios. Since the acoustic speed equals the flow velocity at the sonic point, the ion temperature may be expressed as,

$$T_i = \frac{u^{*2}}{\gamma_i R} - \frac{\gamma_e}{\gamma_i} T_e \qquad (4\text{-p})$$

Using Equation 4-p, Equation 4-e may be rearranged to express the flow velocity u^* in terms of P^*_{FLOW}, $\dot{m}$, and T_e^* evaluated at the sonic point. Electron temperatures on the same order as the inner flow are assumed, i.e. 0(19,000 °K). The electrical power input to the outer flow within the discharge chamber is 2.5×10^5 watts. This input power level accordingly accelerates the 3 g/sec outer flow rate to velocities less than 4500 m/sec and heats the ions to temperatures below 40,000 °K. Both these values are approximately a factor of two less than the inner flow velocity and ion temperature at a similar axial station.

IV-6-3b Exhaust Plume

The mass streamlines measured in the outer exhaust plume flow of the accelerator do not parallel the local current streamlines. The more rapid radial divergence of the outer exhaust flow indicates only partial magnetic confinement. The expansion process in this region of the discharge should therefore more closely resemble that of a free expansion from a sonic orifice. The details of the outer exhaust flow field were not considered.

IV-6-4 Specific Impulse of the MPD Discharge Flow

The specific impulse of the quasi-steady plasma accelerator, defined by Equation 4-q, is an important parameter used to evaluate thruster performance.

$$I_{sp} = T/\dot{m}g \tag{4-q}$$

where T is the thrust produced by the acceleration of the mass flow rate $\dot{m}$ and g is the standard acceleration of gravity. The AVCO critical $J^2/\dot{m}$ model implies an upper limit of 890 seconds for the quasi-steady acceleration of argon propellant (Section I-3-4). The foregoing results of the two-flow plasma acceleration model may be examined in light of this claim. In order to do this the thrust producing regions of the discharge must first be identified.

The thrust produced by the quasi-steady MPD arcjet is both electromagnetic and electrothermal in origin. Electromagnetic thrust arises from the coupling among the vector components of the current density and azimuthal self-magnetic field of the discharge. Both axial and radial Lorentz body forces result from radial and axial current flow respectively. The $j_r B_\theta$ body forces ("electromagnetic blowing") directly accelerate the propellant downstream imparting thrust to the arcjet through the interaction between the current flow in the discharge plasma and the accelerator circuitry. The magnitude of the "blowing" thrust component may be calculated by integrating the Maxwell stress tensor over any convenient surface which encloses the discharge current pattern.(1) The radial or "pumping" $j_z B_\theta$ forces confine the discharge plasma and support radial pressure gradients similar to those found in classical pinch discharges. The thrust contribution from these "electromagnetic pumping" forces may be evaluated by integrating the pressure distributions caused by this magnetic confinement over those surfaces normal to the accelerator's symmetry axis. Thrust results from the overpressure generated on these surfaces.

Electrothermal or aerodynamic thrust generation is a consequence of the discharge plasma being resistively heated. As a result, the unbalanced pressure on the discharge chamber walls and any subsequent nozzle-like flow expansion in the exhaust will impart additional thrust to the device. The proper evaluation of the electrothermal thrust component is not straightforward. Conventionally, aerodynamic thrust is expressed in terms of a nozzle discharge coefficient. However, the appropriate discharge coefficients and chamber pressures for the quasi-steady MPD arc are generally unknown. Usually therefore, one must rely upon specific experimental results to estimate the magnitude of the electrothermal thrust component.

The thrust attributable to the inner and outer flows may be estimated from the experimental data taken at $J = 15.3$ kA and $\dot{m} = 6$ g/sec. The details of the thrust calculations are presented in Appendix A and the results are summarized below.

Inner flow:

$$\begin{aligned} T^I &= T^I_{em} + T^I_{et} \\ &\cong 28.0 + 9.5 \\ &\cong 37.5 \text{ N} \end{aligned}$$

Outer flow:

$$\begin{aligned} T^O &= T^O_{em} + T^O_{et} \\ &\cong 16.0 + 2.7 \\ &\cong 18.7 \text{ N} \end{aligned}$$

where the superscripts I and O denote the inner and outer flows and the subscripts em and et imply electromagnetic and electrothermal thrust components. The total thrust generated by the

MPD discharge at these conditions is the sum of T^I and T^O and equals,

$$\begin{aligned} T &= T^I + T^O \\ &\cong 56.2 \text{ N} \end{aligned}$$

It is interesting to note that approximately 22% of this total calculated thrust is electrothermal in origin. This T_{et}/T ratio is consistent with previous experimental thrust data which implied the electrothermal thrust fraction of the quasi-steady MPD arcjet was constant and equal to 20% over a wide range of conditions.(16)

Several implications of these thrust data may now be discussed. Since each flow region accelerates three grams per second argon, the mass-averaged velocities corresponding to the inner and outer flow thrusts are,

$$\bar{u}^I = T^I / \dot{m}_I \cong 12.5 \text{ km/sec}$$

$$\bar{u}^O = T^O / \dot{m}_O \cong 6.2 \text{ km/sec}$$

Comparison between these mass averaged velocities and the anode orifice exit velocities of the inner and outer flows suggests that approximately 28% of the arcjet's thrust is recovered during the flow expansion in the downstream exhaust. In addition, the mass averaged velocity $\bar{u}^I$ is in close agreement with the terminal exhaust velocity of 12.3 ± 1.1 km/sec measured in the plume of the inner flow. This velocity also equals the maximum velocity obtainable from the 1-D, nozzle-like expansion of the inner flow discussed in Section IV-6-2b. From this correspondance, it may be inferred that thrust recovery in the downstream exhaust regions of the discharge results from the experimentally observed electromagnetic confinement of the flow.

Finally the specific impulses of the two propellant streams may be calculated.

$$I^I_{sp} = T^I / \dot{m}_I g \cong 1280 \text{ sec.}$$

$$I^O_{sp} = T^O / \dot{m}_O g \cong 640 \text{ sec.}$$

The inner and outer flow regions delineated by the two-flow plasma acceleration model may be further characterized by the disparity between their specific impulses. The inner flow region generates thrust with a specific impulse which considerably exceeds the AVCO limiting I_{sp} of 890 seconds for the quasi-steady acceleration of argon propellant. In contrast, the specific impulse associated with the outer propellant flow falls beneath this limiting value. On combining these two flows, the overall specific impulse of the thruster, equal to the total thrust divided by g times the total mass flow, becomes,

$$I_{sp} = (T^I + T^O) / g(\dot{m}_I + \dot{m}_O) \cong 960 \text{ sec.}$$

which, although lower than I^I_{sp}, still exceeds the minimum flow power model's fundamental limit of 890 seconds.

The implications of the two-flow model and the above results, with respect to improving the performance of the quasi-steady MPD thruster, are clear. Namely, higher accelerator thrust densities and specific impulses should be achieved if the relative importance of the outer flow region is reduced. This could seem to be accomplished by reducing the anode and chamber radii such that the outer flow discharge chamber region is physically eliminated. If, as a result of the chamber geometry change, the inner flow properties remain the same, the specific impulse of the accelerator would increase from ~ 960 to ~ 1280 seconds. It must be recalled, however, that previous variations in the mass injection geometry resulted in increased terminal voltages and erratic arcjet behavior when the outer anode regions were deprived of injected mass (Section III-6-1). Furthermore, power density and luminosity measurements imply ionization phenomena are important in the vicinity of the anode (Sections IV-4-4 and IV-5-3). These data all tend to suggest the function of the outer flow may be primarily related to current conduction processes in the anode region. Since these phenomena and their connection and influence upon the plasma acceleration process are not well understood at this time, it is not clear that this flow region can be eliminated without inducing other significant consequences throughout the remainder of the discharge. Improved MPD thruster performance,realized by enhancing the inner flow characteristics of the discharge at the expense of the outer flow, thus remains to be shown.

Chapter V

Results and Implications

This type of research in electromagnetic gas acceleration is directed toward understanding those operational principles whose judicious manipulation will eventually lead to an efficient space thruster. Toward this end, the quasi-steady MPD research effort at Princeton over the past ten years may be divided conveniently into three eras. The pioneering work of Clark established the fundamentals associated with quasi-steady plasma acceleration.(6) This was followed by a period during which extensive diagnostic development was pursued to better facilitate experimental study of the device. Continued arcjet investigations with these techniques later revealed malfunctions of the original facilities due to insulator ablation. In this perspective, the present work may be summarized in two parts. The first part sought, and took the necessary corrective steps, to provide an accelerator configuration whose operation was independent of certain extraneous influences. The structure of the MPD discharge was then examined to clarify the nature of the quasi-steady plasma acceleration process.

Plexiglas insulator ablation significantly alters the terminal voltage and exhaust velocity characteristics of the accelerator. Refractory insulator material and a revised mass injection configuration enable the quasi-steady accelerator to function properly over an extended range of arc currents and mass flow rates. Nominal arcjet operation is also restricted by the onset of terminal voltage fluctuations. The onset of these fluctuations depends upon the mass flow rate and cathode area. For a given mass flow rate, the voltage oscillations may be forestalled by increasing the surface area of the cathode.

The plasma acceleration process is characterized by nearly 50% of the discharge current flowing downstream of the anode orifice, and by final exhaust velocities which exceed the previously proposed limit for such processes. The electromagnetic structure of the exhaust plume supports a nozzle-like, supersonic expansion which partially accounts for the observed terminal velocity.

From the experiments of this program emerges a two-flow MPD accelerator model distinguished by inner and outer coaxial flows. Of these two flow regions, the inner flow exhibits a more efficient propellant utilization in the generation of thrust. Joule heating and Lorentz body forces account for the observed plasma acceleration consistent with the calculated thrust. The outer flow produces thrust with a low specific impulse, and thus degrades the overall performance of the thruster. One may question the necessity of an outer flow, but we know that a minimum fraction of the total propellant flow rate must be invested in the outer flow regions to maintain a minimum terminal arc voltage for a given current. In light of this ambiguity, the function and significance of the outer flow region in the MPD discharge warrant further attention.

One suggested experiment designed to study this ambiguity could examine the consequences of eliminating the outer flow region by an appropriate reduction in the size of the anode. Specifically, this could be accomplished by altering the anode geometry to approximately conform to the 20 volt equipotential contour in Figure 4-6. If the electromagnetic structure of the outer flow region is superfluous, the original inner flow region should be little changed, in analogy to an electrostatic situation wherein electrode and equipotential surfaces are interchangeable. If, however, the outer flow region and its attendent properties are integral portions of the MPD discharge, the appropriate current density, luminosity and velocity diagnostics should continue to indicate a two-flow discharge pattern. In this case, the manner in which the physics of the outer flow influences the performance characteristics of the quasi-steady MPD accelerator must be pursued.

A second question reopened by the results of this program concerns the definition of the "matched" conditions for efficient arc operation. "Matched", in this sense, refers to the proper scaling relation between the arc current and injected propellant flow rate, and effectively determines the specific impulse for given input parameters. Several previously proposed models suggest the mass flow scales with the square of the arc current. In particular, the data of Clark, and of Malliaris, suggest a value of $J^2/\dot{m} = 40$ kA^2-sec/g for the "matched" quasi-steady acceleration of argon.(6,13) The magnitude and steadiness of the terminal voltage signatures as a function of arc current were used to reach this conclusion. However, the present results discussed in Chapter III demonstrate the terminal voltages recorded by Clark and the voltage fluctuation onset currents observed by Malliaris are, in one case, grossly perturbed by insulator ablation and in the other case, not uniquely defined. Given an appropriate insulator material, mass injection, and cathode geometry, the present data imply no reason why quasi-steady operation above $J^2/\dot{m} = 40$ kA^2-sec/g cannot be realized with argon propellant. Thus, higher thrust densities and specific impulses associated with $J^2/\dot{m} > 40$ kA^2-sec/g operation would seem to be accessible even without the elimination of the outer flow region discussed before.

The present data imply the quasi-steady MPD arcjet is not fundamentally limited in the manner proposed by Malliaris. The phenomena previously used to empirically define this limit have been alternatively interpreted. Measured exhaust velocities and calculated specific impulses exceed their proposed "critical values" and further increases in these parameters appear feasible. However, an indication that a higher current limit may exist, may be found in a closer examination of the accelerator's voltage-current characteristic, Figure 3-17. From these data one may define a thermal arcjet efficiency as,

$$\eta_{th} = \frac{V - V_A - V_C}{V}$$

Physically, η_{th} represents the fraction of input energy which appears as plasma enthalpy during the arc discharge. The remaining input energy fraction is dissipated through electrode, radiative and other MPD loss processes. η_{th} equals the maximum attainable arcjet thrust efficiency for the ideal case wherein all the plasma enthalpy is converted into useful thrust. Figure 5-1 illustrates the functional relationship between the thermal efficiency and the arc current for 6 g/sec. For arc currents less than 20 kA, η_{th} monotonically increases. Above 20 kA, however, the thermal efficiency assumes a constant value of approximately 65%. The experimental uncertainty in the voltage fluctuation onset current, J^*, associated with this accelerator configuration, brackets this thermal efficiency transition point. It should be recalled that J^* phenomena have been tentatively identified with current emission and conduction processes occurring in the vicinity of the cathode. Whether or not this trend indeed represents a fundamental limitation imposed upon quasi-steady arcjet performance by electrode phenomena also deserves further attention.

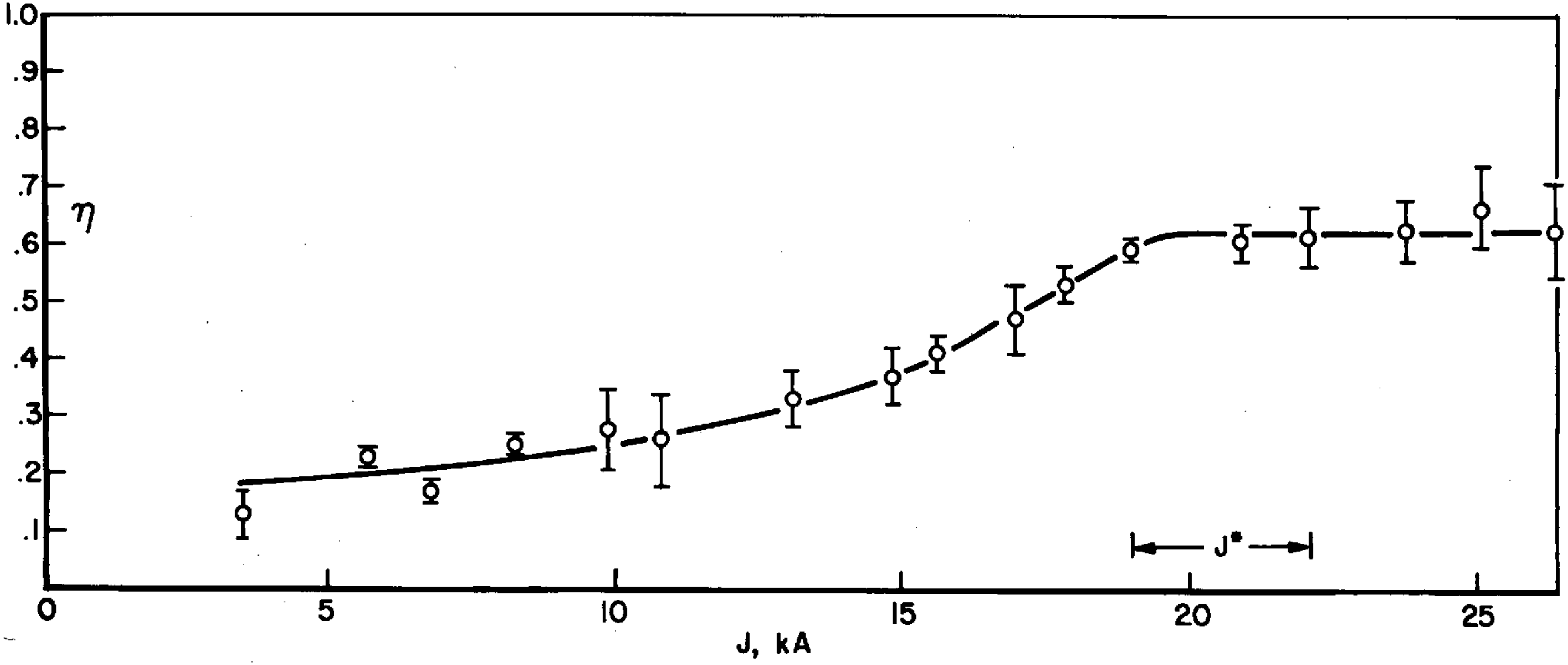

ARCJET THERMAL EFFICIENCY vs ARC CURRENT
$\dot{m}_T$ = 6g/sec, 50:50 FLOW DIVISION

FIGURE 5-1
AP25-5060

Appendix A: Thrust Components of the MPD Discharge

The following appendix details the approximations and calculations made to estimate the thrust produced by the MPD accelerator configuration discussed in Chapter IV. The electromagnetic and electrothermal thrust components of the inner and outer flow regions are separately discussed. Figure A-1 illustrates the characteristic dimensions and surfaces required by the thrust calculations and referred to in the subsequent text. The thrust imparted to the inner propellant flow will be considered first.

A-I Inner flow

Electromagnetic Thrust Contribution

The thrust of the inner mass flow may be treated as the sum of electromagnetic and electrothermal contributions

$$T^I = T^I_{em} + T^I_{et} \tag{A-a}$$

the electromagnetic thrust component may be divided further into "blowing" and "pumping" components defined earlier in Section IV-6-4.

$$T^I_{em} = T^I_b + T^I_p \tag{A-b}$$

The magnitude of the "blowing" component T^I_b is evaluated from a detailed volume integration of the discharge $j_r B_\theta$ pattern or alternatively from the surface integral of the Maxwell stress tensor.$^{(1)}$

$$T_b = \iint_A \bar{\bar{\mathbb{B}}} \cdot \bar{n} \; dA \tag{A-c}$$

where for a self-field accelerator, and a cylindrical geometry,

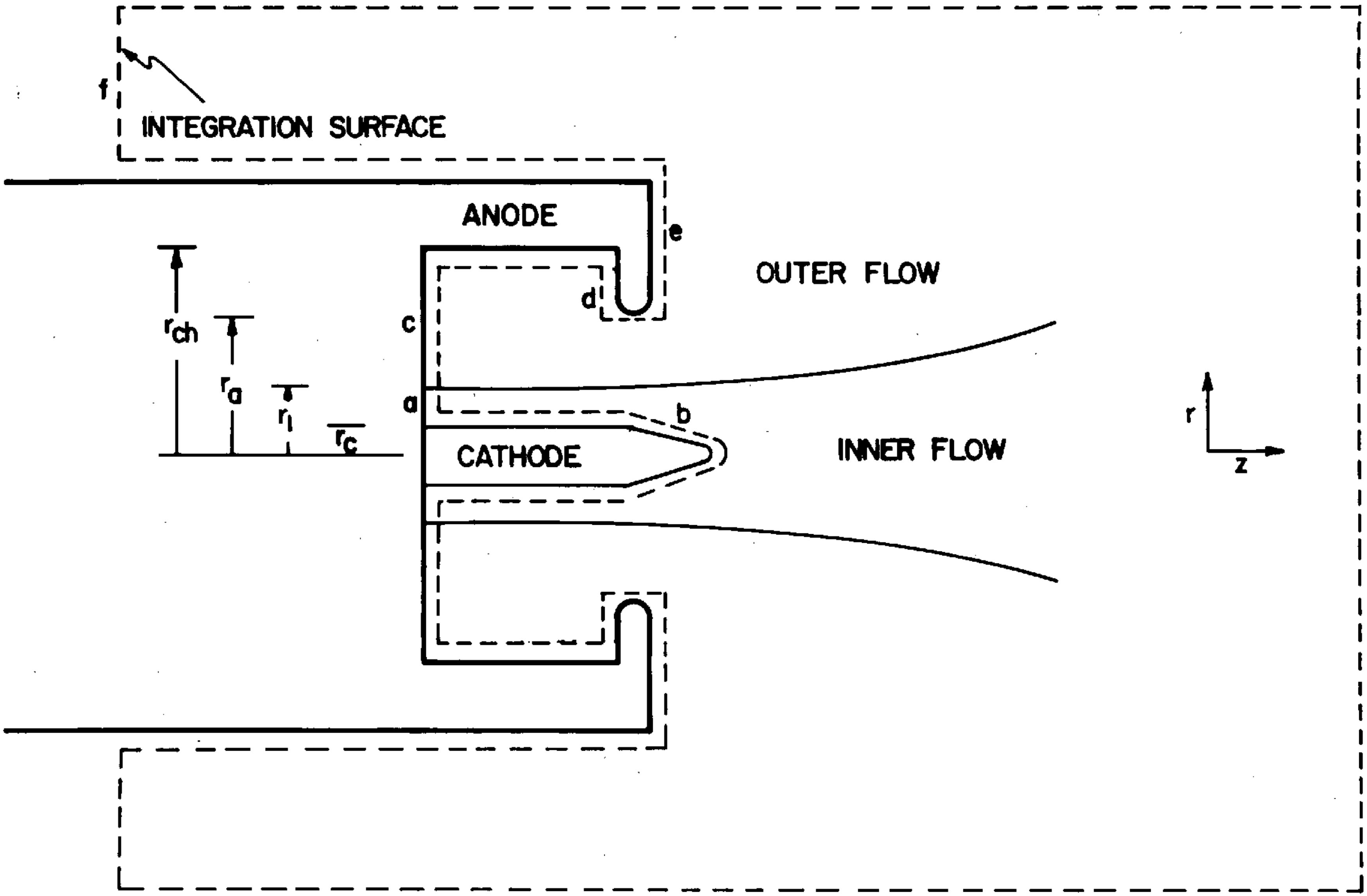

ACCELERATOR SCHEMATIC FOR THRUST CALCULATIONS

FIGURE A-1

AP25-5058

$$\bar{\bar{\mathbb{B}}} = \begin{Bmatrix} -\dfrac{B_\theta^2}{2\mu_o} & 0 & 0 \\ 0 & \dfrac{B_\theta^2}{2\mu_o r^2} & 0 \\ 0 & 0 & -\dfrac{B_\theta^2}{2\mu_o} \end{Bmatrix}$$

and $\bar{n}$ represents the outward normal of the area element dA. The surface of integration, A, must be chosen so as to enclose the entire discharge current pattern. For the following calculations, the integration surface represented by the dashed lines in Figure A-1 is employed.

The integral of $\bar{\bar{\mathbb{B}}} \cdot \bar{n}$ need only be evaluated over those surfaces whose normals have a z component, since the net electromagnetic stresses in the radial direction cancel one another. Specifically then, the "electromagnetic blowing" component of the inner flow equals,

$$T_b^{I} = \iint_a \bar{\bar{\mathbb{B}}} \cdot \bar{n} \; dA_a + \iint_b \bar{\bar{\mathbb{B}}} \cdot \bar{n} \; dA_b \tag{A-d}$$

$$= \int_0^{2\pi} \int_{r_c}^{r_1} \frac{B_a^2}{2\mu_0} \, r \, dr \, d\theta + \int_0^{2\pi} \int_0^{H} \frac{B_b^2}{2\mu_0} \sin\alpha \, (H - z) \frac{\tan\alpha}{\mathrm{tos}\,\alpha} \, d\theta \, dz$$

where $B_{a,b}$ are the self-magnetic fields on the a and b surfaces, and H and α are the height and half angle of the conical cathode tip. The radial and axial dependence of B_a and B_b, determined from the measured quasi-steady magnetic field distribution, and the pertinent cathode tip dimensions are listed below

$$B_a \cong \frac{u_o J}{2\pi r} \qquad (J = 15.3 \text{ kA})$$

$$B_b \cong .093 - 3.66\ z$$

$$H = 2.54 \times 10^{-2} \text{ m}$$

$$\alpha \cong 20^o$$

Substitution of these variables into the integral expressions for T_b^I yields an inner "electromagnetic blowing" thrust component equal to,

$$\begin{aligned} T_b^I &= 27.0 + .5 \\ &= 27.5 \text{ N} \end{aligned}$$

The unbalanced pressure distribution on the end surfaces of the cathode also contributes to the total thrust. This pressure distribution is a consequence of both electromagnetic and electrothermal effects. In order to simplify and separate the two thrust component calculations, an average cathode tip pressure, p_b, taken to represent the actual cathode tip surface pressure distribution, is defined,

$$p_b = p_{anode} + \Delta p \tag{A-e}$$

where p_{anode} equals the plasma pressure in the vicinity of the anode and Δp is the pressure change induced by the interelectrode $j_z B_\theta$ distribution. This pressure change times the conical cathode tip area projected in the axial direction, A_{cath}, defines the electromagnetic "pumping" thrust component.

$$T_p^I = \Delta p \; A_{cath} \tag{A-f}$$

The p_{anode} term is considered electrothermal (aerodynamic) in origin and is discussed subsequently in the section on electrothermal thrust of the inner flow.

Δp is estimated from the radial momentum balance,

$$\frac{dp}{dr} \cong j_z \, B_\theta \tag{A-g}$$

assuming only axial flow to first order. Thus,

$$\Delta p \simeq \int_{anode}^{cathode} j_z \, B_\theta \, dr \tag{A-h}$$

The integral is evaluated graphically using the experimental interelectrode j_z and B_θ distributions.

$$\Delta p \cong 1.6 \times 10^3 \quad N/m^2$$

This pressure combines with $A_{cath} = 3.14 \times 10^{-4}\ m^2$ to yield,

$$T_P^I = \Delta p \, A_{cath} \cong 0.5 \ N$$

The electromagnetic component of the inner flow region thus equals,

$$\begin{aligned} T_{em}^I &= T_b^I + T_p^I \\ &\cong 27.5 + 0.5 \\ &\cong 28.0 \quad N \end{aligned}$$

Electrothermal Thrust Contribution

Evaluation of the electrothermal thrust attributable to the inner flow requires knowledge of the plasma pressures acting against the end wall surface, a, and the cathode tip surface b.

$$T^{I}_{et} = p_a A_a + p_{anode} \quad A_{cath} \tag{A-i}$$

These pressures are estimated from appropriate number densities and charged particle temperatures. The calculation of p_a assumes equal ion and electron temperatures in the plasma adjacent to the end wall of the accelerator. For this case, the equation of state for a perfect gas modified by a compressibility factor, Z, can be written.

$$p_a = Z(p_a, T) \rho \quad R\, T \tag{A-j}$$

The mass density in Equation A-j is given by the one-dimensional continuity equation

$$\rho = \frac{\dot{m}_I}{\bar{u}\, A_a} \tag{A-k}$$

A second relation between p_a and T is provided by the local power deposition $(\bar{j} \cdot \bar{E})$ data and the enthalpy function.

$$h = \frac{P_F}{\dot{m}_I} - \frac{\bar{u}^2}{2} = \int_0^T c_p(p_a, T)\, dT \tag{A-l}$$

$\bar{u}$ in both the state and enthalpy expressions equals the average velocity across the volume element in which the input power P_F appears and is calculated from the axial momentum equation.

$$\rho\, u \frac{du}{dz} \cong j_r \quad B_\theta \tag{A-m}$$

For a negligible inlet velocity, the momentum equation integrates to

$$u_f^{\,2} = \int_0^{\Delta z} \frac{2\, j_r\, B_\theta}{\rho}\, dz$$

which is approximated in terms of average local values for $\bar{j}_r$, $\bar{B}_\theta$ and ρ.

$$u_f^2 = \frac{2\, \bar{j}_r\, \bar{B}_\theta\, \Delta z}{\rho} \qquad \text{(A-n)}$$

Since,

$$\rho = \frac{\dot{m}_I}{\bar{u}\, A_a}$$

and

$$\bar{u} = \frac{u_f}{2}$$

Equation A-n may be rearranged such that,

$$\bar{u} = \frac{\bar{j}_r\, \bar{B}_\theta\, A_a\, \Delta z}{2\, \dot{m}_I} \qquad \text{(A-o)}$$

Combining Equations A-j, A-k, A-l and A-o, one derives,

$$\int_0^T c_p\,(p_a,T)\, dT \equiv f_1(p_a,T) = \frac{P_F}{\dot{m}_I} - \frac{(\bar{j}_r\, \bar{B}_\theta\, A_a\, \Delta z)^2}{8\, \dot{m}_I^2} \qquad \text{(A-p)}$$

$$\frac{p_a}{Z(p_a,T)\, T} \equiv f_2\,(p_a,T) = \frac{2\, R\, \dot{m}_I^2}{\bar{j}_r \bar{B}_\theta A_a^2\, \Delta z}$$

From the experimental data,

$$P_F = 1.78 \times 10^5 \text{ watts}$$

$$\dot{m}_I = 3.0 \times 10^{-3} \text{ kg/sec}$$

$$\bar{j}_r = 4.25 \times 10^6 \text{ amps/m}^2$$

$$\bar{B}_\theta = 1.3 \times 10^{-1} \text{ w/m}^2$$

$$A_a = (r_1^2 - r_c^2)$$

$$= 2.51 \times 10^{-3} \text{ m}^2$$

$$\Delta z = 1.0 \times 10^{-2} \text{ m}^2$$

$$R = 2.07 \times 10^2 \text{ J/kg - }^\circ\text{K}$$

The set of Equations A-p are solved simultaneously for p_a and T using equilibrium thermodynamic tables to evaluate the enthalpy and compressibility functions.(44)

$$T_e = T_i \cong 1.7 \times 10^4 \ ^\circ\text{K}$$

$$p_a \cong 3.6 \times 10^3 \text{ N/m}^2$$

The electrothermal thrust which appears as a result of p_a acting against the inner flow's rear chamber wall is therefore,

$$p_a \ A_a \cong 9.0 \text{ N}$$

This thrust is augmented by the aerodynamic contribution from the cathode end surfaces previously defined as p_{anode} A_{cath}. The pressure off the tip of the anode is approximated by,

$$p_{anode} = n_e \, k \, T_e + n_i \, k \, T_i \qquad \text{(A-q)}$$

n_e and n_i are assumed equal and satisfy the 1-D continuity requirements.

$$n_{e,i} = \frac{\dot{m}_0}{u_0 \pi (r_a^2 - r_1^2) M_i} \tag{A-r}$$

T_e, T_i and u_0 are assumed equal to their outer flow values previously calculated in Section IV-6-3a. Substituting,

$$\dot{m}_0 = 3.0 \times 10^{-3} \quad \text{kg/sec}$$

$$u_0 = 4.5 \times 10^{3} \quad \text{m/sec}$$

$$r_a = 5.1 \times 10^{-2} \quad \text{m}$$

$$r_1 = 3.0 \times 10^{-2} \quad \text{m}$$

$$T_e = 1.9 \times 10^{4} \quad {}^{\circ}\text{K}$$

$$T_i = 4.0 \times 10^{4} \quad {}^{\circ}\text{K}$$

into Equations A-q and A-r,

$$p_{anode} \cong 1.6 \times 10^{3} \quad \text{N/m}^2$$

$$p_{anode}\, A_{cath} \cong 0.5 \quad \text{N}$$

The electrothermal thrust attributable to the inner flow thus equals,

$$\begin{aligned} T_{et}^{I} &= p_a A_a + p_{anode}\, A_{cath} \\ &\cong 9.0 + 0.5 \\ &\cong 9.5 \text{ N} \end{aligned}$$

whereupon the total inner flow thrust becomes,

$$\begin{aligned} T^I &= T^I_{em} + T^I_{et} \\ &\cong 28.0 + 9.5 \\ &\cong 37.5 \quad \mathrm{N} \end{aligned}$$

A-II Outer flow

Electromagnetic Contributions

The "blowing" thrust component of the outer flow is given by,

$$T^O_b = \iint_c \bar{\bar{\mathbb{B}}} \cdot \bar{n} \; dA_c + \iint_d \bar{\bar{\mathbb{B}}} \cdot \bar{n} \; dA_d + \iint_e \bar{\bar{\mathbb{B}}} \cdot \bar{n} \; dA_e \qquad \text{(A-s)}$$

The normal surfaces f and g in Figure A-1 are chosen so as to enclose all the discharge current, thereby making integration on these surfaces unnecessary since the local magnetic field is everywhere zero.

As in the case of the inner flow, each integral is computed using the experimentally measured magnetic field distributions over the three specified surfaces, with the result,

$$T^O_b \cong 16.0 \ \mathrm{N}$$

The "pumping" thrust components generated by the axial current flow into the interior and exterior faces of the anode are calculated to be negligible in comparison to T^O_b. Thus,

$$\begin{aligned} T^O_{em} &= T^O_b + T^O_p \\ &\cong T^O_b \\ &\cong 16.0 \quad \mathrm{N} \end{aligned}$$

Electrothermal Contributions

The plasma pressures adjacent to the annular accelerator surfaces c, d, and e need to be computed to evaluate the outer flow's electrothermal thrust component, T^{O}_{et}.

$$T^{O}_{et} = p_c A_c - p_d A_d + p_e A_e \qquad \text{(A-t)}$$

Similar assumptions and approximations incorporated in the inner flow calculations are repeated here. The backwall pressure, p_c, is estimated from the local input power from which the local ion and electron temperatures are computed.

As before,

$$\begin{aligned} h &= \frac{P_F}{\dot{m}_O} - \frac{\bar{u}^2}{2} = \int_o^T c_p\,(p_c, T)\,dT \\ p_c &= Z\,(p_c, T)\,\rho\,RT \qquad \text{(A-u)} \\ \rho &= \frac{\dot{m}_O}{\bar{u}\,A_c} \end{aligned}$$

The average velocity $\bar{u}$ is equal to the cold gas sonic speed since the local $\bar{j} \times \bar{B}$ acceleration is negligible in this region of the MPD discharge. The other input variables are measured to be,

$$\begin{aligned} P_F &= 5.4 \times 10^3 \text{ watts} \\ \dot{m}_O &= 3.0 \times 10^{-3} \text{ kg/sec} \\ A_c &= \pi\,(r_{ch}^2 - r_1^2) \\ &= 9.84 \times 10^{-3} \text{ m}^2 \end{aligned}$$

which correspond to,

$$T_e = T_i \cong 3.5 \times 10^3 \ {}^oK$$

$$p_c \cong 6.9 \times 10^2 \ N/m^2$$

$$p_c A_c \cong 6.7 \ N$$

The pressure on the interior anode face is derived from expressions similar to Equation A-q and A-r with,

$$\dot{m}_O = 3.0 \times 10^{-3} \ kg/sec$$

$$u_O = 4.5 \times 10^3 \ km/sec$$

$$A_c = \pi (r_{ch}^2 - r_1^2)$$

$$T_e = 1.9 \times 10^4 \ {}^oK$$

$$T_i = 4.0 \times 10^4 \ {}^oK$$

Consequently,

$$p_d \cong 826 \ N/m^2$$

$$p_d A_d \cong 4.0 \ N$$

The remaining aerodynamic thrust contribution from the exterior face of the anode is negligible. On leaving the anode orifice, the supersonic plasma flow must negotiate a 90^o turn. The Prandtl-Meyer expansion of a Mach one, $\gamma = 1.4$ flow about a 90^o corner decreases the isentropic pressure a factor of $O(10^{-4})$.(43) Thus to first order,

$$\frac{p_e A_e}{p_d A_d} << 1$$

since $A_e/A_d = O(1 - 10)$.

The outer flow electrothermal thrust component is therefore estimated to be,

$$\begin{aligned} T^{o}_{et} &= p_c\, A_c - p_d\, A_d + p_e\, A_e \\ &\cong 6.7 - 4.0 \\ &\cong 2.7 \;\; \mathrm{N} \end{aligned}$$

and the total thrust attributable to the outer flow, becomes,

$$\begin{aligned} T^{o} &= T^{o}_{em} + T^{o}_{et} \\ &\cong 16.0 + 2.7 \\ &\cong 18.7 \;\; \mathrm{N} \end{aligned}$$

References

1. Jahn, R. G., Physics of Electric Propulsion, McGraw-Hill Book Company, New York, 1968.
2. John, R. R., Bennett, S. and Connors, J. F., "Experimental Performance of a High Specific Impulse Arc Jet Engine," A.I.A.A. Paper No. 64-669, 1964.
3. Marshall, J., "Performance of a Hydromagnetic Plasma Gun," Physics of Fluids, Vol. 3, January 1960.
4. Burkhardt, L. C. and Lovberg, R. H., "Current Sheet in a Coaxial Plasma Gun," Physics of Fluids, Vol. 5, No. 3, March 1962.
5. Jahn, R. G., von Jaskowsky, W. F. and Burton, R. L., "Ejection of a Pinched Plasma From an Axial Orifice," A.I.A.A. Journal, Vol. 3, No. 10, October 1965.
6. Clark, K. E. and Jahn, R. G., "Quasi-steady Plasma Acceleration," A.I.A.A. Journal, Vol. 8, No. 2, February 1970.
7. Eckbreth, A. C. and Jahn, R. G., "Current Pattern and Gas Flow Stabilization in Pulsed Plasma Accelerators," A.I.A.A. Journal, Vol. 8, No. 1, January 1970.
8. Ducati, A. C., Gianni, G. M. and Muehlberger, E., "Experimental Results in High-Specific-Impulse Thermo-ionic Acceleration," A.I.A.A. Journal, Vol. 2, No. 8, August 1964.
9. Maecker, H., "Plasmaströmungen in Lichtbögen infolge eigenmagnetischer Kompression," Zeitschrift für Physik, 141, 198, February 1955.
10. Stratton, T. F., "High Current Steady State Coaxial Plasma Accelerators," A.I.A.A. Journal, Vol. 3, No. 10, October 1965.
11. Watson, V. R., "Computer Simulation of a Plasma Accelerator," SUIPR Report No. 313, May 1969.
12. Martinache, G. H. C., "A Theory on the Parallel-Plate Plasma Accelerator," Ph.D. thesis, Aerospace and Mechanical Sciences, Princeton University, May 1974.

References

13. Malliaris, A. C., John, R. R., Garrison, R. L. and Libby, D. R., "Quasi-steady MPD Propulsion at High Power," Final Tech. Report AVSD-0146-71-44, NASA CR 111872, February, 1971.

14. Jahn, R. G., Clark, K. E., Oberth, R. C. and Turchi, P. J., "Acceleration Patterns in Quasi-steady MPD Arcs," A.I.A.A. Journal, Vol. 9, No. 1, January 1971.

15. Di Capua, M. S. and Jahn, R. G., "Energy Deposition in Parallel-Plate Plasma Accelerators," NASA 31-001-005, Aerospace and Mechanical Sciences Rept. No. 1015, December 1971, Princeton University, Princeton, N. J.

16. Cory, J. S. and Jahn, R. G., "Mass, Momentum and Energy Flow from an MPD Accelerator," NASA NGL 31-001-005, Aerospace and Mechanical Sciences Rept. No. 999, September 1971, Princeton University, Princeton, N. J.

17. Bruckner, A. P. and Jahn, R. G., "Spectroscopic Studies of the Exhaust Plume of a Quasi-steady MPD Accelerator," NASA NGL 31-001-005, Aerospace and Mechanical Sciences Rept. No. 1041, May 1972, Princeton University, Princeton, N. J.

18. Workman, J. B., "Insulator Ablation in Magnetic Piston Shock Tubes," Physics of Fluids, Vol. 8, No. 12, December 1965.

19. Keck, J., "Current Speed in a Magnetic Annular Shock Tube," Physics of Fluids, Vol. 7, No. 11, November 1964.

20. Vondra, R. J., Thomassen, K., and Solbes, A., "Analysis of Solid Teflon Pulsed Plasma Thruster," Journal of Spacecraft and Rockets, Vol. 7, No. 12, December 1970.

21. Jahn, R. G., von Jaskowsky, W. F. and Casini, A. L., "Gas-triggered Pinch Discharge Switch," The Review of Scientific Instruments, Vol. 36, No. 1, January 1964.

22. Jahn, R. G. and Clark, K. E., "A Large Dielectric Vacuum Facility," A.I.A.A. Journal, Vol. 4, No. 6, June, 1966.

23. Schott, L., "Electrical Probes" in Plasma Diagnostics, Lochte-Holtgreven (eds.), Wiley & Sons, Inc., 1968.

References

24. Swift, J. D. and Schwar, M. J. R., Electrical Probes for Plasma Diagnostics, American Elsevier Publishing Company, Inc., 1969.

25. Johnson, E. O. and Malter, L., "A Floating Double Probe Method for Measurements in Gas Discharges," Physical Review, Vol. 80, No. 1, October 1950.

26. Bettinger, R. T. and Chew, A. A., "An End Effect Associated with Cylindrical Langmuir Probes Moving at Satellite Velocities," Journal of Geophysical Research, Vol. 73, No. 7, April, 1968.

27. Clayden, W. A., "Langmuir Probe Measurements in the R.A.R.D.E. Plasma Jet," Rarefied Gas Dynamics, 3rd Symposium, Vol. II, Academic Press, 1963.

28. Jahn, R. G., von Jaskowsky, W. F. and Clark, K. E., "Pulsed Electromagnetic Gas Acceleration," NASA NGL 31-001-005, semi-annual report for period 1 July 1971 to 31 December 1971, Aerospace and Mechanical Sciences Report No. 634r, January 1972, Princeton University, Princeton, N. J.

29. Boyle, M. J., "Plasma Velocity Measurements with Electric Probes," B.S.E. thesis, April 1969, Princeton University, Princeton, N. J.

30. Jahn, R. G., von Jaskowsky, W. F. and Clark, K. E., "Pulsed Electromagnetic Gas Acceleration," NASA NGL 31-001-005, semi-annual report for period 1 January 1972 to 30 June 1972, Aerospace and Mechanical Sciences Report No. 634s, July 1972, Princeton University, Princeton, N. J.

31. Lovberg, R. H., "Magnetic Probes," in Plasma Diagnostic Techniques, Huddlestone, R. H. and Leonard, S. L., (eds.) Academic Press, 1965.

32. Sovie, R. J. and Connoly, D. J., "Effect of Background Pressure on Magnetoplasmadynamic Thruster Operation," Journal of Spacecraft and Rockets, Vol. 7, No. 3, March, 1970.

References

33. Malliaris, A. C., John, R. R., Garrison, R. L. and Libby, D. R., "Performance of Quasi-steady MPD Thrusters at High Powers," A.I.A.A. Journal, Vol. 10, No. 2, February, 1972.

34. Turchi, P. J., "The Cathode Region of a Quasi-steady Magnetoplasmadynamic Arcjet," Ph.D. thesis, September 1970, Princeton University, Princeton, N. J.

35. Jahn, R. G., von Jaskowsky, W. F. and Clark, K. E., "Pulsed Electromagnetic Gas Acceleration," NASA NGL 31-001-005, semi-annual report for period 1 July 1972 to 31 December 1972, Aerospace and Mechanical Sciences Report No. 634t, January 1973, Princeton University, Princeton, N. J.

36. Hügel, H., "Self-magnetic effect in arcjet engines," A.I.A.A. Journal, Vol. 6, No. 8, August 1968.

37. Spitzer, L., Physics of Fully Ionized Gases, Interscience Publishers, New York, 1962.

38. Nighan, W. L., "Electrical Conductivity of Partially Ionized Noble Gases," Physics of Fluids, Vol. 12, No. 1, 1969.

39. Ducati, A. C. and Jahn, R. G., "Investigation of Pulsed Quasi-steady MPD arcjets," Report FR-061-10140, Plasmadyne, Santa Ana, California, June 1971.

40. Oberth, R. C. and Jahn, R. G., "Anode Phenomena in High-Current Accelerators," A.I.A.A. Journal, Vol. 10, No. 1, January 1972.

41. Jahn, R. G., von Jaskowsky, W. F. and Clark, K. E., "Pulsed Electromagnetic Gas Acceleration," NASA NGL 31-001-005, semi-annual report for period 1 January 1974 to 30 June 1974, Aerospace and Mechanical Sciences Dept. No. 634w, July 1974, Princeton University, Princeton, N. J.

42. Saber, A. J. and Jahn, R. G., "Anode Power in a Quasi-Steady MPD Thruster," Ph.D. thesis, May 1974, Princeton University, Princeton, N. J.

References

43. Shapiro, A. H., The Dynamics and Thermodynamics of Compressible Fluid Flow, Vol. I, Ronald Press Company, New York, 1953.

44. Baum, E. and Cann, G. L., "Thermodynamic Properties of Argon," ARL 63-133, Electro-Optical Systems, Inc., Pasadena, California, August, 1963.

45. Jahn, R. G., von Jaskowsky, W. F. and Clark, K. E., "Pulsed Electromagnetic Gas Acceleration," NASA NGL 31-001-005, semi-annual report for period 1 January 1970 to 30 June 1970, Aerospace and Mechanical Sciences Rept. No. 634o, July 1970, Princeton University, Princeton, N. J.

46. Hixon, T. L., "Near-Ultraviolet Spectroscopic Studies of a Quasi-Steady Magnetoplasmadynamic Arc," B. A. thesis, April 1972, Princeton University, Princeton, N. J.

47. Liepmann, H. W. and Roshko, A., Elements of Gasdynamics, John Wiley and Sons, Inc., New York, 1957.

48. Bates, D. R., Kingston, A. E. and McWhirter, R. W. P., "Recombination between electrons and atomic ions," Proceedings of the Royal Society, A 267, January, 1962.

49. Malliaris, A.C. and Libby, D.R., "Velocities of Neutral and Ionic Species in an MPD Flow," A.I.A.A. Paper No. 69-109, January, 1969.